Glycan analysis using mass spectrometry-based techniques

Inaugural-Dissertation

to obtain the academic degree

Doctor rerum naturalium (Dr. rer. nat.)

Submitted to the

Department of Biology, Chemistry, Pharmacy

of Freie Universität Berlin

by

Márkó Grabarics

from Dunaújváros, Hungary

Berlin, 2022

The work reported herein was performed from September 2017 to December 2021 at the Freie Universität Berlin and the Fritz-Haber-Institut der Max-Planck-Gesellschaft.

First reviewer: Prof. Dr. Kevin Pagel

Second reviewer: Prof. Dr. Gert von Helden

Date of defense: 8 April 2022

Declaration

I hereby declare that I have prepared my thesis independently and have not used any sources or aids other than those indicated. All quotations and citations have been duly acknowledged. I also confirm that the present doctoral thesis has not been submitted to any other university.

Berlin, 4 January 2022 Márkó Grabarics

"[. . .] a világhoz nem alkalmazkodni kell, hanem csinálni, nem újrarendezgetni azt, ami már megvan benne, hanem hozzáadni mindig."

Ottlik Géza, Iskola a határon

Abstract

Glycans are among the fundamental building blocks of life on Earth, essential to all known living organisms. They play key roles in a variety of biological processes, and contribute significantly to the extraordinary molecular and functional diversity of cells. As the importance of glycans has gradually been recognized, earning them the well-deserved attention of the scientific community, the lack of a high-throughput, *de novo* sequencing method has become a major obstacle in glycosciences, preventing the field from reaching its full potential. Although the invention of soft ionization methods gave enormous impetus for mass spectrometry-based glycan analysis, conventional fragmentation techniques often fail to distinguish isomeric carbohydrates or provide unambiguous structural assignment.

With the prospect of overcoming these limitations, this thesis aims to expand the mass spectrometry-based toolbox for glycan analysis and go beyond simply weighing sugars. Through the combination of mass spectrometry with orthogonal methods suitable to study ions transferred into the gas phase, we try to reveal further information about the species underlying the peaks in mass spectra. Coupling mass spectrometry to ion mobility spectrometry – a technique that harnesses electric forces for separating ions in gaseous media – results in a powerful method that provides information not only on the mass and charge, but also on the size and shape of ions. Using the concept of theoretical plates and plate heights, we develop a detailed analytical model that describes three main aspects of ion mobility separations: zone broadening, resolution, and peak capacity. The plate-height model for ion mobility separations was conceived in analogy to existing models of chromatography. As such, it enables the direct comparison of ion mobility spectrometry with other zonal separation methods, and may help to integrate this technique into the unified language of separation science. While our work is mainly theoretical and focuses on the technique rather than on specific molecules, the utility of the plate-height model to aid glycan analysis in everyday practice is demonstrated through a systematic study on fluorescently labeled oligosaccharides.

Santiago Ramón y Cajal warned young investigators against becoming obsessed with theories and instruments to an unhealthy extent, forgetting about nature in natural sciences. To avoid these pitfalls, the second part of this thesis focuses on the most important element of glycomics: the sugars themselves. In particular, we study the structure of glycosaminoglycans, a well-recognizable class of complex carbohydrates with a linear sequence and highly acidic character. As their biosynthesis is not entirely deterministic, the structure of glycosaminoglycans also exhibits random features. Moreover, sulfation of the disaccharide building blocks at various positions, together with potential epimerization of certain residues, lead to a multitude of isomeric sequences. To decipher this complexity, we studied mass-selected glycosaminoglycan ions with infrared action spectroscopy in the cryogenic environment of superfluid He droplets. The recorded infrared spectra revealed details about the structure of deprotonated oligosaccharides that could not have been attained by simple mass measurements, such as the localization of charges or differences in intramolecular hydrogen bonding patterns. In addition, diagnostic spectral features allowed for the unambiguous distinction of glycosaminoglycan stereoisomers with minute structural differences. Finally, the surprisingly strong structure–spectrum correlations observed in the vibrational fingerprints of these ions have potential implications for *de novo* sequence assignment, providing motivation for future spectroscopic experiments on glycosaminoglycans.

Zusammenfassung

Glykane gehören zu den grundlegenden Bausteinen des Lebens. Sie sind essentiell für eine Vielzahl von biologischen Prozessen und tragen wesentlich zu der außergewöhnlichen molekularen und funktionellen Vielfalt von Zellen bei. Im Laufe der vergangenen Jahrzehnte erhielten Glykane wachsende Aufmerksamkeit vonseiten der wissenschaftlichen Gemeinschaft, nachdem ihre Bedeutung zunehmend anerkannt wurde. Das Fehlen einer universellen Hochdurchsatz-Sequenzierungsmethode stellt jedoch ein großes Hindernis in der Kohlenhydratforschung dar und verhindert, dass die Glykowissenschaften ihr volles Potenzial entfalten können. Obwohl die Erfindung von "sanften" Ionisationsmethoden der massenspektrometrischen Glykananalyse großen Auftrieb gegeben hat, ermöglichen traditionelle Fragmentierungstechniken oft keine Unterscheidung oder eindeutige Strukturzuordnung von Kohlenhydratisomeren.

Mit der Aussicht, diese Einschränkungen zu überwinden, verfolgt diese Arbeit das Ziel, die massenspektrometriebasierte Glykananalyse zu erweitern und über das einfache Wiegen von Zuckern hinauszugehen. Durch die Kombination von Massenspektrometrie mit orthogonalen Methoden versuchen wir zusätzliche Informationen über die Analyten zu erhalten, die sich hinter den Peaks im Massenspektrum verbergen. Die Kopplung von Massenspektrometrie mit Ionenmobilitätsspektrometrie – eine Technik, die elektrische Kräfte zur Trennung von Ionen in inerten Gasen nutzt – führt zu einer leistungsstarken Methode, die nicht nur Informationen über Masse und Ladung, sondern auch über die Größe und Form der Ionen liefert. Durch Verwendung des Konzepts von Trennstufenzahlen und Trennstufenhöhen entwickeln wir hier ein detailliertes analytisches Modell, um drei Hauptaspekte der Ionenmobilitätstrennungen zu beschreiben: Zonenverbreiterung, Auflösung und Peakkapazität. Dieses Modell für Ionenmobilitätstrennungen wurde in Analogie zu den bestehenden Modellen der Chromatographie konzipiert. Daher ermöglicht es den direkten Vergleich der Ionenmobilitätsspektrometrie mit anderen zonalen Trennmethoden und könnte die Integration von Ionenmobilitätsspektrometrie in das einheitliche System der Trennwissenschaft fördern.

Dieser theoretische Teil der Arbeit konzentriert sich auf technische Aspekte, während der praktische Nutzen des Modells durch eine systematische Studie über fluoreszenzmarkierte Glykane demonstriert wird.

Santiago Ramón y Cajal warnte junge Forschende davor, in einem ungesunden Ausmaß von Theorien und Instrumenten besessen zu sein und dabei die Natur in den Naturwissenschaften zu vergessen. Um diese Fallstricke zu vermeiden, fokussiert sich der zweite Teil dieser Arbeit auf das wichtigste Element der Kohlenhydratforschung: die Zucker selbst. Vor allem untersuchen wir die Struktur von Glykosaminoglykanen, einer einzigartigen Klasse komplexer Kohlenhydrate mit linearer Sequenz und stark saurem Charakter. Da ihre Biosynthese nicht völlig deterministisch ist, weist die Struktur der Glykosaminoglykane stochastische Merkmale auf. Darüber hinaus führt die Sulfatierung der Disaccharid-Bausteine und die mögliche Epimerisierung bestimmter Reste zu einer Vielzahl isomerer Sequenzen. Um diese Komplexität zu entschlüsseln, haben wir massenselektierte Glykosaminoglykan Ionen mit Infrarotspektroskopie in der kryogenen Umgebung suprafluider Heliumtröpfchen untersucht. Die Infrarotspektren enthüllten Details über die Struktur der deprotonierten Oligosaccharide, die durch bloße Massenspektrometrie verborgen blieben. Solche Informationen sind zum Beispiel die Lokalisierung von Ladungen oder Unterschiede in den intramolekularen Wasserstoffbrückenbindungen. Die diagnostischen Spektralbanden ermöglichten auch die eindeutige Unterscheidung von Stereoisomeren mit minimalen strukturellen Unterschieden. Schließlich könnten die überraschend starken Struktur–Spektrum Korrelationen, die in den spektroskopischen Fingerabdrücken dieser Ionen beobachtet wurden, potentielle Auswirkungen auf die Sequenzierung von Glykosaminoglykanen haben und daher zukünftige spektroskopische Experimente an diesen Biomolekülen vorantreiben.

Contents

Chapter 1

Introduction

This introductory chapter aims to give a general overview of the work presented herein. It provides a brief look into the current state of glycan analysis, clarifies the motivation that initiated our research, defines the scope and main objectives of this thesis, and outlines the specific topics addressed in subsequent chapters.

Living systems encode information and function in the sequence of biopolymers, such as nucleic acids, proteins, and carbohydrates. The importance of nucleic acids and proteins as key actors of the cellular machinery, responsible for a variety of sophisticated tasks, was recognized early on by chemists and biologists alike. Knowledge accumulated through fundamental research led to the development of powerful tools enabling the high-throughput, automated synthesis and sequencing of these biopolymers, which in turn provided further insight into their structure and biological roles.[1–12] In comparison, carbohydrates were mainly considered to be simple metabolic substrates and structural elements, and glycosciences lagged behind their counterparts dealing with nucleic acids and proteins.

In the past decades however, the diversity of biological functions fulfilled by complex carbohydrates or glycans, has gradually become apparent.[13–20] In light of the accumulated evidence for the existence of specific glycan–protein interactions, well-defined binding motifs, and structure–function relationships with the potential to be harnessed for medical applications, it may seem surprising at first that no automated, high-throughput method has been developed to date that would allow for the *de novo* sequencing of glycans. The reason for the lack of a universal glycan sequencing workflow lies in the immense structural complexity of these molecules. In contrast to nucleic acids and proteins that possess a linear sequence, glycans often form branched structures with complex regiochemistry. In addition, many of their building blocks differ only in the configuration of a single stereocenter, and variations in the anomeric configuration further increase the number of possible isomers. Finally, as no amplification methods exist that may rapidly multiply defined glycan structures, they are often available only in limited quantities.

With the advent of soft ionization methods enabling the gentle transfer of nonvolatile species into the gas phase, mass spectrometry (MS) has become the primary method for the analysis of various biomolecules, including glycans and glycoconjugates.[21–27] However, whereas conventional tandem MS-based methods have revolutionized protein analysis, they often fail to reveal crucial information required for the unambiguous distinction and identification of isomeric glycans. Such species exhibit identical mass-to-charge (m/z) ratios, and are often indistinguishable based on their fragmentation patterns. To overcome these limitations, novel techniques have been introduced to the field of glycomics for studying ions in the gas phase. These methods, adapted originally from molecular physics, have significantly expanded the MS-based glycan analysis toolbox, enabling researchers to go far beyond the measurement of simple m/z ratios and gain information on the structure of glycan ions in previously unattainable details.

One such method in the focus of this thesis is ion mobility spectrometry

(IMS), an electrophoretic technique that separates ions in an inert buffer gas according to their mobilities.[28,29] The measured mobilities can be related to collision cross sections (CCSs), which convey information on the size and shape of the ions.[30–32] IMS can be readily coupled to MS analysis, the resulting hyphenated method thus providing information not only on the mass and charge, but also on the overall three-dimensional structure of the analytes.[33,34] In addition to revealing structural information, IMS also serves as a post-ionization separation technique that may significantly improve the overall peak capacity of multidimensional analytical workflows.[35] In this sense, time-dispersive IMS can be viewed as a differential migration method that shares many common features with chromatographic and condensed-phase electrophoretic systems. The recognition of these key similarities between ion mobility separations and the above-mentioned differential migration techniques served as the direct motivation for our research. Analogously to chromatography where studies on the mechanism of zone broadening have been aiding method development and promoting advancements in instrumentation, a suitable model describing zone broadening, resolution, and peak capacity in ion mobility separations may contribute to the further development of this field. Therefore, utilizing the general concept of theoretical plates and plate heights,[36] in this thesis we set out develop such a simple analytical model for ion mobility separations. While the work is mainly theoretical and the resulting plate-height model is not limited to any specific molecule class, the practical utility of our findings is demonstrated through suitable examples of glycan analysis.

Once ions are isolated in the gas phase, one may study their structure not only by manipulating their motion with electric fields, but also by probing them using tunable laser radiation, which allows for recording optical spectra of mass-selected species.[37–39] Infrared (IR) spectroscopy of ions cooled to cryogenic temperatures proved to be an extremely powerful method for glycan analysis, combining the sensitivity and separation capabilities of MS with the structural information provided by vibrational spectroscopy.[40–42] To record highly resolved IR spectra of glycans, thermal line broadening must be minimized, making cryogenic temperatures essential. For this reason, we employ a method where mass-selected ions are embedded in superfluid He droplets, which serve as ideal cryogenic matrix by providing sub-kelvin temperatures for IR spectroscopic experiments.[43,44] The method, referred to herein as cold-ion IR spectroscopy, has been successfully employed for the structural characterization of various glycans, such as milk oligosaccharides, Lewis epitopes, or glycosyl cations carrying different protecting groups.[44–49] In this thesis, we explore the potential of cold-ion IR spectroscopy for the analysis of glycosaminoglycans, a unique class of acidic carbohydrates whose structural complexity represents an immense challenge for state-of-the-art

glycan analysis methods.

Including the present introduction, the content of this thesis is organized into six individual chapters. In **Chapter 2** we address fundamental aspects of the structure and biological functions of carbohydrates, with special focus on glycosaminoglycans. We then briefly discuss the basics of the experimental techniques employed herein, addressing electrospray ionization mass spectrometry, ion mobility separations, and cold-ion IR spectroscopy in He droplets. Following the discussion of fundamentals, **Chapter 3** provides a concise overview of the instruments and experimental methods applied. The main findings of the thesis are presented in two separate chapters. **Chapter 4** is dedicated entirely to developing and exploring a plate-height model for ion mobility separations. It begins with a dedicated introduction, aimed at familiarizing the reader with the concepts, measures, and nomenclature adapted from chromatography and separation science. This section is followed by the presentation and discussion of results, organized according to the three main aspects of zonal separations: zone broadening, resolution, and peak capacity. The chapter is completed with a practical example, demonstrating the utility of the plate-height model for glycan analysis. **Chapter 5** presents the most important findings obtained by studying glycosaminoglycan (GAG) oligosaccharides with cold-ion IR spectroscopy in He droplets. GAGs are highly acidic carbohydrates with a linear sequence, participating in various biological processes ranging from neural development to inflammation. Dense sulfation of the chains at various positions in combination with epimeric building blocks give rise to a vast number of isomeric sequences, making their analysis extremely challenging. This chapter focuses on diagnostic spectral features arising from sulfation, the distinction and identification of stereoisomeric structures, and the strong structure–spectrum relationships observed in the vibrational fingerprints of these ions. Finally, in **Chapter 6** we revisit the main findings of the thesis and discuss perspectives for the future.

Chapter 2

Fundamentals

This chapter outlines a few fundamental concepts to provide a theoretical basis for subsequent sections. First, the structure and biological functions of carbohydrates are discussed, with special focus on glycosaminoglycans, a unique class of acidic saccharides. Having introduced the molecules at the forefront of this thesis, we then briefly review the basics of electrospray ionization mass spectrometry, ion mobility spectrometry, and cold-ion infrared spectroscopy, the experimental techniques employed herein for the analysis of glycans.

Chapter 2 is partly based on the following publication:

M. Grabarics, M. Lettow, C. Kirschbaum, K. Greis, C. Manz, K. Pagel; Mass spectrometry-based techniques to elucidate the sugar code, *Chemical Reviews* **2021**. Article in press. DOI: 10.1021/acs.chemrev.1c00380.

2.1 Structure and biological functions of carbohydrates

Carbohydrates are the most abundant organic polymers on Earth.[50,51] As one of the four major classes of biomacromolecules, they are also essential to all known living organisms.[19] Originally, the name "carbohydrate" was applied to simple sugars and stemmed from the fact that the composition of these compounds may be described by the general formula $C_n(H_2O)_m$. Today this term is employed in a much broader sense: we may define carbohydrates as polyhydroxy aldehydes and ketones, including their polymerization products and simple derivatives (*e.g.* amino sugars, alditols, aldaric and uronic acids). Although the above definition seems rather arbitrary at first glance, this arbitrariness merely reflects that nature is neither concerned nor confined by such artificial constructs of the human intellect as IUPAC recommendations.[52] Indeed, carbohydrates display a unique combination of characteristics that make them a diverse but well-recognizable class of bioorganic molecules. To shine a light on these features, let us take a closer look at carbohydrate structure through some examples.

The most simple representatives of carbohydrates are the so-called monosaccharides, such as ribose, glucose, or fructose. They vary in size, ranging from the smallest trioses with three carbon atoms to nonoses containing a chain of nine covalently linked carbons. While even larger monosaccharides are conceivable and may be synthesized chemically, such structures do not occur in natural sources. Based on their carbonyl functional groups, parent monosaccharides can be grouped into two main categories: those carrying a (potential) formyl group are termed aldoses, while those with a (potential) ketonic carbonyl group are ketoses. Except for dihydroxyacetone, the simplest ketose, monosaccharides contain at least one stereocenter. As a consequence, carbohydrates generally lack a rotation–reflection axis of symmetry, meaning they are chiral molecules (exceptions are the *meso* forms of certain alditols and aldaric acids).

The structural complexity of monosaccharides largely stems from the high number of stereocenters in these molecules. In case of aldohexoses with the composition $C_6H_{12}O_6$, the 4 nonequivalent stereocenters lead to $2^4 = 16$ different open chain stereoisomers, forming 8 pairs of enantiomers (see Figure 2.1). Designation of the enantiomers follows the system devised by Emil Fischer, who received the Nobel Prize in Chemistry in 1902 for his groundbreaking work in sugar synthesis.[53,54] Briefly, monosaccharides are assigned to either the D- or L-series based on the configuration of the highest-numbered stereocenter, the so-called configurational atom. A monosaccharide belongs

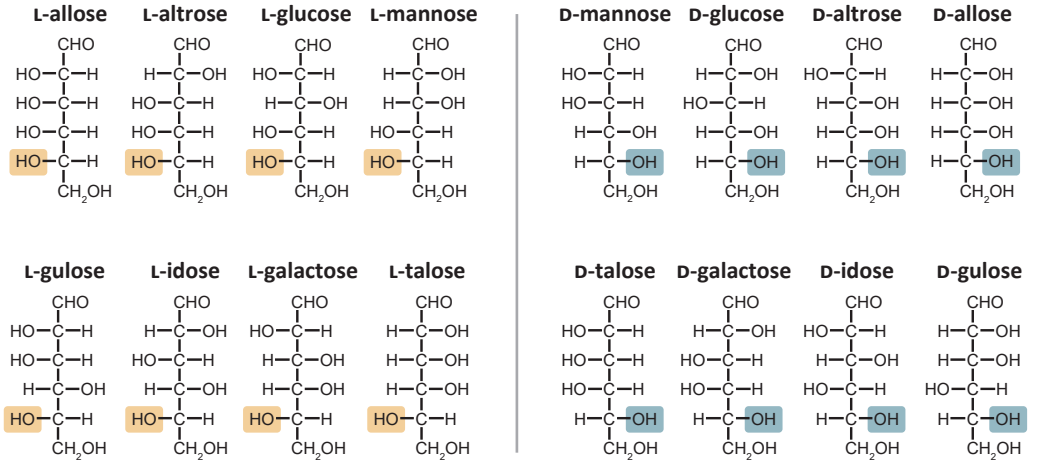

Figure 2.1: The $2^4 = 16$ aldohexose stereoisomers with the molecular formula $C_6H_{12}O_6$, forming 8 pairs of enantiomers. Having the same composition and constitution of atoms, the isomers differ only in the orientation of their hydroxy groups. The trivial name of each monosaccharide is provided above the respective structure, portrayed using the Fischer projection. In this two-dimensional representation, the longest carbon chain is depicted as a vertical line, the lowest numbered carbon being at the top. To obtain the desired projection, each stereocenter is considered individually. The carbon atom is placed in plane of the paper so that the hydrogen and the hydroxy group point towards the reader. When evaluating the configuration of the next stereocenter, the molecule should thus be rotated by 180° about its vertical axis. For clarity, hydroxy groups attached to the configurational atoms are highlighted in color, yellow marking L-sugars and light blue the respective enantiomers in the D-series.

to the L-series if the hydroxy substituent attached to the configurational atom points to the left in the Fischer projection, while sugars are marked with the configurational symbol D if the aforementioned hydroxy group falls on the right-hand side.

The stereochemical complexity may further increase due to the characteristic ring–chain tautomerization of sugars. Aldoses and ketoses show a propensity to form cyclic hemiacetals and hemiketals, respectively, and this ring closure gives rise to a new center of chirality, the anomeric center. The resulting closed-ring epimers differ only in the configuration of the anomeric carbon, and therefore are called anomers. In protic solvents the anomers can readily interconvert through the open chain carbonyl structure. Figure 2.2 depicts the above-mentioned cyclization reaction on the example of D-glucose. The configuration at the newly formed stereocenter is designated using a relative stereodescriptor. If the exocyclic oxygen atom at the anomeric center and the oxygen attached to the anomeric reference atom ($C5$ in glucose) are formally *cis* in the Fischer projection, the anomeric configuration is specified

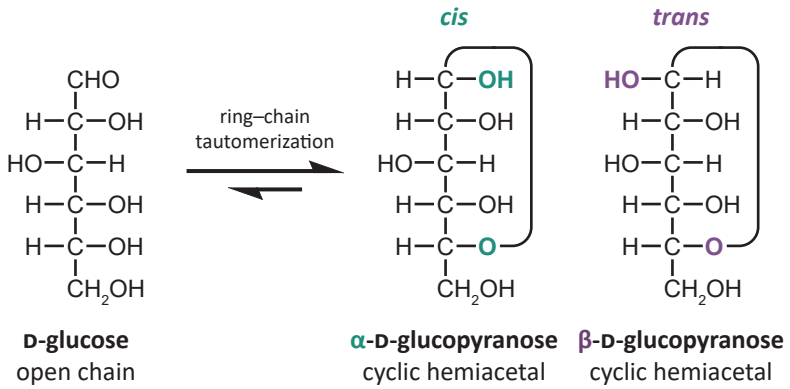

Figure 2.2: Ring–chain tautomerization of D-glucose. Covalent bond formation between the oxygen atom attached to $C5$ and the prochiral carbon atom of the formyl group leads to heterocyclic structures and the emergence of a new stereocenter. The configuration of this so-called anomeric center is designated using the relative stereodescriptors α and β. Six-membered carbohydrate rings are termed pyranoses, following the proposition of Goodyear and Haworth.[55]

with the symbol α. Evidently, when β-anomers are depicted using the Fischer projection, the aforementioned substituents are formally *trans*.

As their name implies, monosaccharides can serve as monomer building blocks to form complex oligo- and polysaccharides, often referred to as glycans. In these biopolymers, the monosaccharides are connected to each other *via* glycosidic bonds, *i.e.* covalent linkages involving the anomeric carbon of one monomer unit and an exocyclic oxygen of another. In general, the complexity of glycans stems from three key aspects of their structure: the monosaccharide composition, the connectivity of building blocks, and the anomeric configuration.

Composition. The composition of a glycan is defined by the identity and number of monosaccharide units linked together *via* glycosidic bonds. While the number of potential building blocks is enormous, this number may be narrowed down based on prior knowledge of the sample. Figure 2.3 shows the ten distinct monosaccharides that make up most of the mammalian glycome: D-glucose (Glu), D-galactose (Gal), and D-mannose (Man), *N*-acetyl-D-glucosamine (GlcNAc) and *N*-acetyl-D-galactosamine (GalNAc), D-glucuronic (GlcA) and L-iduronic acid (IdoA), D-xylose (Xyl), *N*-acetyl-D-neuraminic acid (Neu5Ac), and L-fucose (Fuc). Importantly, many of these monosaccharides are diastereomers. While stereoisomers with minute structural differences may display extremely similar physico-chemical characteristics, the same structural differences often manifest in contrasting behavior

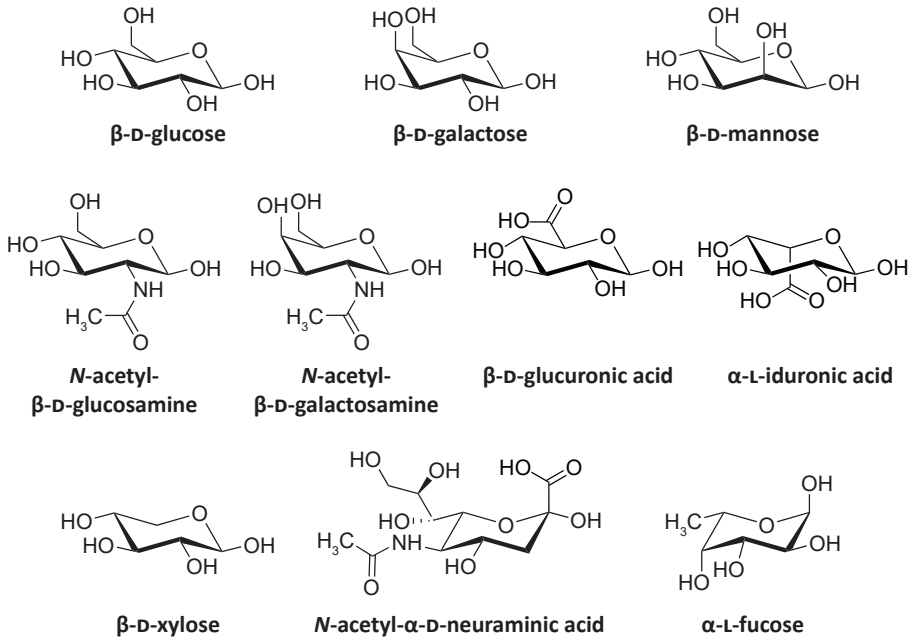

Figure 2.3: Monosaccharides serving as common building blocks in mammalian glycans. These include (top) three isomeric hexoses, (center) two related *N*-acetylhexosamines and a pair of hexuronic acid epimers, as well as (bottom) the pentose D-xylose, the 9-carbon backbone *N*-acetyl-D-neuraminic acid, and the deoxy sugar L-fucose (essentially a 6-deoxy-L-galactose). The depicted anomers reflect the thermodynamically more stable or physiologically more abundant forms.

in biological recognition processes. Indeed, glycans differing merely in the configuration of a few stereocenters may display remarkably different physiological functions. This Janus-faced trait of glycans renders them exceptionally challenging to study by means of chemical and physical methods.

Connectivity. In proteins and DNA, the connectivity of building blocks can be defined by a single linear sequence, since peptide bonds and 3'–5' phosphodiester linkages enable no variation with respect to linkage position, only to linkage order. In stark contrast, monosaccharide building blocks in glycans usually contain multiple free hydroxy groups that can readily participate in the formation of new glycosydic bonds. As such, additional monomer units may be attached at various positions to a growing glycan chain, leading to complex regiochemistry. In addition, if the attachment involves an internal residue, so-called branched structures arise. As branched glycans contain a single reducing but multiple nonreducing *termini*, glycan sequencing approaches are often fundamentally different from those developed for deciphering the inherently linear genetic code.

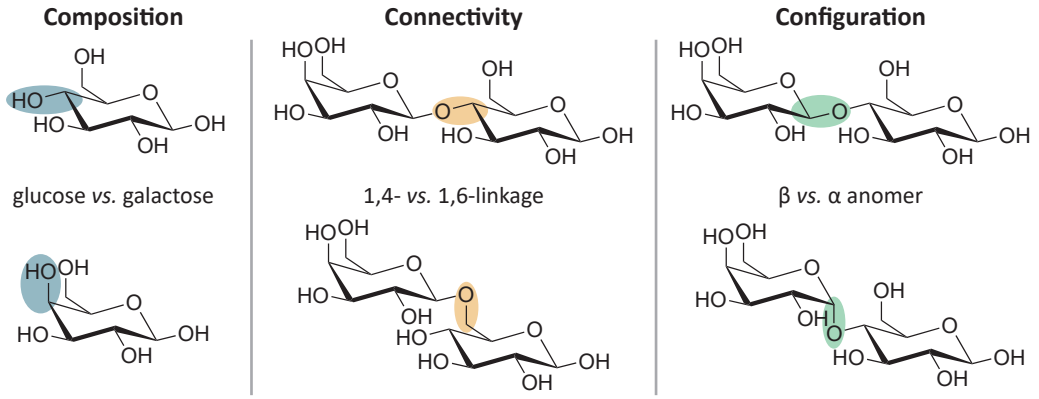

Figure 2.4: Main levels of glycan structural complexity: monosaccharide composition, connectivity of building blocks, and configuration of the anomeric centers.

Configuration. As mentioned above, cyclic hemiacetal and hemiketal anomers may interconvert in solution. Upon formation of a glycosidic bond, however, the mobile proton participating in the tautomerization is removed, and the anomeric center becomes stabilized in either the α or the β configuration. As glycosyltransferases catalyze glycosidic bond formation with high stereoselectivity during glycan biosynthesis, an ideal sequencing approach should be sensitive to the anomeric configuration. Complementing the above description, the three key elements of glycan structural complexity are also highlighted graphically in Figure 2.4

While they accurately reflect the composition, connectivity, and configuration of molecules, traditional carbohydrate representation schemes have inherent limitations. The Fischer projection, the Haworth and Mills depictions, or the traditional chair representation may be highly suited for small mono- and disaccharides, but portraying larger glycans becomes cumbersome, and the human eye often struggles to recognize subtle differences between similar species in such complex drawings. These shortcomings were successfully overcome in the symbol nomenclature for graphical representation of glycans (SNFG), a system developed with the specific aim of facilitating the depiction and interpretation of large oligo- and polysaccharides.[56] In the SNFG nomenclature, the various monosaccharide building blocks are represented by colorful geometric symbols, while the connecting lines reflecting glycosidic bonds encode information about connectivity and the anomeric configuration. Figure 2.5 introduces the SNFG nomenclature on the example of the milk oligosaccharide lacto-*N*-fucopentaose I. For simplicity, the SNFG system will be also adopted in this thesis.

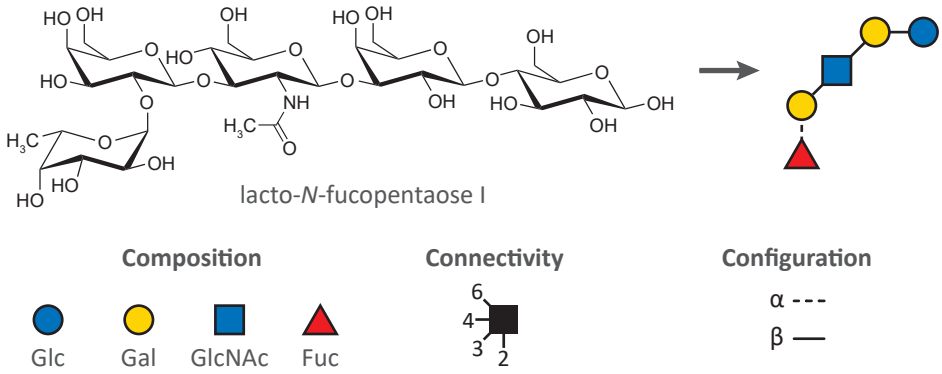

Figure 2.5: The milk oligosaccharide lacto-*N*-fucopentaose I depicted (left) conventionally and (right) according to the symbol nomenclature for glycans. In the latter nomenclature each monosaccharide unit is represented by a colorful symbol, while the angle of the connecting lines reflects the linkage position. Dashed and solid lines represent α- and β-anomeric configurations, respectively.

Linking structure to biological functions is one of the main objectives of glycosciences. When ordering carbohydrates by size, on one end of the spectrum we find simple mono- and disaccharides that mainly serve as fuel for the cellular machinery. At the other extreme are large, water insoluble polysaccharides such as cellulose and chitin, the principal building materials of plant and fungal cell walls, respectively. Between these simple sugars and highly repetitive polysaccharides, glycans represent a more diverse and largely unexplored domain with remarkable structural complexity and a range of sophisticated biological functions.[13,18] While glycans may also occur in the form of free saccharides as for example in milk[57–59], most of them are covalently attached to other biomolecules, forming glycoconjugates such as glycolipids, glycoproteins, and proteoglycans.[14,60] In fact, glycosylation is the most abundant (and certainly most complex) post-translational modification found in proteins.[17,61]

Glycans appear ubiquitously across all domains of life and all cell types. They are especially abundant on the surface of cells where they form a dense sugary coating, the glycocalyx (meaning "sweet husk").[62,63] It is estimated that the concentration of sialic acids in the glycocalyx of typical human B lymphocytes may be on the order of 100 mM, which reflects the prevalence of glycans on cell surfaces.[19] Besides being anchored to cell membranes, glycans are also found on soluble proteins and are essential constituents of extracellular matrices (ECM). As hydrophilic oligosaccharide chains are generally exposed to the exterior of glycoproteins, glycans may have a strong impact on the folding of these molecules.[64,65]

Considering their abundance on membrane-bound and secreted glycopro-

teins and proteoglycans, it is not surprising that glycans participate in various biological recognition processes.[66–69] They orchestrate cell–cell and cell–matrix interactions, including such specific processes as the sperm–egg interplay in mammalian fertilization.[70–72] Besides mediating physiological processes in healthy tissues, glycans also play a role in cancer and inflammation, where alterations in protein glycosylation may serve as diagnostic markers.[15,73] Glycan-mediated interactions also occur between different organisms, and many pathogens have developed ingenious methods to target glycan motifs on the surface of host cells. Adhesins of the malaria pathogen *Plasmodium falciparum*, viral agglutinins, and many bacterial and plant toxins, such as the cholera and ricin toxins, bind to host glycans.[74–76] Such interactions may also be exploited for pharmaceutical purposes, *e.g.* for the development of (synthetic) carbohydrate-based vaccines.[77–79] Besides serving as targets for vaccines and therapeutic antibodies, glycans and glycomimetic compounds can also be applied as therapeutics, prominent examples being the antidiabetic drug acarbose or the anticoagulant heparin and its derivatives.[80,81]

While the above list of examples is obviously incomplete and may only serve as a glimpse into the diverse biological roles of these molecules, it still leads us to the conclusion that glycans are not merely cellular decorations. They are key actors in a wide range of physiological processes, and as such, deserve the growing attention of researchers. Following this general overview of carbohydrate structure and function, in the next section we provide a more detailed description of glycosaminoglycans, an idiosyncratic class of complex saccharides in the focus of this thesis.

2.2 Glycosaminoglycans

The present section provides an overview of the structural and physiological characteristics, as well as the analytical challenges associated with glycosaminoglycans (GAGs). GAGs are unbranched, highly acidic polysaccharides in the kDa to MDa range, expressed by essentially all animal cells.[82] Although also present intracellularly, GAGs are much more prominent on cell surfaces and in the ECM. They interact with a diverse set of soluble and membrane proteins, as well as ECM components: cytokines and chemokines, growth factors and their receptors, morphogens, blood coagulation factors, lipoproteins, integrins, and collagens.[69,83–86] In addition to these endogenous binding partners, GAGs may also interact with viral and microbial proteins.[60,87] Thus, they participate in various physio- and pathophysiological processes, such as embryonic and neural development, angiogenesis, hemostasis, inflammation, cancer progression, and infection.[16,73,88–92]

Albeit a structurally heterogeneous class of complex carbohydrates, some common, distinct features of GAGs render them a unique, well-recognizable group within the glycome. All GAGs possess a linear sequence formed by repeating disaccharide units, where an (occasionally deacetylated) *N*-acetylhexosamine alternates with hexuronic acids or galactose. Based on the structure of these disaccharides, four families of GAGs are distinguished traditionally: hyaluronan, chondroitin sulfate jointly with dermatan sulfate, heparan sulfate together with heparin, and keratan sulfate.[82,93] Figure 2.6 provides a structural overview of the aforementioned GAG families, accompanied by a brief description below.

Hyaluronan or hyaluronic acid (HA). An extremely high molecular weight polysaccharide, HA consists of alternating *N*-acetyl-D-glucosamine (GlcNAc) and D-glucuronic acid (GlcA) residues, forming a poly(GlcAβ3-GlcNAcβ4) chain of several thousand disaccharide units.[94] HA emerged relatively late in the evolution of animals and appears to be an exception among GAGs in many aspects. It stands out as the only GAG where the repetitive copolymeric chain is not modified further by sulfation or epimerization. In addition, HA is not linked covalently to proteins, in stark contrast to other GAGs that form specific glycoproteins, so-called proteoglycans, whose functions are determined principally by their GAG constituents.

Chondroitin sulfate (CS) and dermatan sulfate (DS). CS and DS are closely related galactosaminoglycans, often referred to as a single family and discussed in conjunction owing to substantial similarities in structure,

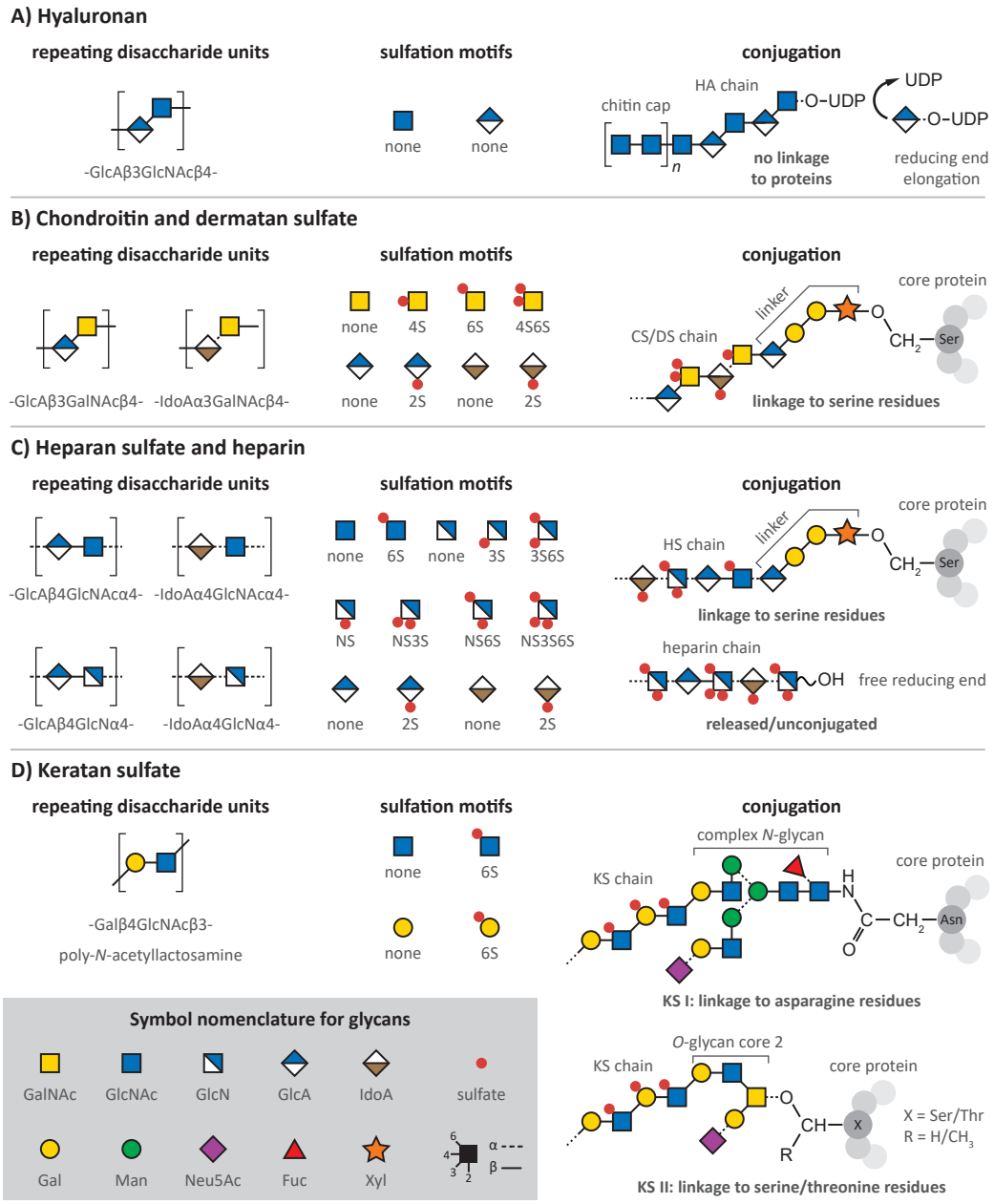

Figure 2.6: Structural overview of glycosaminoglycans, highlighting the characteristic disaccharide units, sulfation motifs, and potential protein linkages found in the four main families. (A) Hyaluronan chains are not modified further by sulfation or epimerization. Uniquely, biosynthesis starts with the formation of a chitin cap and proceeds towards the reducing end. (B) Chondroitin and dermatan sulfate display a variety of sulfation motifs. The chains are linked to serine residues of proteoglycan core proteins through a specific tetrasaccharide linker. (C) Heparan sulfate and heparin represent the most diverse family of glycosaminoglycans. The heparin chain depicted reflects the antithrombin III binding sequence. (D) Keratan sulfate contains galactose instead of hexuronic acid. Chains may be linked to both asparagine as well as serine/threonine residues of core proteins.

biosynthesis, and function.[95] The main difference between the two concerns their hexuronic acid residues. CS contains exclusively GlcA, alternating with *N*-acetyl-D-galactosamine (GalNAc) to build poly(GlcAβ3-GalNAcβ4) chains. In contrast, DS contains not only GlcA, but also its *C*5 epimer, L-iduronic acid (IdoA) to varying extents. It leads to a more complex polymer backbone where two basic disaccharide building blocks vary across the sequence: (GlcAβ3-GalNAcβ4) and (IdoAα3-GalNAcβ4). It is, however, also widespread to distinguish GlcA-containing CS disaccharides and IdoA-containing DS disaccharides categorically, and referring to longer sequences containing both kinds of hexuronic acid as hybrid CS/DS chains. CS and DS chains may contain over 100 disaccharide units, and unlike HA, they are extensively sulfated. GlcA and IdoA may carry 2-*O*-sulfation, while GalNAc can be sulfated at the 4-*O*- and 6-*O*-positions. The resulting sulfation motifs give rise to several isomeric building blocks, and a complex sulfation pattern across the chains that influences molecular recognition and may encode functional information.[96] Elucidating the "sulfation code" of shorter bioactive protein-binding sequences along the polysaccharide chains is a major challenge in the analysis of all sulfated GAGs.

Heparan sulfate (HS) and heparin. HS and heparin form the structurally most complex GAG family. During their biosynthesis, the initial poly(GlcAβ4-GlcNAcα4) chain undergoes extensive modifications: epimerization of GlcA to IdoA, 2-*O*-sulfation of the hexuronic acids, *N*-deacetylation/*N*-sulfation, as well as 6-*O*- and the rare 3-*O*-sulfation of GlcNAc may all occur, affecting a varying number of residues.[97–99] The result is a heterogeneous copolymer of enormous complexity, with an extremely high density of ionizable functional groups.[100,101] Like CS and DS, HS is linked to serine residues of specific core proteins *via* a xylose-containing tetrasaccharide. The sulfation and epimerization pattern of GAG chains in these proteoglycans show temporal and spatial variation across tissues. In general, the composition of HS chains found on a certain kind of proteoglycan, but in different cell types, shows higher variability than the chains found on different proteoglycans within the same cell. Although sharing the same set of disaccharide building blocks and basic sulfation motifs, important differences exist between HS and heparin.[69,102] HS is expressed by virtually all animal cells, whereas heparin is produced by only a few cell types, most prominently connective tissue mastocytes. HS is attached to core proteins localized on cell surfaces and in the ECM. Heparin, on the other hand, is stored intracellularly in secretory granules, attached to its cytoplasmic core protein, serglycin. HS chains typically consist of 50–250 disaccharide units, while heparin chains are significantly shorter with an

average molecular weight of 12–15 kDa. In HS, regions showing extensive sulfation and epimerization are clustered along the chain (NS domains), separated by largely unmodified regions (NA domains). Heparin lacks such domain structure, serving as a single extended NS region: most of its GlcA residues undergo epimerization to IdoA, and the chains are more heavily sulfated (∼2.5 sulfates per disaccharide on average) than in HS (∼1 sulfate per disaccharide). Heparin is the largest biopharmaceutical in production, widely used as an anticoagulant in unconjugated form.

Keratan sulfate (KS). KS is unique among GAGs in that the chains lack hexuronic acid, containing instead D-galactose (Gal).[103,104] In KS chains, up to 50 repeating (GalAβ4-GlcNAcβ3) disaccharide units form the linear poly-*N*-acetyllactosamine backbone, whose strong acidic character stems from sulfation. Sulfate groups can be installed at the 6-*O*-position of both Gal and GlcNAc residues, with sulfated Gal occurring mainly adjacent to sulfated GlcNAc. In addition to *O*-mannose (KS III, not shown) and *O*-GalNAc (KS II) linkages, the chains may also be linked to asparagine residues (KS I) of core proteins in KS proteoglycans. Although the complex-type *N*-glycan linker may possess multiple antennae, KS chains themselves are not branched.

Sulfated GAGs represent immense structural complexity and are among the most challenging biopolymers to characterize. Obtaining information on the sequence of even the simplest full-length chains is a formidable task.[105–107] Due to the sheer size of full-length GAG polysaccharides, (partial) enzymatic or chemical depolymerization of the chains is crucial for obtaining smaller oligosaccharides that are tractable by MS-based methods (see Figure 2.7).[101,108–110] Thus, strategies to characterize and sequence GAGs tend to follow a bottom-up approach. The complexity of mixtures resulting from depolymerization and inherent size polydispersity imply that extensive multistep separations are indispensable in GAG analysis.[111–113] Depolymerization, combined with chromatographic and electrophoretic separations, provides the link between the full-length GAG chains and the shorter oligosaccharides (dp $\leq$ 12) compatible with MS analysis.

In general, complexity and the associated challenges stem from four main aspects of GAG structure: high degree of polymerization combined with size polydispersity, sequence microheterogeneity, high negative charge density, and the potentially isomeric building blocks. Being highly polydisperse, the length of GAG chains found on a certain proteoglycan at a given position is not uniform. Because of their microheterogeneity, GAGs cannot be characterized by a single, well-defined sequence, in contrast to biopolymers with template-driven biosynthesis, *e.g.* proteins or coding DNA. The dense sulfation of

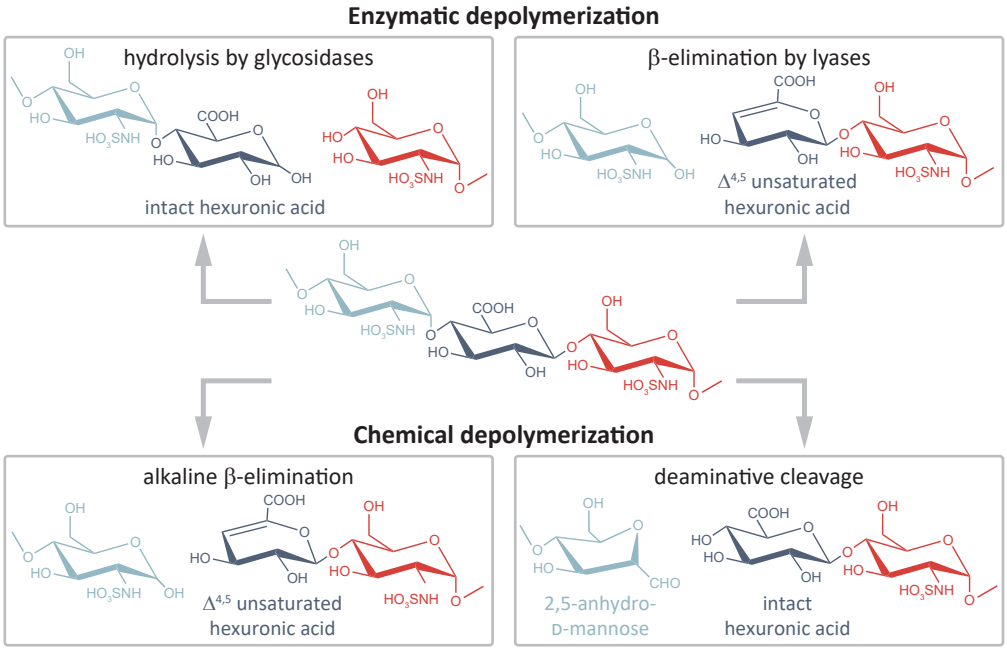

Figure 2.7: Common glycosaminoglycan depolymerization strategies shown through the example of heparan sulfate/heparin. (top, left) Enzymatic depolymerization of GAG chains may be performed using glycosidases, resulting in hydrolytic cleavage that preserves the hexuronic acid stereochemistry. To obtain oligosaccharide fragments covering the full sequence, enzymes with endolytic activity are necessary. Heparanases are endo-β-glucuronidases cleaving at the reducing end of GlcA residues in moderately sulfated HS/heparin chains. (top, right) Prokaryotic lyases, such as heparinase I–III, act *via* a β-eliminative mechanism, leading to $\Delta^{4,5}$-unsaturated hexuronic acid residues at the new nonreducing end. Consequently, stereochemical information is lost in the process. (bottom, left) Benzyl esterification with alkaline β-elimination may be applied for the depolymerization of GAGs, mimicking lyase activity. (bottom, right) Deaminative cleavage preserves hexuronic acid stereochemical information at the cleavage site, but alters the structure of the glucosamine through the formation of 2,5-anhydromannose. The reaction is blocked in the presence of *N*-acetyl groups on glucosamines, making prior deacetylation necessary.

GAGs complicates their MS analysis due to Coulomb repulsion, sulfate loss, and the formation of multiple adducts (see Section 2.3). Finally, epimerization and sulfation at various positions lead to a large number of isomeric building blocks, difficult to distinguish by conventional MS analysis that relies on the measurement of mass-to-charge ratios. The development of novel MS-based methods that may not only tackle the challenges arising from dense sulfation, but are also capable of distinguishing isomeric GAG sequences on the oligosaccharide level, is one of the main objectives of this thesis.

2.3 Electrospray ionization and mass spectrometry

This section briefly discusses a few basic aspects of electrospray ionization mass spectrometry (ESI-MS), focusing on details that are relevant to glycan analysis and the topics addressed in this thesis. The electrospray ion source as applied today was developed in the lab of John B. Fenn in the 1980s, enabling the efficient and gentle transfer of nonvolatile species from solution into the gas phase.[114,115] Building on the pioneering work of Malcolm Dole,[116–118] the research of Fenn and co-workers led to the successful realization of a long-standing dream of physical chemists to produce a beam of intact macromolecules suitable for subsequent MS experiments.[7,119,120] For this momentous achievement that revolutionized MS and the analysis of biological (macro)molecules, Fenn was awarded the Nobel Prize in Chemistry in 2002, becoming the oldest recipient at the time at the age of 85.[121]

To produce gas-phase ions by ESI, a solution containing the analytes is infused into an electrically conductive capillary. Upon establishing a high DC voltage – typically on the order of 0.5–3 kV – between the spray capillary and a counter electrode placed at a few centimeters distance, the strong electric field at the capillary tip leads to the polarization of the solvent and, consequently, to the distortion of the meniscus into a Taylor cone.[122,123] If the field is sufficiently high, a fine jet emerges from the cone and breaks subsequently into micron-sized droplets. The droplets carry a net electric charge due to an excess of ions with certain polarity, determined by the polarity of the applied voltage. As they move towards the counter electrode, the droplets undergo solvent evaporation and rapidly decrease in size. When the charge density of the shrinking droplets (defined by the q^2/r^3 ratio where q is the electric charge and r is the radius of the droplet) exceeds a critical value, surface tension may no longer hold them together against the increasing force of repulsive Coulombic interactions.[124] The inevitable fission of the droplets gives rise to a large number of second generation offsprings with lower charge density, which then also undergo repeated evaporation–fission events, leading eventually to the release of bare analyte ions into the gas phase.[123–125] In case the analytes lack readily ionizable functional groups, adduct formation with small charged species present in the electrosprayed solution can facilitate their ionization. Depending on the interface geometry, the beam of ions is then sampled and directed through a skimmer or an inlet capillary into vacuum, ready to be analyzed by MS.

While its vast potential was first demonstrated through studies on synthetic polymers and proteins, ESI has also brought new momentum into

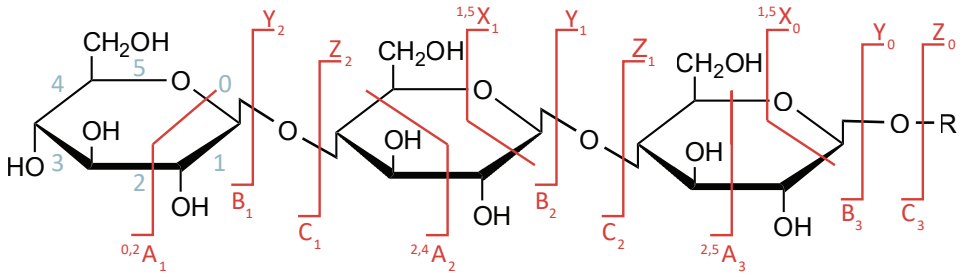

Figure 2.8: Domon–Costello nomenclature for carbohydrate fragments.[134] The A- and X-fragments result from cross-ring cleavages, whereas B- and C-fragments as well as their Y- and Z-type counterparts originate from glycosidic bond cleavages between adjacent monosaccharide units. Numbering of the bonds in the pyranose rings, indicated as superscript numerals in cross-ring fragments, is exemplarily shown for the glucose residue at the nonreducing end.

the field of MS-based glycan analysis.[126–132] Today, ESI-MS is arguably the most widespread technique for the sensitive, high-throughput analysis of glycans and glycoconjugates.[26] Being a soft ionization method that produces closed-shell ions in their electronic ground state with only moderate vibrational excitation, ESI is generally accompanied by low levels of in-source fragmentation, enabling the study of intact molecular ions.[133] Glycans, however, display an extraordinary diversity of potential isomers, which appear at identical mass-to-charge (m/z) ratios in the mass spectra. To distinguish the various isomers and obtain information on the underlying structure of glycans, ESI-MS is generally combined with suitable ion activation methods to induce dissociation of mass-selected species. Fragment ions of glycans are generally designated according to the widely accepted nomenclature introduced by Domon and Costello, which is shown graphically in Figure 2.8.[134]

In principle, two main categories of glycan fragments are being distinguished: those resulting from the cleavage of glycosidic linkages (B-, C-, Y-, and Z-type fragments), and cross-ring fragments that stem from the dissociation of multiple bonds across a single sugar ring (A- and X-fragments). While the former provide information on sequence and composition, the latter may reveal details on branching and connectivity, as well as on the position of sulfate modifications in GAGs. Unfortunately, conventional slow-heating ion activation methods such as collision-induced dissociation (CID) and infrared multiphoton dissociation (IRMPD) often fail to give rise to crucial A- and X-type product ions. Because these fragmentation techniques rely on the gradual vibrational excitation of the analytes, they generally favor dissociation channels with the lowest barriers, which tend to be those leading to glycosidic fragments or to the loss of SO_3 in sulfated GAGs.[22,26,113] As such, tandem

MS with CID and IRMPD often fails to distinguish isomeric glycans and may not enable their unambiguous structural assignment. For this reason, in the present thesis we combine MS with orthogonal methods suitable to study ions following their transfer into the gas phase. The two techniques, ion mobility spectrometry and cold-ion IR spectroscopy, are discussed in separate sections below.

2.4 Ion mobility spectrometry

Ion mobility spectrometry (IMS) is a gas-phase electrophoretic separation technique, widely employed as a stand-alone method for the detection of drugs, explosives, and chemical warfare agents.[135–137] It has a long history as part of ion mobility-mass spectrometry (IM-MS) couplings, with applications in fields as diverse as molecular physics and structural biology.[138–150] Since the commercialization of the first integrated instruments, IM-MS has gained remarkable popularity in bioanalytical chemistry[151–159] and become a key element of the glycomics toolbox.[26,34,42,160–164] Glycan isomers often exhibit identical fragment ion spectra, impeding their tandem MS-based distinction, while the presence of multiple isomers in a mixture calls for efficient separations. IMS proved to be extremely useful for the distinction, separation, and relative quantification of glycan isomers, helping to overcome key challenges associated with MS-based glycan analysis.[165–168] In addition, as comprehensive IMS analyses take place generally on the millisecond time scale, they fit perfectly between condensed-phase separations and fast MS experiments, further increasing the peak capacity of multidimensional workflows.[169]

In general, IMS separates ions based on differences in their gas-phase mobilities K, a transport property related to the ions' mass, charge, size, and shape. K is also influenced by the nature and number density of the buffer gas and by the effective temperature of the collisions. As they traverse a suitable gas-filled cell under the influence of an electric field, ions undergo binary collisions with the neutral gas particles. Larger, extended species collide more frequently, reaching lower velocities upon their electrophoretic motion than more compact ions. This simplified picture reveals the aptitude of IMS to separate isomers and conformers, species having identical m/z ratios but often differing in size and shape.

Within the low-field limit, ion–neutral collisions are essentially thermal, and K is basically independent of the electric field strength:[170–172]

$$K = \sqrt{\frac{18\pi}{\mu k_\mathrm{B} T}} \frac{ze}{16n} \frac{1}{\mathrm{CCS}}. \tag{2.1}$$

The above formula may be considered the fundamental low-field ion mobility equation, generally known as the Mason–Schamp equation. Here, μ is the reduced mass of the ion–neutral collision complex, k_B is the Boltzmann constant, T is the buffer gas temperature, z is the ionic charge state and e is the elementary charge (their product being the net ionic charge q) n is the buffer gas number density, and CCS is the rotationally averaged collision integral, also referred to as the collision cross section. CCSs are related to the size and shape of the collision partners, and also depend on interaction

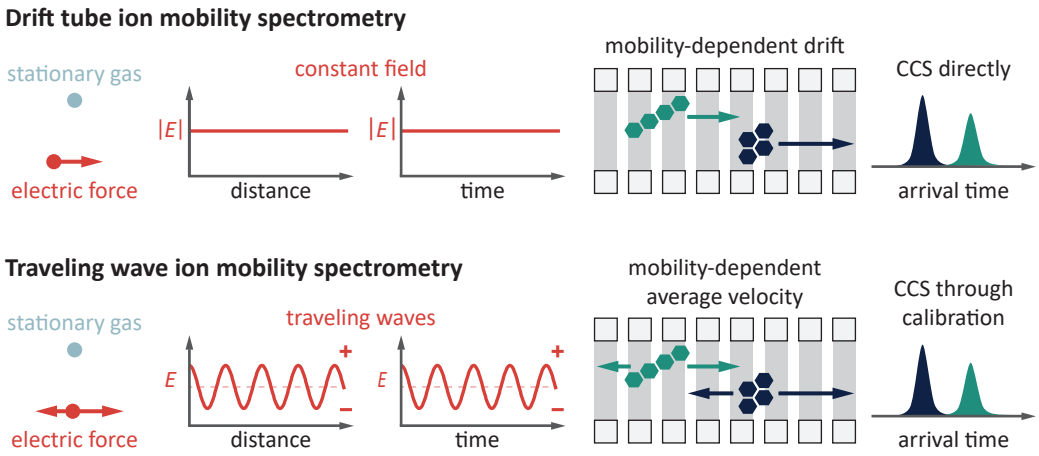

Figure 2.9: Overview and basic principles of temporally dispersive ion mobility techniques: (top) drift tube ion mobility spectrometry and (bottom) traveling wave ion mobility spectrometry.

potentials.[173] They serve as effective areas, generally expressed in units of $Å^2$, reflecting momentum transfer between the colliding particles.[29] The larger the CCS of an ion–neutral pair, the more efficient the momentum transfer between the ion and the gas particles in IMS. CCSs are independent of n and vary generally less with T than mobilities, making them suitable molecular descriptors. They are comparable across different IMS platforms and can be readily stored in databases, facilitating the identification of analytes. Besides experimental determination in suitable IMS experiments, CCSs may also be calculated by computational methods, addressed in more detail later.

A number of IMS techniques have been developed and commercialized in recent years that efficiently harness electric forces for separating ions in gases.[33,35,174,175] In the present work we address two time-dispersive IMS techniques that have been widely applied for glycan analysis. Figure 2.9 provides an overview of these techniques, accompanied by a brief description below.

Drift tube ion mobility spectrometry (DTIMS). In this technique, ions are propelled through a stationary buffer gas by a constant electric field, invariable in both space and time. Under such circumstances, the drift velocity v_D by which the ions traverse the gas-filled drift cell is directly proportional to their mobility:

$$v_D = KE_D, \tag{2.2}$$

the constant of proportionality E_D being the strength of the electric field. Because ions with higher K cover the same distance faster and thus reach

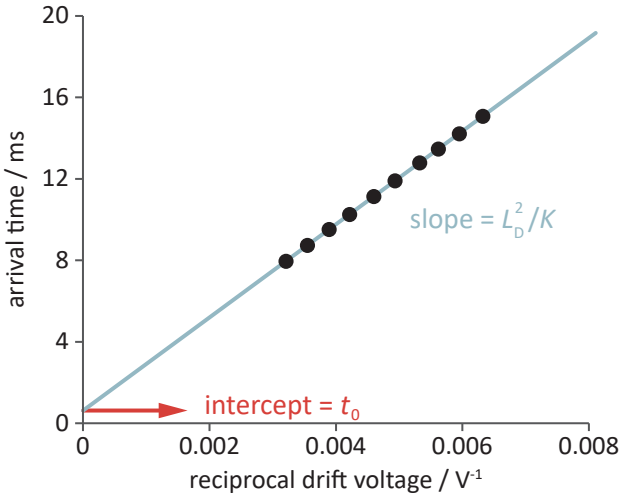

Figure 2.10: Graphical representation of the stepped-field approach to determine mobilities in drift tube ion mobility-mass spectrometry experiments. The depicted data points correspond to an experiment performed in N_2 buffer gas at 1.2 Torr using an instrument with a 250.5 mm long drift cell. From the determined mobility, the $^{DT}CCS_{N2}$ value of the singly charged anion with $m/z = 1687$ was calculated to be 518 $Å^2$.

the detector within a shorter drift time than their less mobile counterparts, DTIMS is considered a time-dispersive method:

$$t_D = \frac{L_D}{K E_D} = \frac{L_D^2}{K V_D}. \tag{2.3}$$

In the above equation t_D is the drift time, L_D is the length of the drift cell, while V_D denotes the drift voltage, the product of E_D and L_D. Thus, in DTIMS one may directly deduce mobilities from the experimentally determined t_D values according to Eq. 2.3. In addition, when experiments are performed within the low-field regime, the Mason–Schamp equation can be readily applied to derive CCSs from the mobilities.

In case DTIMS is coupled to subsequent MS analysis, the measured total arrival time t_A is given as the sum of t_D and a V_D-independent contributor:

$$t_A = t_0 + \frac{L_D^2}{K V_D}, \tag{2.4}$$

where t_0 represents the time that may pass from the moment the ions exit the drift tube until the moment they eventually reach the detector. A common strategy for inferring t_D from the measured t_A is to perform the same DTIM-MS experiment at multiple V_D values. When plotting t_A as a function of the reciprocal V_D, a linear function may be fit to the data set. The intercept of this function yields the V_D-independent t_0, while K may be inferred from the slope of the function (see Figure 2.10). The above strategy may also be applied to stand-alone DTIMS to increase the accuracy of the measurements.

Indeed, this so-called stepped-field method represents the most accurate way of determining K and CCS values within the low-field limit experimentally, with expanded uncertainties reported as low as 0.5%.[176]

Although the above-mentioned features make DTIMS very attractive, enhancing resolving power requires increasingly long pathways and short injection pulses combined with high DC voltages, which may become impractical or difficult to achieve beyond a certain limit.[175]

Traveling wave ion mobility spectrometry (TWIMS). TWIMS is a widely-employed time-dispersive method where ions are driven through a gas-filled cell by the eponymous traveling potential waves.[177–179] In brief, the approximately sinusoidal waves traverse the mobility cell with velocities generally between 100 and 500 $\mathrm{m\,s^{-1}}$, while the ions follow their movement in a mobility-dependent manner. Analytes with higher K are able to "surf" longer on each wave, experiencing fewer discrete roll-over events and reaching higher average velocities. The electric field itself changes sign between the leading and trailing edges of each electric potential wave, causing the ion velocity vectors to fluctuate. This results in a characteristic "x steps forward, one step back" motion of the analytes. Due to this complex motion, the relation between the mobility and the average linear velocity of ions through the TWIMS cell is nonlinear and difficult to decipher, in contrast to the simple linear dependence prevailing in DTIMS.

Despite remarkable improvements in TWIMS theory[180,181], to date no complete and general analytical model has been developed that would allow for inferring mobilities directly from arrival times under a broad range of practical operating conditions. Thus, to obtain mobilities and CCSs, IMS instruments operating with traveling potential waves need to be calibrated. When performing TWIMS calibration, the relation between the reduced mass and charge-normalized CCS and the net transit time of ions through the mobility cell is usually approximated by the following power function:[182,183]

$$\frac{\mathrm{CCS}\sqrt{\mu}}{|z|} = a \cdot (t_\mathrm{D})^b. \tag{2.5}$$

The parameters a and b depend on measurement conditions (*e.g.* wave velocity and wave height), and can be determined by measuring the net t_D for a set of calibrant ions whose mobilities and CCSs are known from low-field DTIMS experiments.[184,185]

An advantage of TWIMS technology over DTIMS is the flexibility it enables in instrument geometry: cyclic arrangements or structures for lossless ion manipulations (SLIMs) with serpentine routes provide extremely long

separation pathways within compact architectures.[186,187] Such instruments may achieve resolving power values currently unattainable in linear drift tubes, allowing for the separation of glycan anomers in the gas phase.[188,189]

Although experimentally determined CCSs are highly useful to distinguish and identify analytes, they ultimately reduce molecular structures to a single value: an effective area. These areas are linked to the overall shape of ions, but do not carry direct, atomic level information about the underlying molecular structure. Without prior knowledge and based merely on experimentally determined CCSs, it is extremely difficult, if not impossible, to tell unambiguously whether two separated isomers differ in their conformation, configuration, or constitution. To obtain atomic level structural details with the help of CCSs, complementing theoretical approaches are indispensable. The strategy, in principle, is simple: experimentally determined CCSs are compared to those calculated for structural candidates generated by computational methods, and the model structures are evaluated on the basis of CCS agreement. This approach proved to be very helpful for the structural analysis of charged clusters[190–192], and has been successfully adopted for biomolecular ions.[31,193]

To calculate CCSs, the first, computationally less expensive methods treated the colliding partners as hard spheres, ignoring details of the interaction potentials.[190,194] The development of the trajectory method applying realistic interaction potentials put CCS calculations on a more solid physical basis, albeit at the expense of significant computational cost.[30] Since then, continuous improvements in theoretical methods and computational tools have manifested in increasingly fast and accurate CCS calculations in atomic and molecular gases.[30,195–199] Today, the main bottleneck for glycans is not the calculation of CCSs for model structures with satisfying accuracy (at least in common buffer gases), but the generation of reliable structural candidates. It requires state-of-the-art computational approaches, such as merging density functional calculations with advanced methods to explore the vast conformational space of glycan ions *in vacuo*.[42] However, as the computation of glycan structures is not in the focus of the present work, this exciting field of research is not discussed in detail.

As a final remark to CCSs, let us introduce a widespread terminology that will be also adopted herein. According to this system, the experimental or theoretical method applied to obtain a given CCS value may be specified in the superscript, while the buffer gas shall be defined in the subscript of the CCS notation.[172] As an example, $^{\mathrm{DT}}\mathrm{CCS}_{\mathrm{He}}$ refers to a value determined in He buffer gas by DTIMS or DTIM-MS, while $^{\mathrm{TW}}\mathrm{CCS}_{\mathrm{N2}}$ indicates a value obtained using a TWIMS instrument with N_2 as buffer gas.

2.5 Cold-ion infrared spectroscopy in helium droplets

Studying the interaction of matter with electromagnetic radiation in the infrared (IR) region has contributed significantly to our understanding of molecular structure. In principle, the energy of photons in the so-called mid-IR ranging from 400 to 4000 cm^{-1} is comparable to the differences between vibrational energy levels in molecules. Thus, resonant absorption of IR photons initiates vibrational excitation in the absorbing species. By probing transitions between their vibrational energy levels, IR spectroscopy may provide information on the functional groups, hydrogen bonding pattern, conformation, or symmetry of molecules. In general, a nonlinear molecule consisting of N atoms possesses $3N-6$ normal modes of vibration, while a linear molecule with the same number of atoms has $3N-5$ such fundamental modes. For a vibrational mode to be IR active, the vibrational excitation must be accompanied by a change in the electric dipole moment of the molecule. Considering larger species that consist of atoms of different elements, such as those studied in the present thesis, the above criterion is usually satisfied for several of their vibrational modes.

The quantum harmonic oscillator provides a simple picture of molecular vibrations in diatomics. In this model, vibrations are described as the periodic harmonic motion of the nuclei along the bond axis in a quadratic potential well.[200] The quantum mechanical treatment of this problem results in discrete, equally spaced vibrational energy levels:

$$E_v = \left(v + \frac{1}{2}\right) h\nu, \tag{2.6}$$

where h is the Planck constant, ν is the vibration frequency, and v is the vibrational quantum number, which may adopt non-negative integer values. While the quantum harmonic oscillator serves as a suitable first approximation, it ignores the anharmonicity of chemical bonds by default and fails to predict their dissociation above critical threshold energies. To overcome these limitations and describe the behavior of anharmonic oscillators, Morse suggested a more realistic potential that also includes bond dissociation explicitly.[201] As a result of anharmonicity, the vibrational energy levels do not appear equidistant, and the model successfully explains the occurrence of overtone and hot bands in IR spectra. Figure 2.11 portrays schematically the harmonic oscillator model and the Morse potential with the respective energy levels. Although the Morse potential is also limited to diatomics, we shall keep it in mind as a useful qualitative picture for larger species.

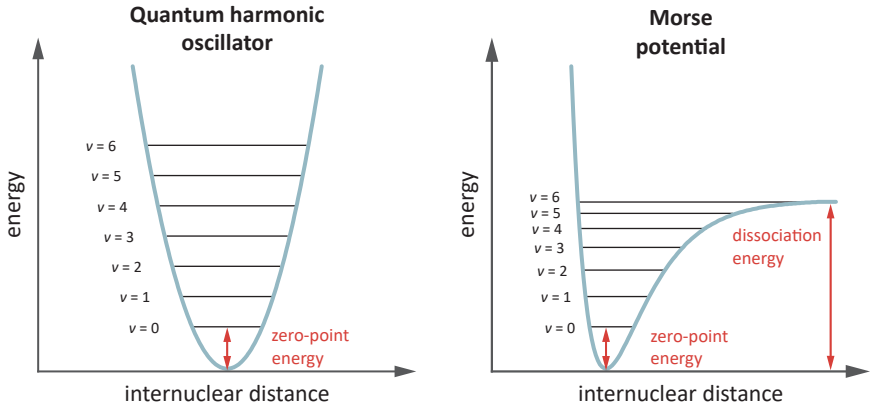

Figure 2.11: (left) The quantum harmonic oscillator model with equally spaced vibrational energy levels, and (right) the more realistic Morse potential which explicitly includes the bond dissociation energy.

In experiments where sufficiently large amounts of solid, liquid, or gaseous sample can be probed, IR spectra are generally recorded by measuring the attenuation of the incident radiation. According to the Beer–Lambert–Bouguer law, the difference between the intensities of the incident (I_0) and the transmitted (I_T) electromagnetic radiation is given as:

$$I_0 - I_T(\tilde{\nu}) = I_0 \left(1 - e^{-\sigma(\tilde{\nu})nl}\right), \tag{2.7}$$

where n is the number density of the absorbing species, l is the optical path length, and σ is the absorption cross section, with $\tilde{\nu}$ in parentheses indicating wavenumber-dependence. In general, such direct absorption spectroscopy experiments require number densities of at least 10^{10} absorbing molecules per cubic centimeter. When dealing with a cloud of isolated ions, however, Coulomb repulsion limits the maximally achievable number density to around 10^6 singly charged ions per cubic centimeter, which is orders of magnitude lower than that required for classical absorption spectroscopy.[37] Thus, to perform IR spectroscopy on ions in a mass spectrometer, a fundamentally different approach is required. In action spectroscopy, instead of looking at how the analytes affect the IR radiation, one may focus on how IR photons affect the analytes.[39] Vibrational excitation through resonant photon absorption often leads to changes in isolated systems which can be readily detected by mass spectrometry. By monitoring such photon-induced changes or actions as the function of the wavenumber, IR spectra of mass-selected ions can be recorded. Considering single-photon excitation in a two-level system where the lower level corresponds to the intact, unaffected ions, while the excited ions undergo with 100% probability the specific action that is being monitored, the number

of affected ions N_A can be given as:

$$N_\mathrm{A}(\tilde{\nu}) = N_0 \left(1 - e^{-\sigma(\tilde{\nu})H(\tilde{\nu})}\right). \tag{2.8}$$

In the above equation N_0 is the total number of ions, while H is the photon fluence, which may also exhibit some wavenumber-dependence. Although the situation in reality is often more complicated than implied by Eq. 2.8 (due to for example competing relaxation channels, multiple energy levels, or multiphoton action processes), it generally applies that the signal intensity depends on the number of ions undergoing photoexcitation and thus increases with increasing photon fluence. For this reason, IR action spectroscopy methods require intense radiation, which is generally provided by tunable laser systems, such as optical parametric oscillators and free-electron lasers.

Well-established IR action spectroscopy techniques include infrared multiphoton dissocation (IRMPD) spectroscopy[37,202–204], which is based on the fragmentation of vibrationally highly excited species, and messenger-tagging spectroscopy[205–208], where the photodissociation of weakly bound complexes formed at cryogenic temperatures between the ion and a suitable messenger (a rare gas atom or small gas molecule) serves as the specific action. A major advantage of the latter method is the absence of significant ion heating. The energy of a single IR photon generally suffices to detach the weakly bound messenger from the ion, thereby inducing an observable change in the m/z ratio. As a consequence, the recorded IR spectra reflect the initial temperature of the ion–messenger complex, which may be as low as a few kelvins in cryogenic ion traps. Cooling of ions is a highly effective way of reducing inhomogeneous spectral broadening, brought about by the elimination of hot bands and the decrease in the number of thermally populated conformers.[38] A powerful method that enables IR spectroscopic experiments on mass-selected ions at even lower, sub-kelvin temperatures, is cold-ion IR spectroscopy in superfluid He droplets.[40,43,44,209,210] Before discussing the operating principles of this technique that has been applied in the present work, we shall first explore the unique properties of He nanodroplets.

Helium, the second most abundant element in the universe, comes in the form of two stable isotopes: the rare, fermionic ^{3}He, and the abundant, bosonic ^{4}He. In this thesis with He we always refer to the bosonic isotope; ^{3}He has different physical properties and bears no relevance to the spectroscopic experiments presented herein. When expanding pressurized He gas into vacuum through a nozzle that is cooled to cryogenic temperatures, large He clusters containing $>10^3$ atoms can be formed. Such He nanodroplets produced in free jet expansions have an equilibrium temperature of 0.37 K, which they maintain through evaporative cooling.[211] According to the two-fluid theory

proposed by Tisza in 1938, liquid He at temperatures below the lambda point (2.17 K at 1 atm) can be described as the mixture of a normal fluid and a superfluid component, the latter having zero viscosity and entropy.[212,213] The two-fluid model of liquid He has been later confirmed experimentally, both in the bulk and in He nanodroplets.[214,215] In addition to their superfluidity and sub-kelvin equilibrium temperature, He droplets are completely transparent to electromagnetic radiation at photon energies below 20 eV, and are capable of capturing various ions and neutrals through inelastic collisions.[216–219] The energy of the collision and the thermal energy of the dopant is transferred to the droplet, which leads to the rapid evaporation of He atoms. While the size of the droplet decreases during evaporative cooling, its equilibrium temperature is maintained, and the entrapped species is rapidly cooled to 0.37 K.[211] The unique combination of the above-mentioned features inspired researchers to apply He droplets as cryogenic matrix for spectroscopic studies on a variety of molecules and molecular ions.[46,220–225] Owing to the superfluidity of He, dopants may freely rotate inside the droplets (with increased moment of inertia), and no significant spectral line broadening or shifts in the vibrational frequencies occur as compared to isolated species.[209,221,226] Thus, in terms of IR spectroscopy, superfluid He droplets can be considered transparent, noninteracting, mesoscopic cryostats that provide sub-kelvin temperatures for the embedded molecules and ions.

For recording optical spectra of ions captured in He droplets, one requires a suitable action fulfilling two requirements: it needs to be initiated by resonant photon absorption, and one should be able to efficiently monitor the action, preferably by means of MS. The first action spectroscopy experiments on He droplet-embedded ions revealed that the absorption of IR and UV photons can lead to the emergence of bare, intact ions from the droplets.[209,219,224,227] The released ionic species may be readily detected following m/z-analysis, and by plotting the ion release yield as a function of photon energy, it is possible to reconstruct highly resolved optical spectra of cold, mass-selected ions. Although many details of this ion release mechanism are still unresolved, we may explore important aspects of cold-ion IR spectroscopy through a simplified view at the processes initiated by IR photon absorption in a single molecular ion trapped in a He droplet. Figure 2.12 provides a schematic overview of the processes involved, accompanied by a brief description below. Following ion capture and thermalization to 0.37 K, the embedded species is in its vibrational ground state. Next, absorption of a resonant IR photon leads to the selective excitation of a certain vibrational mode in the ion. Through vibration–phonon coupling the energy of the absorbed photon gets rapidly dissipated to the droplet, which leads to the heating of the latter and the relaxation of the dopant to the ground state. Finally, the droplet

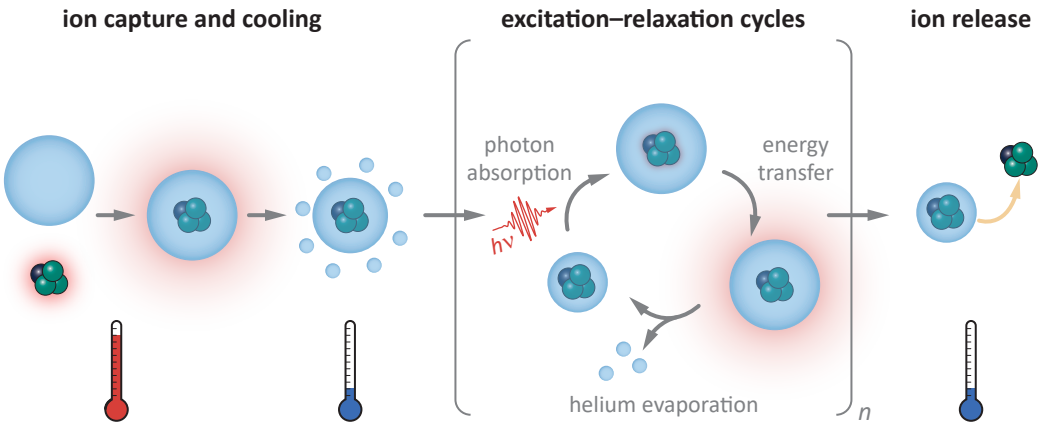

Figure 2.12: Schematic representation of the action process in cold-ion IR spectroscopy using He droplets. First, a molecular ion is captured by a superfluid He droplet and cooled to its equilibrium temperature of 0.37 K. Resonant IR photon absorption then leads to the vibrational excitation of the ion, followed by the transfer of the absorbed energy to the droplet through vibration–phonon coupling. The dopant–droplet system finally regains its initial temperature through evaporative cooling, and is ready for the absorption of the next photon, initiating a new cycle. After a sufficient number of cycles, the ion is released from the droplet. Plotting the ion release yield as a function of photon energy provides highly resolved IR spectra of ions at sub-kelvin temperature.

undergoes evaporative cooling, whereby the system regains its equilibrium temperature of 0.37 K. This process may repeat several times, as rapid cycles of photoexcitation, energy transfer, and He evaporation ensure that the embedded ion always returns to its ground state and initial temperature, at the expense of a decreasing droplet size. Considering a heat of evaporation of $5\,\mathrm{cm}^{-1}$,[211,228] the energy of an IR photon at $1000\,\mathrm{cm}^{-1}$ would suffice to evaporate 200 He atoms. Thus, boiling off an entire droplet consisting of 10^5 He atoms would require 500 photons with the aforementioned energy. Experimental results, however, strongly indicate that ions may get released from the droplets before the complete evaporation of the latter, *i.e.* due to an apparently nonthermal ejection process.[224]

Importantly, and regardless of whether ion release is a thermal or non-thermal phenomenon, cold-ion IR spectroscopy in He droplets involves no vibrational ladder climbing or highly excited species when combined with a suitable laser system. Cooling ions to sub-kelvin temperatures thus efficiently reduces inhomogeneous thermal broadening, with the recorded IR spectra reflecting the vibrational ground state of the dopants. Such highly resolved vibrational spectra of cold, mass-selected molecular ions can reveal details about their underlying structure that might otherwise remained unresolved when measuring simply m/z ratios. In addition, being ultimately an MS-based

technique, cold-ion IR spectroscopy requires only minute sample amounts, and can efficiently cope with mixtures and impurities. As oligosaccharides are often available only in limited quantities or as components of complex biological samples, the combination of these attractive features make cold-ion IR spectroscopy a promising technique for glycan structure analysis.

Chapter 3

Experimental methods

This chapter provides an overview of the instruments employed in the herein presented work, accompanied by a brief description of materials and methods used in the experiments. We discuss two drift tube ion mobility-mass spectrometers that were applied in connection of the plate-height model for ion mobility separations. In addition, we describe the layout and operating principles of a mass spectrometry-based setup that utilizes superfluid helium droplets as cryogenic matrix to record high resolution infrared spectra of mass-selected ions at sub-kelvin temperatures.

3.1 iMob: a custom-built ion mobility-mass spectrometer

A significant part of this thesis, Chapter 4, is dedicated entirely to an analytical model assessing the efficiency of ion mobility separations. In connection to this mainly theoretical work, a series of experiments were performed and compared to calculations to evaluate the accuracy of the latter. For this purpose, we employed a drift tube ion mobility quadrupole time-of-flight mass spectrometer, referred to herein simply as iMob (see Figure 3.1). The experimental setup and details of the measurements are discussed below.

In this custom-built DTIM-MS instrument, ions are generated using a linear nano-electrospray ion source (nESI) with Pt/Pd-coated spray emitters prepared in-house from borosilicate glass capillaries. The charged analytes are collected, radially focused, and trapped by a ring electrode radio frequency (RF) ion funnel. This four-stage entrance funnel also serves for the injection of discrete ion packets with defined pulse-width into the drift region, generally at a rate of 10 to 20 Hz. The 805.5 mm long drift cell consists of a series of conductive glass tubes (Photonis, USA), and was filled with He buffer gas (99.999% purity). The temperature in the drift region is monitored with a Pt100 resistance thermometer, attached to the drift cell from the outside. Being critical in IMS experiments, the buffer gas pressure is monitored with a high-precision MKS Baratron absolute pressure gauge (type 627). To avoid contamination of the buffer gas inside the drift region, an absolute pressure difference of 0.6 mbar is maintained between the drift tube and the entrance funnel. Measurements were performed within the low-field regime, with reduced electric field strengths between 1.6 and 19.3 Td. Connected to the drift cell, a second electrodynamic ion funnel (exit funnel, 144 mm in length) serves for the radial confinement of ion clouds, thereby facilitating ion transport through the conductance limit. Pressure and temperature inside the exit funnel and the the drift cell are essentially identical.

Having passed the conductance limit following the exit funnel, ions are transmitted through two differentially pumped stages by ring electrode ion guides, and eventually reach the high vacuum region of the instrument. Here, a quadrupole mass filter and another quadrupole ion guide of identical dimensions enable m/z-selection and the efficient transport of ions. The ions then pass an einzel lens stack and a set of steering lenses before finally being detected with an off-axis electron multiplier. Another possibility offered by the setup is to pulse the ions into an orthogonal Wiley–McLaren time-of-flight (ToF) mass analyzer. The latter operation mode, however, was not applied since significantly higher sampling rates are possible without ToF analysis.

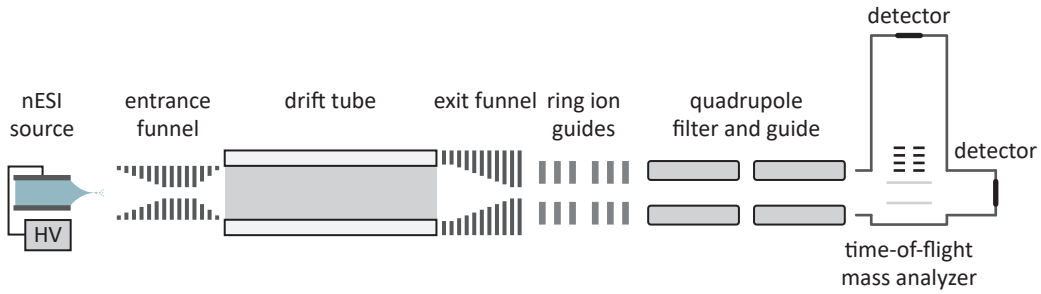

Figure 3.1: Schematic depiction of the iMob, a drift tube ion mobility quadrupole time-of-flight mass spectrometer.

Hardware and data acquisition were controlled using an in-house developed LabView software, while data analysis and calculations were performed using the Origin 2017 software package (OriginLab Co., Northampton, US). Each arrival time distribution (ATD) was fitted with a Gaussian function to determine the centroid arrival time, the temporal standard deviation, and the width of the distribution at its half maximum. Mobilities were determined using the stepped-field method and the respective ${}^{\mathrm{DT}}\mathrm{CCS}_{\mathrm{He}}$ values were calculated according to the Mason–Schamp equation. A main advantage of the iMob over commercial DTIM-MS devices is that if offers control over virtually every experimental parameter, which proved to be essential for testing the theoretical model and the impact of various measurement conditions.

For the experiments discussed in this thesis, three singly charged cations were chosen as model analytes: protonated 12-crown-4 with $m/z = 177$ and ${}^{\mathrm{DT}}\mathrm{CCS}_{\mathrm{He}} = 74\,\text{Å}^2$ (in the followings referred to as analyte **#1**), the Na^+ adduct of a dextran-derived trisaccharide with $m/z = 527$ and ${}^{\mathrm{DT}}\mathrm{CCS}_{\mathrm{He}} = 139\,\text{Å}^2$ (analyte **#2**), and the tetrabutylammonium iodide trimer $[(\mathrm{TBA})_3\mathrm{I}_2]^+$ with $m/z = 980$ and ${}^{\mathrm{DT}}\mathrm{CCS}_{\mathrm{He}} = 270\,\text{Å}^2$ (analyte **#3**). The ions exhibited unimodal ATDs in the experiments, and the ${}^{\mathrm{DT}}\mathrm{CCS}_{\mathrm{He}}$ values show equirational progression. Chemicals to generate the above analytes using nESI were obtained from commercial vendors: dextran purified from *Leuconostoc mesenteroides* (analytical standard for GPC, average $M_{\mathrm{W}} = 1000\,\mathrm{Da}$), tetrabutylammonium iodide (TBAI, $\geq 99.0\%$ purity), and 12-crown-4 (98% purity). Each compound was dissolved in a water/methanol 50/50 (v/v) solution containing 0.1% formic acid. The following concentrations were used in the measurements: 500 µM for 12-crown-4, $1\,\mathrm{mg\,mL^{-1}}$ for dextran, and 200 µM for TBAI.

3.2 Modified Synapt G2-S ion mobility-mass spectrometer

Chapter 4 also involves experiments with fluorescently labeled glycans on a modified Synapt G2-S HDMS instrument (Waters Co., Manchester, UK). This IM-MS device is equipped with a double orthogonal nESI source (ZSpray™), which is followed by the StepWave™ ion guide that transports ions from the source region to a quadrupole mass filter through differential pumping stages. In Synapt G2-S instruments, ion transport at elevated pressures is generally accomplished using such ring electrode ion guides, operated with traveling potential waves. Following their passage through the quadrupole, the potentially m/z-selected ions enter the TriWave™ unit. Serving as the heart of the instrument, the TriWave™ consists of an ion mobility cell that is sandwiched between two ring ion guides, the so-called trap and transfer cells. These are filled with Ar gas at pressures on the order of 10^{-2} mbar, and besides facilitating ion transport, they may also be applied as collision cells to perform collision-induced dissociation (CID) prior or subsequent to ion mobility separation. Thus, the setup resembles a conventional hybrid quadrupole ToF MS instrument, the simple collision cell between the quadrupole mass filter and the ToF analyzer being replaced by the TriWave™ unit.

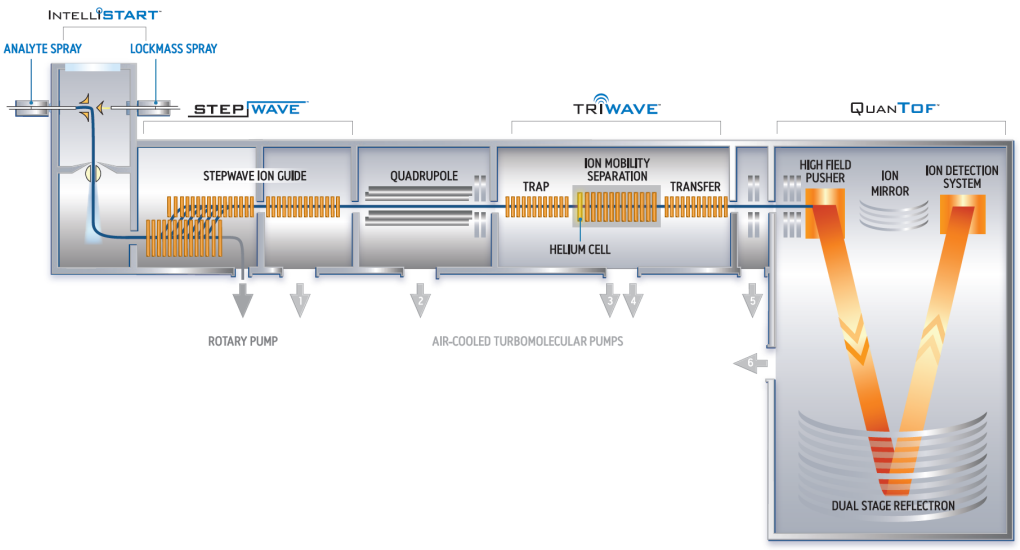

Figure 3.2: Schematic overview of the Waters Synapt G2-S ion mobility mass spectrometer. In the instrument employed herein, the original traveling wave cell was replaced by an RF-confining drift cell, enabling the determination of ion mobilities and collision cross sections without calibration. Illustration provided by the Waters Corporation.

In the most widespread, commercially available version of Synapt instruments, ion mobility separation is based on the traveling wave technology.[178] In the modified version employed herein, the TWIMS cell was replaced by an RF-confining drift cell that consists of 168 gold-coated ring electrodes, each connected to printed circuit boards.[229] The axial drift of analytes in the 250.5 mm long drift region is governed by a constant DC field, while the ion clouds are kept radially confined during the whole DTIM separation by RF potentials. Owing to the latter, no ion funnel need to be placed after the drift cell as in case of DC-only drift tubes. In general, the drift cell is filled with He or N_2 as buffer gas at pressures between 2.4 and 3 mbar. A great advantage of the modified setup is that Eqs. 2.2 and 2.4 remain valid in DTIM-MS, allowing for the determination of ion mobilities and ^{DT}CCS values without calibration.

Following separation and potential fragmentation in the TriWave™, ions finally reach the high resolution reflectron ToF mass analyzer. As the timescale of ToF analyses is in general over an order of magnitude shorter than the temporal width of the ions' arrival time distribution, several mass spectra can be recorded for each peak in the ion mobility spectrum. Thus, in so-called nested IM-MS experiments the Synapt G2-S can provide information on the mass, charge, and mobility of a large number of intact and fragment ions simultaneously. A schematic representation of the instrument is provided in Figure 3.2.

3.3 HeDrop: an instrument for ion spectroscopy at sub-kelvin temperatures

In the present thesis, Chapter 5 is dedicated to IR spectroscopic studies on mass-selected glycosaminoglycan anions at cryogenic temperatures. This section provides a general overview of the HeDrop instrument, a unique setup that enables cold-ion IR spectroscopy experiments in superfluid He droplets (see Figure 3.3). While this section does not aim to give a detailed description of the experimental setup's various constituent parts, the basic layout of the HeDrop and details of the experiments are briefly discussed to provide suitable background for the results presented in subsequent chapters.

The front end of the HeDrop is based on a commercial Waters Ultima quadrupole time-of-flight mass spectrometer (Waters Co., Manchester, UK), equipped with a a double orthogonal nESI source. To produce negatively charged glycosaminoglycan ions, a voltage between -0.7 and $-1.1\,\mathrm{kV}$ is generally applied to the nESI needle containing a $50\,\mu\mathrm{M}$ solution of the respective compound. Emitter tips were prepared in-house from borosilicate glass capillaries using a Flaming/Brown P-1000 micropipette puller (Sutter Instrument, Novato, USA), and were coated with Pt/Pd alloy employing a Cressington 108auto sputter coater (Cressington Scientific Instruments, Watford, UK). Following ionization, the analytes are transferred to vacuum through two differentially pumped chambers using ring electrode ion guides. At the next stage, a quadrupole mass filter enables the selection of ions with defined m/z ratios up to 2000 Th. The mass-selected analytes then pass through a hexapole ion guide and are focused by an einzel lens before reaching the quadrupole bender, where the ion beam is deflected by 90°.

Following deflection, the ions are collected in a variable temperature hexapole ion trap, where they are thermalized through collisions with He buffer gas. During the accumulation of ions, the pressure in this compartment is estimated to be on the order of 10^{-4} mbar, and at the space charge limit the trap may contain the equivalent of approximately 10^7 singly charged ions. Enclosed in a copper-housing, the trap can be routinely cooled with a flow of cold N_2 gas down to temperatures around 90 K, which we employed to reduce the number of thermally populated conformers of the ions prior to pick-up by He droplets.

Superfluid He droplets are produced by a pulsed droplet source based on a cryogenic Even–Lavie valve.[230] The valve is cooled by a closed cycle He cryocooler, and by adjusting its temperature, one can efficiently control the size of the generated droplets. For experiments reported in this thesis, droplets with an average size of 10^5 He atoms and an average linear velocity

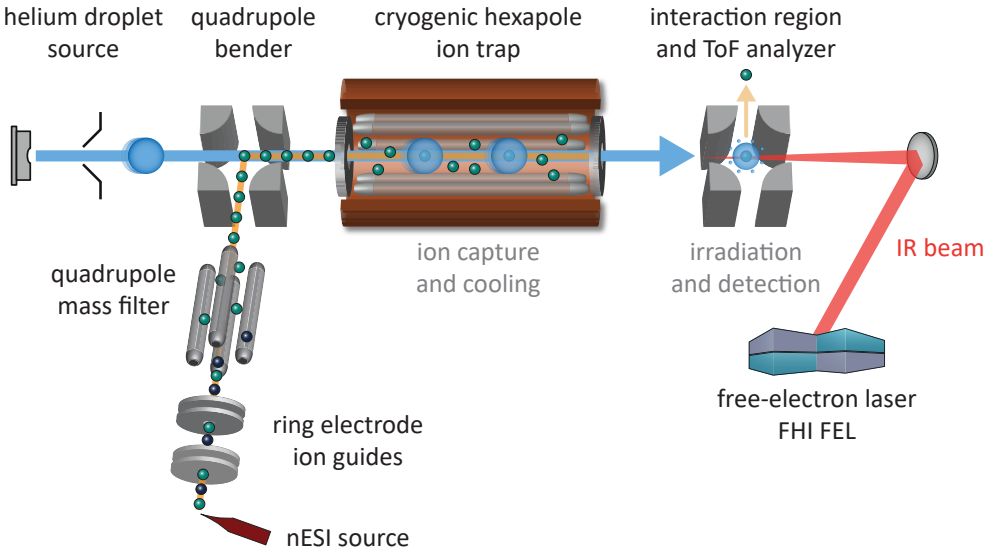

Figure 3.3: Simplified schematic layout of the HeDrop instrument. Figure adapted with permission from M. Lettow, M. Grabarics, K. Greis, E. Mucha, D. A. Thomas, P. Chopra, G.-J. Boons, R. Karlsson, J. E. Turnbull, G. Meijer, R. L. Miller, G. von Helden, K. Pagel, *Analytical Chemistry* **2020**, *92*, 10228–10232. Copyright 2020 American Chemical Society.

of around 450 m s^{-1} were employed. Considering these figures, a typical He droplet in the experiments thus possessed roughly 400 eV kinetic energy. The beam of He droplets is transmitted to the hexapole ion trap using a skimmer, where they can capture the accumulated ions through inelastic collisions. The high kinetic energy of the doped droplets enables them to overcome the axial trapping potential, which is on the order of a few volts. Droplet-embedded ions thus eventually reach the region downstream of the ion trap, where they may interact with an intense IR laser beam. This experimental solution utilizing the kinetic energy of the traversing droplets for ion release ensures that the charged analytes may only escape the trap and reach the interaction region when embedded in a He droplet.

Once in the interaction region, a suitable ion guide downstream of the trap, the doped droplets are irradiated by a beam of IR photons coming from the Fritz Haber Institute Free-Electron Laser (FHI FEL).[231] In principle, to perform IR action spectroscopy based on a multiphoton process, one requires intense, monochromatic radiation that is tunable over the desired wavenumber range. Unfortunately, as conventional lasers rely on population inversion between discrete energy levels in atomic and molecular gain media, the quantization of energy imposes restrictions on the achievable photon energies in their case. In contrast to traditional benchtop lasers, the active medium of FELs are eponymous free electrons. As the kinetic energy of

free electrons may be varied continuously over several orders of magnitude, the aforementioned constraints on photon energies and tuning range are lifted. Since the first successful lasing using the principle in 1977, FELs have proven to be extremely useful sources of bright, broadly tunable, coherent, and polarized radiation over a wide range of photon energies.[232–236] Being an essential part of the cold-ion IR spectroscopy setup, the basic layout and characteristics of the FHI FEL, shown schematically in Figure 3.4, are briefly discussed.

A gridded thermionic gun emits bunches of free electrons, which are subsequently compressed in a subharmonic buncher cavity and brought to relativistic energies using two linear accelerators (LINACs). The first LINAC accelerates the electrons to a nominal energy of 20 MeV, while in the second stage the kinetic energy is adjusted to the final value between 15 and 50 MeV. For the experiments reported in this thesis, electrons were accelerated to around 36 MeV. The beam of relativistic electrons is then delivered through a magnetic deflecting system into the 2 m long mid-IR undulator, placed inside an optical cavity. The undulator is a periodic array of oppositely poled dipole magnets, which creates a strong static magnetic field. Owing to the Lorentz force, the periodic magnetic field coerces the electrons onto a sinusoidal path. As the undulator is located inside an IR cavity, the initial monochromatic but incoherent synchrotron radiation emitted by the wiggling electrons is reflected by cavity end mirrors. Through careful adjustment of the cavity length, it is possible to synchronize the motion of the reflected photons with that of a subsequent electron bunch entering the undulator, enabling them to interact along their way through the periodic magnet structure. This interaction between the electromagnetic field of the IR pulse and the relativistic electrons causes the micro-bunching of the latter, leading to the emission of intense, coherent IR radiation. Finally, a fraction of the radiation can be extracted through a suitable outcoupling mirror, enabling it to be used in action spectroscopy experiments. The IR beam of the FHI FEL has a characteristic pulse-structure, determined by the macro- and micro-repetition rate of the electron gun. Macro-pulses are 10 µs long and occur at a typical repetition rate of 10 Hz, with pulse energies on the order of 100 mJ. Each macro-pulse consists of 10^4 micro-pulses with widths on the order of 10^{-12} s, separated evenly by 1 ns. This pulse-structure enables doped droplets to return to their initial temperature of 0.37 K between the arrival of subsequent micro-pulses. During spectroscopic experiments, the electron energy is kept constant, and photon energies are tuned by adjusting the gap between the magnets of the undulator. To record the IR spectra reported in this thesis, the wavenumber of the FEL radiation was changed between 1000 and 1800 cm^{-1}.

In case the incident laser radiation is in resonance with a sufficiently

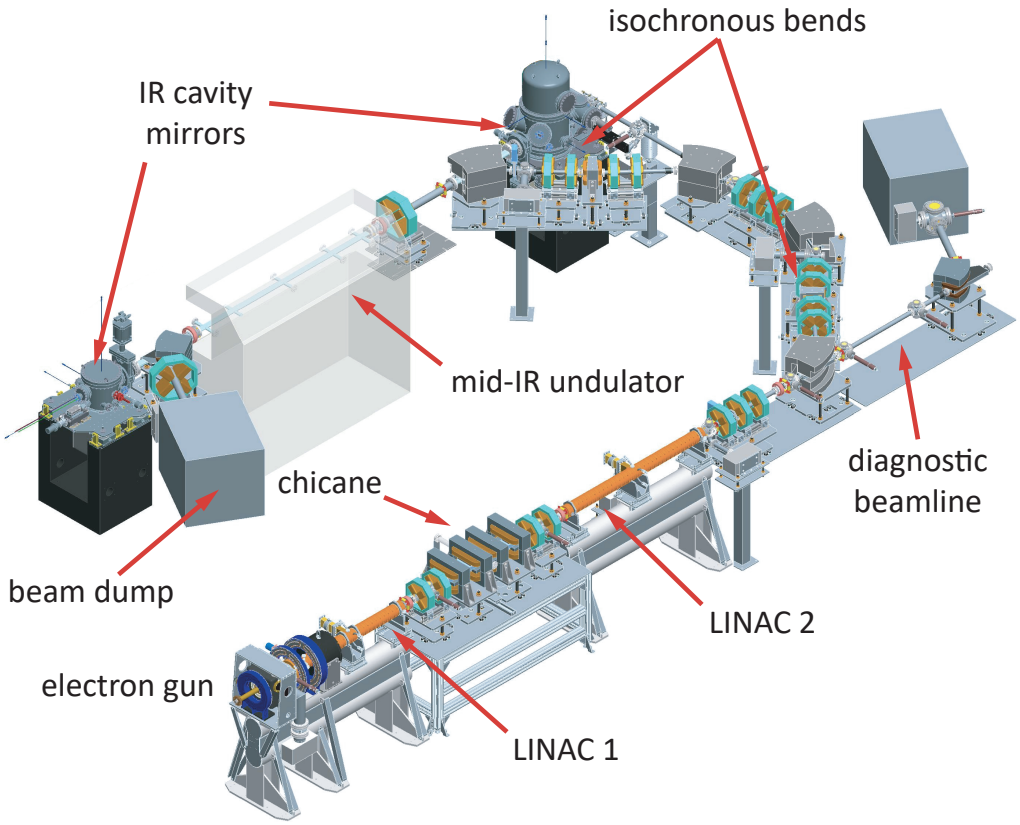

Figure 3.4: Schematic overview of the Fritz Haber Institute Free-Electron Laser. Figure adapted from reference [231].

strong IR active vibrational transition of the dopant, sequential absorption of multiple photons can finally lead to the release of ions from the droplets. The ions released in the interaction region are then accelerated to a defined kinetic energy, matching the magnitude of the DC voltages applied to the electrodes of a quadrupole bender. The deflected ion beam is focused by einzel lenses and guided towards a Micromass ToF mass analyzer, where the ions are separated according to their m/z-values and finally reach the detector. The ion release being a reporter for photon absorption, IR spectra of cold, mass-selected ions are obtained by plotting the signal intensity for the respective species as a function of the incident photon energy.

Chapter 4

A plate-height model for ion mobility separations

In this chapter we aim to develop a plate-height model for ion mobility separations. For this purpose, we borrow concepts and mathematical frameworks from chromatography, and combine them with physical models rooted in the fundamental laws governing ion transport in gases. We explore zone broadening, peak-to-peak resolution, and peak capacity, the three key aspects of ion mobility separations. Finally, the utility of the model is demonstrated through a practical example of glycan analysis. By employing the plate-height concept for ion mobility separations, we wish to find a common ground between this emerging separation technique and such well-established methods as chromatography or zone electrophoresis.

Chapter 4 is based on the following publications:

C. Manz, M. Grabarics, F. Hoberg, M. Pugini, A. Stuckmann, W. B. Struwe, K. Pagel; Separation of isomeric glycans by ion mobility spectrometry – the impact of fluorescent labelling, *Analyst* **2019**, *144*, 5292–5298.

M. Grabarics, M. Lettow, A. T. Kirk, G. von Helden, T. J. Causon, K. Pagel; Plate-height model of ion mobility-mass spectrometry, *Analyst* **2020**, *145*, 6313–6333.

M. Grabarics, M. Lettow, A. T. Kirk, G. von Helden, T. J. Causon, K. Pagel; Plate-height model of ion mobility-mass spectrometry: Part 2. Peak-to-peak resolution and peak capacity, *Journal of Separation Science* **2021**, *44*, 2798–2813.

4.1 Birth and evolution of the theoretical plate concept

Theoretical plates are generally associated with chromatography. The concept, however, was originally introduced by Lewis and Peters to describe distillation in fractionating columns and evaluate the efficiency of such methods.[237–239] Drawing an analogy between the processes occurring in distillation columns and those governing chromatographic elution, Martin and Synge adopted the theoretical plate concept to the latter technique and developed an approximate theory of chromatography.[240] In this theory, the chromatographic column is divided into a finite number of virtual equilibrating stages, the theoretical plates, and elution of the solutes is described as mass transfer between these compartments. Division of the column length with the number of discrete stages yields the height equivalent to a theoretical plate (HETP) or shortly plate height. This simple view of the chromatographic elution process proved to be extremely fruitful, catalysing intense research and debate within the chromatography community.[241,242] For their seminal work in chromatography, Martin and Synge were awarded the Nobel Prize in Chemistry in 1952.

Besides its historical importance and undeniable merits, the plate theory also suffers from inherent shortcomings. They stem from the misleading physical picture behind the model, as in reality no discrete equilibrating stages are present in chromatographic columns. To overcome these limitations, more advanced macroscopic and microscopic theories have been developed since, such as van Deemter's rate model or the stochastic theory of chromatography.[243–248] While these theories do not view the column as a series of discrete stages, theoretical plates and the plate height were retained as measures of column efficiency for historical continuity and practical reasons.[36]

Through the pioneering work of Calvin Giddings, theoretical plates and the plate height as indices of separation efficiency became adopted to various other differential migration techniques, such as sedimentation, electrophoresis, and field-flow fractionation.[36,249] In principle, these measures may be readily applied to any differential migration methods, provided linear interactions dominate, *i.e.* zone broadening is the result of independently acting dispersion processes. In such systems, the total variance of a zone is given as the sum of variances associated with the individual dispersion processes:

$$\sigma^2_{\text{total}} = \sum_i \sigma^2_i. \tag{4.1}$$

In general, plate-height models are simple analytical models that calculate zone dispersion through the addition of variances. From the zone variance a

set of highly useful measures can be derived, providing a unified framework to evaluate and compare the efficiency of different separation techniques. Not surprisingly, plate-height models have been most prominent in the field of chromatography.[243,250–256] Owing to their simplicity and flexibility, however, they have been also applied to other zonal separation methods, considering of course quite different physical processes that are specific to the respective technique.[36,257–260]

In capillary electrophoresis, strong nonlinear phenomena (most prominently electromigration dispersion) often limit the utility and accuracy of plate-height models.[261–265] In contrast to its solution-based counterpart, nonlinear effects are relatively weak in low-field DTIMS, molecular diffusion being clearly the dominant intrinsic dispersion process. These fortunate characteristics make DTIM separations highly suited to be described through plate-height models, which we attempt to accomplish herein.

4.2 Zone broadening and theoretical plates in ion mobility separations

Inspired by the well-known models of chromatography, in Section 4.2 we present a simple analytical model to describe zone broadening in DTIM separations. We start by quantifying the effects of major dispersion processes, *i.e.* factors that contribute to the total width of peaks and determine the number of theoretical plates in this separation technique. Building on these findings, we formulate plate-height equations for stand-alone DTIMS and DTIM-MS, and test their accuracy by comparison with experiments. Finally, we explore the plate-height model through extensive calculations, revealing the influence of key experimental parameters on the separation efficiency.

4.2.1 Measures of zone broadening

In general, peaks or arrival time distributions (ATDs) in DTIMS converge to a Gaussian profile. Besides the dominant influence of diffusion, this convergence is also facilitated by the large number of independently acting dispersion processes according to the central limit theorem of statistics. Except for some extraordinary and practically less relevant cases, *e.g.* when injection pulses are abnormally long or space charge effects become so strong to surpass diffusional broadening, the axial distribution of ions at the end of the separation can be adequately described by a Gaussian function. The width of a Gaussian alone, however, does not reflect the separation efficiency adequately. To obtain a more accurate picture, the temporal or spatial width of a zone needs to be related to the time or distance covered during the separation. In the plate-height model we use three such measures that relate dispersion to migration, described in detail below.

Height equivalent to a theoretical plate. Adopted from fractionating columns to chromatography, the height equivalent to a theoretical plate (HETP) or shortly plate height was originally linked to virtual equilibration stages in a column.[240] To detach it from the constraints of a physical model that does not reflect accurately the chromatographic elution process, the plate height may instead be defined as the increase in spatial variance per unit migration distance:[36,266]

$$\mathrm{HETP}_{\mathrm{local}} = \frac{\mathrm{d}\sigma_{\mathrm{L}}^2}{\mathrm{d}L}. \tag{4.2}$$

The subscript indicates that $\mathrm{HETP}_{\mathrm{local}}$ is defined as a derivative with respect to spatial position. $\mathrm{HETP}_{\mathrm{local}}$ has a dimension of length, generally measured

in μm, and we may interpret it as the rate of generating spatial variance. If extrinsic factors contributing to the total variance are absent, and the separation field is completely uniform, *i.e.* there are no spatial variations in $\mathrm{d}\sigma_\mathrm{L}^2/\mathrm{d}L$, $\mathrm{HETP}_\mathrm{local}$ equals the experimentally observed apparent plate height:[36,266]

$$\mathrm{HETP}_\mathrm{app} = \frac{\sigma_\mathrm{t}^2}{t^2} L. \tag{4.3}$$

Here, σ_t^2 is the total temporal variance generated from injection to detection, t is the total time spent in the separation region, and L is the total migration distance covered during this time. If zone velocities do not vary between discrete sections of the separation region, $\mathrm{HETP}_\mathrm{app}$ can be written in the following form:

$$\begin{aligned} \mathrm{HETP}_\mathrm{app} &= \frac{\sigma_\mathrm{L}^2}{L^2} L \\ &= \frac{\sigma_\mathrm{L}^2}{L}, \end{aligned} \tag{4.4}$$

where σ_L^2 is the total spatial variance. These abstract definitions given above are not associated with physical models and thus are not limited to chromatography. They can be readily adopted to various other differential migration methods[249], and will be applied to DTIM separations herein.

Importantly, the conditions when $\mathrm{HETP}_\mathrm{app} = \mathrm{HETP}_\mathrm{local}$ are often not met in ion mobility separations or even in chromatography in practice.[267] Extrinsic contributors become often significant, and the separation field may be nonuniform for various reasons. For example, if the width of zones in DTIMS were determined exclusively by diffusion in the drift tube in presence of a perfectly homogeneous electric field, $\mathrm{HETP}_\mathrm{app}$ and $\mathrm{HETP}_\mathrm{local}$ would indeed be equal. In reality, however, the injection pulse-width is a non-negligible extrinsic source of variance, and $\mathrm{HETP}_\mathrm{local}$ may also vary between sections of the separation region due to for example variations in the electric field strength (see the treatment of the exit funnel in Section 4.2.2). For clarity, the terms "plate height" and "HETP" in the followings will always refer to the experimental observable $\mathrm{HETP}_\mathrm{app}$ (Eqs. 4.3 and 4.4), and not to the local derivative $\mathrm{HETP}_\mathrm{local}$ (Eq. 4.2). The subscript of $\mathrm{HETP}_\mathrm{app}$ will thus be omitted in the rest of Chapter 4.

Number of theoretical plates. The plate number N is a dimensionless measure of zone broadening, defined as

$$N = \frac{t^2}{\sigma_\mathrm{t}^2}. \tag{4.5}$$

If zone velocities are invariable across discrete sections of the separation region, we may also write:

$$N = \frac{L^2}{\sigma_{\mathrm{L}}^2}. \tag{4.6}$$

In cases when the velocities vary, the above spatial quantities need to be corrected accordingly (see Eqs. 4.37 and 4.38 on page 57). N is an experimental observable that reflects the ratio of two antagonistic processes, migration and dispersion. We may interpret it as resistance towards broadening: the larger its value, the sharper the zone and thus the more efficient the separation method. Like HETP, N is defined based on a single peak, and may vary significantly across a chromatogram or ion mobility spectrum, adopting different values for different analytes undergoing the same separation. When calculating the total number of plates in plate-height models, we may derive an upper N limit for each independent dispersion process through the respective variance. Variances being additive, the reciprocal of these limits may be summed together to yield the reciprocal total plate count:

$$\frac{1}{N_{\mathrm{total}}} = \sum_i \frac{1}{N_{\mathrm{i}}}. \tag{4.7}$$

Resolving power. The resolving power R_{P} is another dimensionless measure of zone spreading, defined as

$$R_{\mathrm{P}} = \frac{t}{w_{\mathrm{t}}}, \tag{4.8}$$

where w_{t} is the temporal full-width at half-maximum (FWHM) of a Gaussian. R_{P} may also be defined using the respective spatial quantity, w_{L}. Based on the relation $w = \sigma\sqrt{8\ln 2}$ for Gaussians, R_{P} can be readily obtained from N:

$$R_{\mathrm{P}} = \sqrt{\frac{N}{8\ln 2}}. \tag{4.9}$$

Similarly to N, we may also derive an upper R_{P} limit for each independent dispersion process. Unlike variances, however, squared FWHM values are additive only for Gaussian distributions. Thus, when a dispersion process leads to a non-Gaussian (*e.g.* rectangular, quadratic, *etc.*) function, the R_{P} limit must always be derived from the respective N limit according to Eq. 4.9, instead of substituting the FWHM of the distribution into Eq. 4.8. This approach is equivalent to calculating w for a Gaussian that has the same variance as the respective non-Gaussian distribution, and ensures that the square of reciprocal R_{P} limits are additive.

In general, while HETP and N are preferred in chromatography, R_P is more widespread in the IMS literature. To address both communities, in the present work we apply all three figures of merit as defined above.

4.2.2 Dispersion processes

In the present section, the most important dispersion processes and their influence on zone broadening in DTIM separations are discussed in detail. Longitudinal diffusion, the finite width of the injection pulse, Coulomb repulsion, electric field inhomogeneities, and dispersion in the exit funnel all contribute to the total variance of peaks. Combined, these physical processes thus determine the number of theoretical plates achievable in DTIM separations. To quantify the effect of said processes and calculate the corresponding variances, equations are derived from first principles, forming the physical basis of the plate-height model. Integrated into a mathematical framework adopted from chromatography, these findings enable the formulation of adequate plate-height equations for DTIMS and DTIM-MS, presented in Section 4.2.3.

Equations in the present section are valid only within the low-field regime. Under such circumstances, ion–neutral collisions are essentially thermal, and ion mobilities are basically independent of the electric field strength.

Longitudinal diffusion. Longitudinal diffusion is considered as the main intrinsic dispersion process in DTIM separations.[28,268–270] Besides being responsible for a significant portion of the total variance, diffusional spreading of ion clouds also contributes to the convergence of ATDs to a Gaussian profile.

To obtain a formula for $\sigma^2_{\mathrm{L,diff}}$, the spatial variance due to longitudinal diffusion in the drift cell, we may substitute the expression for the drift time from

$$t_{\mathrm{D}} = \frac{L_{\mathrm{D}}^2}{K V_{\mathrm{D}}} \tag{4.10}$$

into the relation

$$\sigma^2_{\mathrm{L,diff}} = 2 D t_{\mathrm{D}}, \tag{4.11}$$

and finally write:

$$\sigma^2_{\mathrm{L,diff}} = L_{\mathrm{D}}^2 \frac{2D}{K V_{\mathrm{D}}}. \tag{4.12}$$

Here, L_{D} is the length of the drift cell, V_{D} is the drift voltage, while K and D are the mobility and diffusion coefficient of the ions, respectively. Employing

the Nernst–Einstein–Townsend (NET) relation,

$$K = \frac{Dq}{k_{\mathrm{B}}T}, \tag{4.13}$$

where q is the ion's charge, k_{B} is the Boltzmann constant, and T is the ion temperature (assumed to equal the buffer gas temperature below the low-field limit), we may eliminate the transport properties D and K from Eq. 4.12 to arrive at the following alternative formula:

$$\sigma^2_{\mathrm{L,diff}} = L^2_{\mathrm{D}} \frac{2k_{\mathrm{B}}T}{qV_{\mathrm{D}}}. \tag{4.14}$$

Combining Eqs. 4.12 and 4.14 with the definitions in Section 4.2.1, the diffusion limit of theoretical plates, N_{diff}, and the diffusion limited resolving power, $R_{\mathrm{P,diff}}$, can be finally expressed:

$$\begin{aligned} N_{\mathrm{diff}} &= \frac{KV_{\mathrm{D}}}{2D} \\ &= \frac{qV_{\mathrm{D}}}{2k_{\mathrm{B}}T}, \end{aligned} \tag{4.15}$$

$$\begin{aligned} R_{\mathrm{P,diff}} &= \sqrt{\frac{KV_{\mathrm{D}}}{16D\ln 2}} \\ &= \sqrt{\frac{qV_{\mathrm{D}}}{16k_{\mathrm{B}}T\ln 2}}. \end{aligned} \tag{4.16}$$

The above expressions are analogous to those of zone electrophoresis, for which the corresponding equations were first derived in 1969.[249] Eqs. 4.15 and 4.16 reflect what Giddings described so eloquently in his *magnum opus*: "Separation is the art and science of maximizing separative transport relative to dispersive transport".[36] While the directional electrophoretic motion of ions is responsible for separative transport (proportional to K), random thermal motion causing diffusion leads to dispersive mass transport (proportional to D). The more dominant the former relative to the latter, the sharper the peaks appear.

We may interpret Eq. 4.15 as the ratio of two energies: the electrical potential energy drop experienced by an ion, qV_{D}, and the thermal energy, $k_{\mathrm{B}}T$.[257,271] Thus, performing separations at low temperatures and applying higher V_{D} may significantly increase N_{diff}. Importantly, N_{diff} is influenced by the ratio of K and D, and not by the absolute values of these transport

properties. Because the ratio depends solely on the temperature and the charge state of the ion in question, the CCS does not affect N_{diff}. Being proportional to $\sqrt{N_{\mathrm{diff}}}$, the same considerations apply also to $R_{\mathrm{P,diff}}$. Although higher buffer gas pressure p and longer drift cells enable the application of higher V_{D} in low-field DTIMS by helping to keep the reduced field strength sufficiently low, p and L_{D} do not influence N_{diff} or $R_{\mathrm{P,diff}}$ directly. The benefits of higher p and longer tubes stem mainly from their influence on the spatial variance of the injected ion packet, as discussed in the following paragraph.

Injection pulse-width. Intrinsic dispersion processes such as diffusion are the cause of the ion clouds' inevitable expansion during their passage through the drift cell. The ion clouds, however, are not infinitesimally narrow at the moment they enter the separation region. They have finite initial width contributing substantially to the total width of zones and thus, the injection pulse-width must be considered as an important extrinsic source of variance.

In our simple picture of DTIM separations, the axial distribution of ions in the injected packet is assumed to follow exactly the shape of the injection voltage pulse. The relation between the duration of this pulse, t_{inj}, and the temporal standard deviation of the injected ion packet, $\sigma_{\mathrm{t,inj}}$, depends on the aforementioned distribution and thus, on the shape of the pulse:

$$\sigma_{\mathrm{t,inj}}^2 = \frac{t_{\mathrm{inj}}^2}{C_{\mathrm{inj}}}. \tag{4.17}$$

The dimensionless constant of proportionality, C_{inj}, may be readily obtained through calculating the second central moment of the respective probability density function (see Appendix A). In case of a rectangular distribution C_{inj} adopts a value of 12, while assuming Gaussian distribution $C_{\mathrm{inj}} = 16$. For quadratic and symmetric triangular distributions C_{inj} becomes 20 and 24, respectively. Injection voltage pulses are applied generally as boxcar functions, resulting in rectangular ion distributions and $C_{\mathrm{inj}} = 12$.

The spatial variance of an injected ion cloud can be calculated by multiplying $\sigma_{\mathrm{t,inj}}^2$ with the square of the drift velocity:

$$\begin{aligned}\sigma_{\mathrm{L,inj}}^2 &= \sigma_{\mathrm{t,inj}}^2 v_{\mathrm{D}}^2 \\ &= \frac{t_{\mathrm{inj}}^2}{C_{\mathrm{inj}}} \left(\frac{K V_{\mathrm{D}}}{L_{\mathrm{D}}} \right)^2 .\end{aligned} \tag{4.18}$$

Thus, while $\sigma_{\mathrm{t,inj}}^2$ is essentially the same for all analytes within a single experiment, $\sigma_{\mathrm{L,inj}}^2$ may differ significantly for the various species of a multicomponent sample, depending on the species' K. From Eq. 4.18 the injection limit of

theoretical plates and the injection limited resolving power can be readily derived:

$$N_{\mathrm{inj}} = C_{\mathrm{inj}} \frac{t_{\mathrm{D}}^2}{t_{\mathrm{inj}}^2} = \frac{C_{\mathrm{inj}}}{t_{\mathrm{inj}}^2} \left(\frac{L_{\mathrm{D}}^2}{K V_{\mathrm{D}}} \right)^2, \tag{4.19}$$

$$R_{\mathrm{P,inj}} = \sqrt{\frac{C_{\mathrm{inj}}}{8 \ln 2}} \frac{t_{\mathrm{D}}}{t_{\mathrm{inj}}} = \sqrt{\frac{C_{\mathrm{inj}}}{8 \ln 2}} \frac{L_{\mathrm{D}}^2}{t_{\mathrm{inj}} K V_{\mathrm{D}}}. \tag{4.20}$$

N_{inj} is inversely proportional to t_{inj}^2, and being defined by the $t_{\mathrm{D}}^2/\sigma_{\mathrm{t,inj}}^2$ ratio, it is affected by every factor that influences a given analyte's t_{D}. Upon revealing these influences, strong dependence on L_{D} and inverse proportionality to V_{D}^2 become apparent. These characteristics are in strong contrast with those found for N_{diff} (see Eq. 4.15 on page 50 for comparison). In relation to N_{inj} it is important to discuss the role of transport properties. Unlike its diffusion limited counterpart that depends on the K/D ratio, N_{inj} is inversely proportional to K^2 and entirely independent of D. Thus, it depends on all such characteristics of the ions and the separation medium that influence K. For ions with lower $|q|$ and for ion–neutral pairs with larger CCS, N_{inj} appears to be higher, while performing experiments at higher buffer gas number densities n increases N_{inj} for all analytes in a sample uniformly. Being proportional to $\sqrt{N_{\mathrm{inj}}}$, similar considerations apply to $R_{\mathrm{P,inj}}$.

Longitudinal diffusion and the finite width of the injected ion cloud are the most important sources of zone broadening in DTIM separations.[28,269,272,273] Together they form the backbone of analytical models aimed at predicting the total variance of zones by considering experimental conditions and characteristics of the analytes. To further refine the model presented herein, a few additional sources of dispersion shall be considered.

Coulomb repulsion. Such additional dispersion may result from space charge effects.[274,275] Although the electrophoretic motion of ions is governed principally by the drift field E_{D}, charged analytes can also interact with the electric field of the ion clouds' space charge. This repulsive Coulombic interaction may lead to further expansion of the clouds and thus increase the total variance.

At low ion number densities the motion of individual ions may be assumed to be independent of one other.[173] When the space charge field becomes significant, however, the ions' velocity vectors will be influenced by the surrounding charged species. Unfortunately, differential equations describing the evolution of ion clouds due to simultaneous diffusion and electrophoretic motion in a space charge field are nonlinear, and their solution requires numerical methods.[276] Instead of relying on numerical calculations, we follow a simpler approach that yields an analytical solution compatible with plate-height models. Adapted from Tolmachev *et al.*[277], the approach is based on Gauss's law for electrostatics and the assumption that diffusion and Coulomb repulsion act independently. Similar physical models were developed by Xu *et al.*[278] and Kirk *et al.*[270], considering ion clouds with different initial geometries. Due to the assumptions and the fact that the ion clouds' total charge may not be known accurately, the following equations merely estimate rather than precisely quantify the impact of Coulomb repulsion on zone broadening in DTIM separations.

Let us consider a spherically shaped ion cloud with radius r and total electric charge Q, consisting of ions with identical K values. Neglecting diffusional effects, expansion of the cloud during its drift results exclusively from Coulomb repulsion. The Coulombic or space charge field at the edge of the cloud, E_{Clmb}, drives the expansion through propelling ions at the cloud's boundary. According to Gauss's law for electrostatics, E_{Clmb} appears as

$$E_{\mathrm{Clmb}} = \frac{Q}{4\pi r^2 \varepsilon}, \tag{4.21}$$

where ε is the absolute permittivity of the buffer gas, virtually equal to the vacuum permittivity, $\varepsilon_0 = 8.854\,187\,8128 \cdot 10^{-12}$ Fm^{-1}. Thus, E_{Clmb} is determined only by Q and the surface area of the spherical ion packet. As long as spherical symmetry is maintained, E_{Clmb} is independent of the ions' radial distribution within the cloud. The rate of the ion cloud's Coulomb expansion is given as the product of E_{Clmb} and the mobility of ions:

$$\begin{aligned} v_{\mathrm{Clmb}} &= \frac{\mathrm{d}r}{\mathrm{d}t} \\ &= K E_{\mathrm{Clmb}}. \end{aligned} \tag{4.22}$$

Combining Eqs. 4.21 and 4.22 we arrive at the following first-order differential equation:

$$\frac{\mathrm{d}r}{\mathrm{d}t} = K \frac{Q}{4\pi r^2 \varepsilon_0}. \tag{4.23}$$

Solving of Eq. 4.23 and substituting t_D for time we obtain

$$r(t_{\mathrm{D}}) = \left(\frac{3KQ}{4\pi\varepsilon_0}(t_{\mathrm{D}} + t_0)\right)^{1/3}, \tag{4.24}$$

where t_0 is the constant of integration. It can be readily calculated from r_0, the initial radius of the ion cloud:

$$t_0 = r_0^3 \frac{4\pi\varepsilon_0}{3KQ}. \tag{4.25}$$

When r_0 is neglected, the increase in the radius of an ion cloud due to Coulomb repulsion, r_{Clmb}, can be expressed in the following form:

$$r_{\mathrm{Clmb}} = \left(\frac{3KQ}{4\pi\varepsilon_0} t_{\mathrm{D}}\right)^{1/3}. \tag{4.26}$$

Although it does not influence r_{Clmb}, the radial distribution of ions inside the ion cloud in the model needs to be considered when deriving the corresponding spatial variance from Eq. 4.26. Upon introducing the dimensionless constant C_{Clmb} and expressing t_{D} with more fundamental quantities, we obtain the following expression for $\sigma^2_{\mathrm{L,Clmb}}$:

$$\begin{aligned} \sigma^2_{\mathrm{L,Clmb}} &= \frac{r^2_{\mathrm{Clmb}}}{C_{\mathrm{Clmb}}} \\ &= \frac{1}{C_{\mathrm{Clmb}}} \left(\frac{3Q}{4\pi\varepsilon_0 V_{\mathrm{D}}} L^2_{\mathrm{D}}\right)^{2/3}. \end{aligned} \tag{4.27}$$

The role of C_{Clmb} above is analogous to that of C_{inj} in Eqs. 4.17 and 4.18, and its value can be calculated in a similar fashion. Uniformly populated spherical ion clouds gives rise to quadratic radial ion distributions, and thus $C_{\mathrm{Clmb}} = 5$. For Gaussian distributions $C_{\mathrm{Clmb}} = 4$, while for rectangular distributions the constant of proportionality adopts a value of 3. To calculate C_{Clmb}, note that r_{Clmb} is half of the respective distribution's full-width at the base. From Eq. 4.27 the Coulomb limit of theoretical plates and the corresponding resolving power limit can be finally derived:

$$\begin{aligned} N_{\mathrm{Clmb}} &= C_{\mathrm{Clmb}} \frac{L^2_{\mathrm{D}}}{r^2_{\mathrm{Clmb}}} \\ &= C_{\mathrm{Clmb}} \left(\frac{4\pi\varepsilon_0 V_{\mathrm{D}}}{3Q} L_{\mathrm{D}}\right)^{2/3}, \end{aligned} \tag{4.28}$$

$$R_{\mathrm{P,Clmb}} = \sqrt{\frac{C_{\mathrm{Clmb}}}{8\ln 2}}\frac{L_{\mathrm{D}}}{r_{\mathrm{Clmb}}} = \sqrt{\frac{C_{\mathrm{Clmb}}}{8\ln 2}}\left(\frac{4\pi\varepsilon_0 V_{\mathrm{D}}}{3Q}L_{\mathrm{D}}\right)^{1/3}. \tag{4.29}$$

The detrimental effect of large Q values is apparent. Since v_{D} and v_{Clmb} are both directly proportional to K, the influence of the mobility cancels out, leaving N_{Clmb} and $R_{\mathrm{P,Clmb}}$ independent of this transport property. The equations above also reveal the explicit dependence of N_{Clmb} and $R_{\mathrm{P,Clmb}}$ on L_{D}, a characteristic that is in contrast with that of their diffusion limited counterparts (see Eqs. 4.15 and 4.16 on page 50). Finally, an interesting remark in relation to the rate of generating spatial variance: while $\mathrm{d}\sigma^2_{\mathrm{L,diff}}/\mathrm{d}L_{\mathrm{D}}$ is invariable along the drift cell, $\mathrm{d}\sigma^2_{\mathrm{L,Clmb}}/\mathrm{d}L_{\mathrm{D}}$ decreases continuously towards its exit. Because the latter varies systematically from point to point in a drift tube, the separation field may be considered nonuniform.[266,267] When compared, however, Coulomb expansion giving rise to this intrinsic variation in the local plate height is generally much less significant than diffusional broadening.

Electric field inhomogeneities. Any deviation from an ideal, perfectly homogeneous drift field leads to the increase of measured t_{D} values in DTIMS.[279] In imperfect, spatially heterogeneous fields the ions behave as if the applied V_{D} were decreased by a factor of $\theta \geq 1$, resulting in lower average v_{D} values:

$$v_{\mathrm{D}} = \frac{KV_{\mathrm{D}}}{L_{\mathrm{D}}\theta}. \tag{4.30}$$

This phenomenon manifests in systematic errors of experimentally determined mobilities, and negatively affects the plate count and resolving power of DTIM separations.[270,280]

To account for field inhomogeneities, let us substitute V_{D}/θ for V_{D} in Eqs. 4.14 and 4.27:

$$\sigma^2_{\mathrm{L,diff}} = L^2_{\mathrm{D}}\frac{2k_{\mathrm{B}}T}{qV_{\mathrm{D}}}\theta, \tag{4.31}$$

$$\sigma^2_{\mathrm{L,Clmb}} = \frac{1}{C_{\mathrm{Clmb}}}\left(\frac{3Q}{4\pi\varepsilon_0 V_{\mathrm{D}}}L^2_{\mathrm{D}}\theta\right)^{2/3}.$$

Thus, in presence of field inhomogeneities, $\sigma^2_{\mathrm{L,diff}}$ and $\sigma^2_{\mathrm{L,Clmb}}$ increase by a factor of θ and $\theta^{2/3}$, respectively. The corresponding theoretical plate limits,

N_{diff} and N_{Clmb}, decrease in proportion. Determining θ experimentally for a given drift cell requires reference standards with known accurate K_0 or CCS values, and all other sources of systematic error must be excluded or minimized. Although satisfying these criteria is extremely challenging, especially since no K_0 and CCS standards are available that represent such high precision and trueness as those for mass or frequency, comparing reference K_0 or CCS values with measured ones at the same effective temperature could in principle provide an estimate of the field correction factor:

$$\begin{aligned}\theta &= \frac{1}{j}\sum_{i=1}^{j}\frac{K_{0,\mathrm{ref,i}}}{K_{0,\mathrm{exp,i}}} \\ &= \frac{1}{j}\sum_{i=1}^{j}\frac{\mathrm{CCS}_{\mathrm{exp,i}}}{\mathrm{CCS}_{\mathrm{ref,i}}}.\end{aligned} \tag{4.32}$$

Correction with a single θ value applies to hypothetical situations where every ion experiences the same inhomogeneous field. In reality, each ions has a different trajectory, and ions closer to the tube axis drift in a more homogeneous field than those father away. The resulting distribution of θ values leads to differences in t_{D} and thus to additional zone broadening.[270,279] To obtain the distribution of θ values, accurate mapping of the drift field and simulation of ion trajectories would be required, which is out of the scope of the plate-height model.

Dispersion in the exit funnel. In stand-alone DTIMS, ions impinge on a Faraday cup, microchannel plate, or other suitable detector placed directly at the end of the drift tube. In DTIM-MS, on the other hand, ions exiting the drift cell need to traverse various compartments, such as ion funnels, ion guides, and mass analyzers, before being finally detected. During this transit the temporal variance of the analyte zones increases, and thus post-cell dispersion may significantly influence the efficiency of the DTIM separation. We make no attempt here to estimate the extent of zone spreading in the high vacuum region of DTIM-MS devices. Instead, a simple model is presented to account for drift and dispersion in exit funnels placed after DC-only drift tubes. The model exploits the fact that ions in such funnels are propelled axially by a constant electric field, while the impact of radial confinement on the ion distribution is neglected. Thus, the model treats exit funnels simply as extensions of drift cells.

Being no conductance limit between the two compartments, p and T in the exit funnel are the same as inside the drift tube. Consequently, transport

properties remain unaltered. Similarly to drift cells, ion clouds inside the funnel expand due to diffusion and Coulomb repulsion, and the respective spatial variances can be expressed analogously:

$$\sigma^2_{\mathrm{L,fun,diff}} = L^2_{\mathrm{fun}} \frac{2k_{\mathrm{B}}T}{qV_{\mathrm{fun}}}, \tag{4.33}$$

$$\sigma^2_{\mathrm{L,fun,Clmb}} = \frac{1}{C_{\mathrm{Clmb}}} \left(\frac{3Q}{4\pi\varepsilon_0 V_{\mathrm{fun}}} L^2_{\mathrm{fun}} \right)^{2/3}. \tag{4.34}$$

Here, L_{fun} is the funnel's length, while V_{fun} is the voltage drop across the funnel. Let us designate the sum of the two above variances as $\sigma^2_{\mathrm{L,fun}}$, while the sum of those associated with injection and the drift cell as $\sigma^2_{\mathrm{L,cell}}$. If the linear velocity of ions is identical in the funnel and the drift cell, the total spatial variance is given as the sum of $\sigma^2_{\mathrm{L,cell}}$ and $\sigma^2_{\mathrm{L,fun}}$, while the total length of the separation region is the sum of L_{D} and L_{fun}. Under such conditions the plate number in DTIM-MS can be calculated as

$$N_{\text{DTIM-MS}} = \frac{\left(L_{\mathrm{D}} + L_{\mathrm{fun}}\right)^2}{\sigma^2_{\mathrm{L,cell}} + \sigma^2_{\mathrm{L,fun}}}. \tag{4.35}$$

The case above is fairly simple. In practice, however, linear velocities between cell and funnel often differ, because the respective DC fields, E_{D} and E_{fun}, are not identical. To provide solution to such realistic situations, the summands need to be corrected with the velocity ratio.

When a zone's transit from one compartment to another is accompanied by a change in its linear velocity, the zone undergoes spatial contraction or expansion accordingly, while the temporal standard deviation remains unaffected:

$$\frac{\sigma_{\mathrm{L},1}}{v_1} = \frac{\sigma_{\mathrm{L},2}}{v_2}. \tag{4.36}$$

Here, $\sigma_{\mathrm{L},1}$ and $\sigma_{\mathrm{L},2}$ are the spatial standard deviations, while v_1 and v_2 are the linear velocities of the zone in the first and second compartment, respectively. Correcting Eq. 4.35 according to Eq. 4.36 results in the following equation:

$$N_{\text{DTIM-MS}} = \frac{\left(L_{\mathrm{D}} + L_{\mathrm{fun}} \frac{v_{\mathrm{D}}}{v_{\mathrm{fun}}}\right)^2}{\sigma^2_{\mathrm{L,cell}} + \sigma^2_{\mathrm{L,fun}} \frac{v^2_{\mathrm{D}}}{v^2_{\mathrm{fun}}}}, \tag{4.37}$$

where v_{fun} designates the linear velocity of ions in the funnel. In Eq. 4.37 the ratio of velocities could be readily replaced by that of the electric fields. We may term the second summand in the numerator the velocity corrected funnel

length, and the second summand in the denominator the velocity corrected spatial variance associated with the funnel. When v_D and v_fun differ, Eq. 4.37 describes a case of nonuniform separation fields where the rate of diffusional broadening $\mathrm{d}\sigma^2_\mathrm{L,diff}/\mathrm{d}L$ is different in the cell and the funnel. It is similar to the situation when chromatographic columns with different diameter or packing density are coupled in series, which leads to differences in the mobile phase linear velocity and thus changes in $\mathrm{d}\sigma^2_\mathrm{L,diff}/\mathrm{d}L$ between the individual columns.[267] Although the underlying physical processes are different, the mathematical concepts applied to calculate the total plate number in the two systems are similar.

Extending the logic behind Eq. 4.37 to any finite number of compartments (including the possibility of multiple drift tubes), and introducing the notation $M_\mathrm{i} = v_\mathrm{D}/v_\mathrm{i}$, i referring to the ith separate section, $N_\mathrm{DTIM\text{-}MS}$ can be expressed in the following general form:

$$\begin{aligned} N_\mathrm{DTIM\text{-}MS} &= \frac{\left(\sum_{i=1}^{j} L_\mathrm{i} M_\mathrm{i}\right)^2}{\sum_{i=1}^{j}\left(\sigma^2_\mathrm{L,i} M_\mathrm{i}^2\right)}(1-F)^2 \\ &= \frac{\left(\sum_{i=1}^{j} t_\mathrm{i}\right)^2}{\sum_{i=1}^{j}\sigma^2_\mathrm{t,i}}(1-F)^2. \end{aligned} \tag{4.38}$$

F is a dimensionless constant, defined as

$$\begin{aligned} F &= \frac{t_\mathrm{ns}}{t_\mathrm{A}} \\ &= \frac{t_\mathrm{ns}}{t_\mathrm{s}+t_\mathrm{ns}}, \end{aligned} \tag{4.39}$$

where t_s is the separative transport time (the sum of the net t_D and the time spent in the exit funnel), t_ns is the residence time in compartments where no mobility separation occurs (ion guides, mass analyzers, *etc.*), and t_A is their sum, the total arrival time. Upon correction with F, the nonseparative residence time t_ns will not add superfluously to the numerator when calculating $N_\mathrm{DTIM\text{-}MS}$. In cases when only drift cells and exit funnels are considered, as in Eqs. 4.35 and 4.37, t_ns and F are both 0.

The above model was developed for instruments that employ DC-only drift tubes in combination with exit funnels to focus ions radially before their passage through conductance limits. Many commercial and custom-built DTIM-MS devices follow this design.[281–287] An alternative strategy utilizes RF-confining drift cells to keep ion packets radially focused during

their entire drift, which renders exit funnels unnecessary.[229,288,289] Even if exit funnels are absent in such DTIM-MS setups, dispersion in their other post-cell compartments can in principle be taken into account by applying the general mathematical framework of Eq. 4.38.

Having addressed various dispersion processes individually, we may now synthesize these findings and apply them to formulate adequate plate-height equations for DTIMS and DTIM-MS. The following section is dedicated entirely to this subject.

4.2.3 Plate-height equations

To estimate the total width of zones and that of the resulting peaks, plate-height models rely on the summation of variances. At the end of Section 4.2.2 we already applied this concept to obtain suitable expressions for $N_{\text{DTIM-MS}}$. Herein we use the same strategy to derive two plate-height equations in analogy to those existing for chromatography: a simplified formula for stand-alone DTIMS, and an extended expression for DTIM-MS.

Plate-height equation for DTIMS. Under isocratic conditions, the velocity of chromatograpic bands is directly proportional to the flow rate of the carrier fluid. As linear velocities play a pivotal role in determining the efficiency of chromatographic separations through influencing multiple dispersion processes, HETP is generally represented there as a function of mobile phase velocity. In comparison, drift velocities in DTIMS are directly proportional to E_{D} or V_{D}, which affect the various dispersion phenomena in often antagonistic ways. Therefore, when constructing plate-height equations for DTIM separations, we may represent HETP as a function of either of the above-mentioned variables. Since V_{D} is an experimental parameter controlled directly in practice, we chose it over E_{D} for convenience. Employing E_{D} as the independent variable would result in analogous plate-height functions with similar appearance and equivalent utility.

Having discussed the role of V_{D}, let us start the derivation by introducing the following notations for brevity:

$$\mathbf{B} = \frac{t_{\text{inj}}^2 K^2}{C_{\text{inj}} L_{\text{D}}^2}, \tag{4.40}$$

$$\mathbf{D} = L_{\text{D}}^2 \frac{2k_{\text{B}}T}{q}\theta, \tag{4.41}$$

where $\mathbf{B}$ and $\mathbf{D}$ are inferred from $\sigma_{\text{L,inj}}^2$ and $\sigma_{\text{L,diff}}^2$, respectively. Employing the above integrated terms and neglecting Coulomb repulsion, a concise

plate-height equation can be formulated for stand-alone DTIMS:

$$\begin{aligned} \mathrm{HETP}_{\mathrm{DTIMS}} &= \frac{\sigma^2_{\mathrm{L,inj}} + \sigma^2_{\mathrm{L,diff}}}{L_{\mathrm{D}}} \\ &= \frac{\mathbf{B}V_{\mathrm{D}}^2 + \mathbf{D}/V_{\mathrm{D}}}{L_{\mathrm{D}}}. \end{aligned} \tag{4.42}$$

Eq. 4.42 highlights the role of V_{D}, and its minimum corresponds to the case where the sharpest zones and highest resolving power are achieved for the representative analyte chosen. Thus, finding this minimum is of practical importance. For this purpose, let us consider the following derivative:

$$\frac{\mathrm{d}(\mathrm{HETP}_{\mathrm{DTIMS}})}{\mathrm{d}V_{\mathrm{D}}} = \frac{2\mathbf{B}V_{\mathrm{D}} - \mathbf{D}/V_{\mathrm{D}}^2}{L_{\mathrm{D}}}. \tag{4.43}$$

Equating the above function to 0, a simple expression can be derived for the optimum of V_{D}, *i.e.* for the position of the minimum along the abscissa:

$$V_{\mathrm{D,opt}} = \left(\frac{\mathbf{D}}{2\mathbf{B}}\right)^{1/3}. \tag{4.44}$$

Substituting the above expression into Eq. 4.42, a comparably simple formula arises for $\mathrm{HETP}_{\mathrm{DTIMS,min}}$, the position of the minimum along the ordinate:

$$\mathrm{HETP}_{\mathrm{DTIMS,min}} = \frac{3}{L_{\mathrm{D}}}\left(\frac{\mathbf{D}^2\mathbf{B}}{4}\right)^{1/3}. \tag{4.45}$$

A graphical representation of Eq. 4.42 is shown in Figure 4.1, highlighting the function's minimum and the independent dispersion contributions from diffusion and the injection pulse. The calculation corresponds to a hypothetical stand-alone DTIMS experiment in a drift tube identical to that of the iMob instrument, with no contribution from post-cell compartments. The input parameters mimic experimental conditions generally applied for real-life experiments with the iMob.

Similarly to Eq. 4.42, the plate count in DTIMS may be expressed using the terms $\mathbf{B}$ and $\mathbf{D}$, thereby highlighting the role of V_{D}:

$$\begin{aligned} N_{\mathrm{DTIMS}} &= \frac{L_{\mathrm{D}}^2}{\sigma^2_{\mathrm{L,inj}} + \sigma^2_{\mathrm{L,diff}}} \\ &= \frac{L_{\mathrm{D}}^2}{\mathbf{B}V_{\mathrm{D}}^2 + \mathbf{D}/V_{\mathrm{D}}}. \end{aligned} \tag{4.46}$$

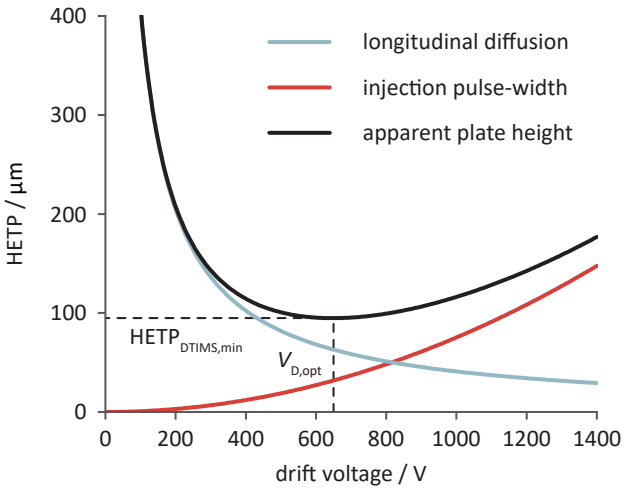

Figure 4.1: Graphical representation of the plate-height equation for stand-alone DTIMS. Computation was performed according to Eq. 4.42 with the following input parameters: He buffer gas, $p = 3\,\mathrm{mbar}$, $T = 295\,\mathrm{K}$, $L_\mathrm{D} = 805.5\,\mathrm{mm}$, $t_\mathrm{inj} = 150\,\mu\mathrm{s}$. K was derived according to the Mason–Schamp equation for analyte **#2**: ${}^{\mathrm{DT}}\mathrm{CCS}_\mathrm{He} = 139\,\mathrm{Å}^2$, $m = 527\,\mathrm{Da}$, $z = +1$ (see Section 3.1). Rectangular injection profile ($C_\mathrm{inj} = 12$) and a completely homogeneous drift field ($\theta = 1$) were assumed.

By combining Eq. 4.45 with the general relation $N = L/\mathrm{HETP}$, the maximally achievable plate count can be calculated:

$$N_\mathrm{DTIMS,max} = \frac{L_\mathrm{D}^2}{3}\left(\frac{4}{\mathbf{D}^2\mathbf{B}}\right)^{1/3}. \tag{4.47}$$

Finally, the respective expressions for $R_\mathrm{P,DTIMS}$ and its maximum can be formulated analogously:

$$\begin{aligned} R_\mathrm{P,DTIMS} &= \sqrt{\frac{N_\mathrm{DTIMS}}{8\ln 2}} \\ &= \frac{L_\mathrm{D}}{\sqrt{8\ln 2\,(\mathbf{B}V_\mathrm{D}^2 + \mathbf{D}/V_\mathrm{D})}}, \end{aligned} \tag{4.48}$$

$$R_\mathrm{P,DTIMS,max} = \frac{L_\mathrm{D}}{\sqrt{24\ln 2}}\left(\frac{2}{\mathbf{D}\sqrt{\mathbf{B}}}\right)^{1/3}. \tag{4.49}$$

The plate-height equation and related expressions presented above offer a simple and transparent approach to predict separation efficiency in stand-alone DTIMS. Similarly to their analogues in chromatography, these equations reveal key factors influencing zone broadening, thereby aiding analytical method development and creating a sound theoretical basis for optimization strategies.

Extended plate-height equation for DTIM-MS. In addition to being employed as a stand-alone analytical tool, drift tubes are often coupled to mass analyzers through a suitable interface. While Eq. 4.42 is limited to

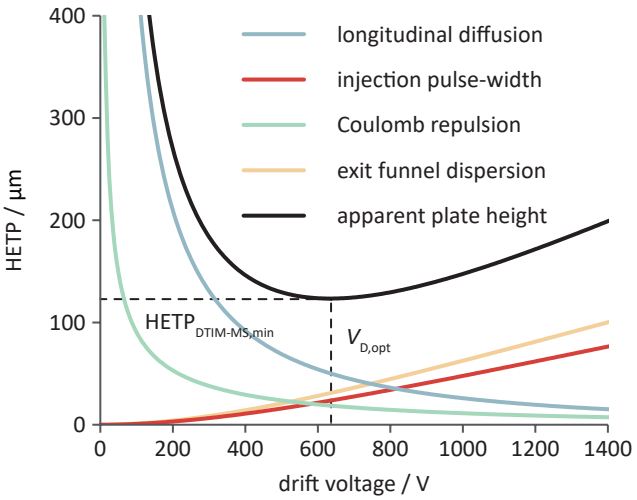

Figure 4.2: Graphical representation of the extended plate-height equation for DTIM-MS. Computation was performed according to Eq. 4.52 with the following input parameters: He buffer gas, $p = 3\,\mathrm{mbar}$, $T = 295\,\mathrm{K}$, $L_\mathrm{D} = 805.5\,\mathrm{mm}$, $L_\mathrm{fun} = 144\,\mathrm{mm}$, $v_\mathrm{fun} = 88.5\,\mathrm{m\,s^{-1}}$, $t_\mathrm{inj} = 150\,\mu\mathrm{s}$. K was derived according to the Mason–Schamp equation for analyte **#2**: ${}^\mathrm{DT}\mathrm{CCS}_\mathrm{He} = 139\,\mathrm{Å}^2$, $m = 527\,\mathrm{Da}$, $z = +1$. We assumed $Q = 100\,000\,e$, $C_\mathrm{Clmb} = 3$, $C_\mathrm{inj} = 12$, and $\theta = 1$ for the calculations.

stand-alone DTIMS, employing the model developed in Section 4.2.2 it can be readily extended to describe separations in DTIM-MS devices equipped with exit funnels. This extended plate-height equation can be further refined by including an estimate of space charge effects, without having to sacrifice the simplicity of analytical models.

We may start by introducing two additional integrated terms, corresponding to funnel-associated dispersion and Coulomb repulsion in the drift cell, respectively:

$$\mathbf{A} = \left[L_\mathrm{fun}^2 \frac{2k_\mathrm{B}T}{qV_\mathrm{fun}} + \frac{1}{C_\mathrm{Clmb}} \left(\frac{3Q}{4\pi\varepsilon_0 V_\mathrm{fun}} L_\mathrm{fun}^2 \right)^{2/3} \right] \left[\frac{L_\mathrm{fun}}{L_\mathrm{D} V_\mathrm{fun}} \right]^2, \tag{4.50}$$

$$\mathbf{C} = \frac{1}{C_\mathrm{Clmb}} \left(\frac{3Q}{4\pi\varepsilon_0} L_\mathrm{D}^2 \theta \right)^{2/3}. \tag{4.51}$$

In term **A**, the multiplicand in brackets on the left is essentially $\sigma_\mathrm{L,fun}^2$, while the multiplier in brackets on the right serves, together with V_D, for velocity correction. By combining all four integrated terms and accounting for potential velocity mismatch between cell and funnel, the following plate-height equation can be obtained for DTIM-MS:

$$\begin{aligned} \mathrm{HETP}_\mathrm{DTIM\text{-}MS} &= \frac{\sigma_\mathrm{L,inj}^2 + \sigma_\mathrm{L,diff}^2 + \sigma_\mathrm{L,Clmb}^2 + \sigma_\mathrm{L,fun}^2 M_\mathrm{fun}^2}{\left(L_\mathrm{D} + L_\mathrm{fun} M_\mathrm{fun}\right)^2} (L_\mathrm{D} + L_\mathrm{fun}) \\ &= \frac{(\mathbf{A} + \mathbf{B}) V_\mathrm{D}^2 + \mathbf{C}/V_\mathrm{D}^{2/3} + \mathbf{D}/V_\mathrm{D}}{\left(L_\mathrm{D} + L_\mathrm{fun} M_\mathrm{fun}\right)^2} (L_\mathrm{D} + L_\mathrm{fun}). \end{aligned} \tag{4.52}$$

M_{fun} denotes the velocity ratio $v_{\mathrm{D}}/v_{\mathrm{fun}}$ (see Eq. 4.38 on page 58). Although Eq. 4.52 looks rather extensive, it involves only addition, multiplication, division, and exponentiation, which makes the equation highly spreadsheet compatible. Figure 4.2 shows a graphical representation of Eq. 4.42, with the portrayed function corresponding to a real experiment performed with the iMob custom-built DTIM-MS instrument. Note that the relative contribution of the funnel-associated dispersion to $\mathrm{HETP}_{\text{DTIM-MS}}$ increases as V_{D} is being raised. While $\sigma^2_{\mathrm{L,fun}}$ itself is of course entirely independent of V_{D}, it is weighted with M^2_{fun} in Eq. 4.52. Thus, increasing V_{D} while keeping conditions in the funnel constant will lead to the increase of the respective velocity corrected spatial variance.

For completeness, let us express $N_{\text{DTIM-MS}}$ and $R_{\text{P,DTIM-MS}}$ in similar form:

$$\begin{aligned} N_{\text{DTIM-MS}} &= \frac{(L_{\mathrm{D}} + L_{\mathrm{fun}} M_{\mathrm{fun}})^2}{\sigma^2_{\mathrm{L,inj}} + \sigma^2_{\mathrm{L,diff}} + \sigma^2_{\mathrm{L,Clmb}} + \sigma^2_{\mathrm{L,fun}} M^2_{\mathrm{fun}}} \\ &= \frac{(L_{\mathrm{D}} + L_{\mathrm{fun}} M_{\mathrm{fun}})^2}{(\mathbf{A}+\mathbf{B}) V_{\mathrm{D}}^2 + \mathbf{C}/V_{\mathrm{D}}^{2/3} + \mathbf{D}/V_{\mathrm{D}}}, \end{aligned} \tag{4.53}$$

$$\begin{aligned} R_{\text{P,DTIM-MS}} &= \sqrt{\frac{N_{\text{DTIM-MS}}}{8 \ln 2}} \\ &= \frac{L_{\mathrm{D}} + L_{\mathrm{fun}} M_{\mathrm{fun}}}{\sqrt{8 \ln 2 \left[(\mathbf{A}+\mathbf{B}) V_{\mathrm{D}}^2 + \mathbf{C}/V_{\mathrm{D}}^{2/3} + \mathbf{D}/V_{\mathrm{D}} \right]}}. \end{aligned} \tag{4.54}$$

Through predicting the extent of zone broadening and revealing the influence of experimental parameters on HETP, N, and R_{P}, equations presented herein may help to rationalize method development and the optimization of DTIM separations in everyday practice. To assess their practical utility, however, rigorous comparison to experimental data is necessary.

4.2.4 Comparison of theory and experiment

To evaluate the accuracy and predictive potential of the model, a series of experiments were performed using the iMob custom-built DTIM-MS instrument. All measurements were carried out in positive ion mode with He as buffer gas. We varied p, t_{inj}, and the ${}^{\mathrm{DT}}\mathrm{CCS}_{\mathrm{He}}$ of the singly charged analytes in a systematic manner, while all other parameters were left unchanged. Representative ATDs obtained for a singly charged trisaccharide (analyte **#2**) are shown in Figure 4.3. By measuring the centroid arrival time and width of such ATDs, the experimentally achieved N, R_{P}, and HETP could be readily determined. Sweeping V_{D} from low to high values and plotting the experimentally achieved HETP as the function of voltage resulted in the characteristic curves shown on the left-hand side of Figure 4.4. For comparison, the corresponding theoretical HETP functions, calculated based on Eq. 4.52, are displayed on the right-hand side of the figure. Since in the present as well as in the following section all experiments and calculations refer to DTIM-MS, for simplicity this abbreviation is dropped from the subscript of the respective figures of merit.

In general, the plate-height model shows good agreement with experimental data. Trends observed in the experiments upon changing p, t_{inj}, and the ${}^{\mathrm{DT}}\mathrm{CCS}_{\mathrm{He}}$ are successfully reproduced by theory. In addition, agreement is satisfactory in most cases even on a quantitative level. As expected, increasing p from 3 to 5 mbar or reducing t_{inj} from 150 to 50 µs have profound positive influence on HETP. While having no impact on the extent of diffusional broadening, increasing p reduces the spatial spread of the injected ion cloud. Thus, its effect is essentially equivalent to that of applying shorter injection pulses. Although p is not present explicitly in Eq. 4.52, its influence on

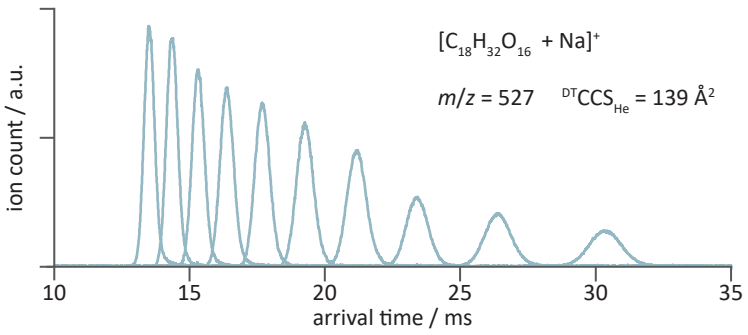

Figure 4.3: Representative arrival time distributions obtained for a singly sodiated trisaccharide (analyte **#2**) using the iMob DTIM-MS instrument. The measurements were performed in He buffer gas at $p = 3$ mbar and $T = 295$ K, with $t_{\mathrm{inj}} = 150$ µs. The depicted ATDs correspond to V_{D} values varied between 160 and 385 V in equidistant steps.

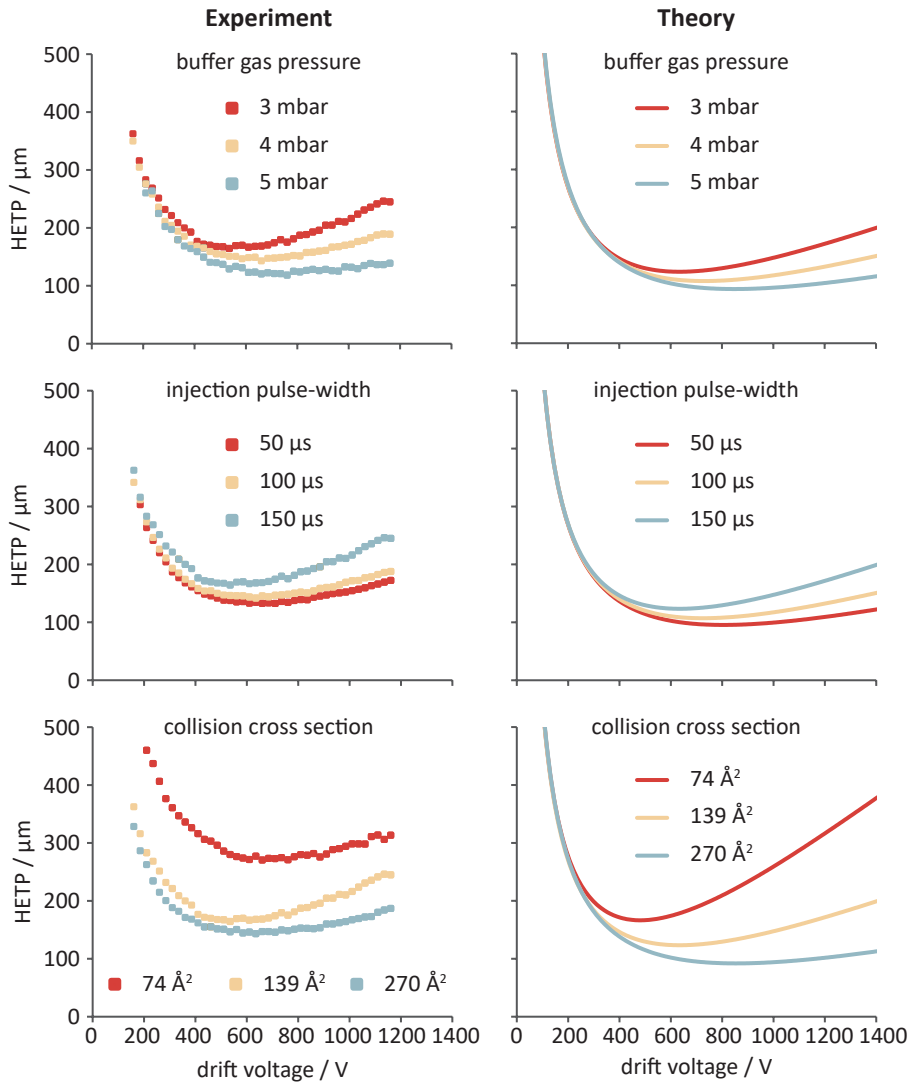

Figure 4.4: Plate height in DTIM-MS: comparison of experiment and theory. Experimental results are displayed on the left-hand side, while the right-hand side shows theoretically predicted HETP as a function of the drift voltage. To study their influence on HETP, three key parameters were changed systematically: (top) $p = 3\,\text{mbar}$, $4\,\text{mbar}$, $5\,\text{mbar}$; (center) $t_{\text{inj}} = 50\,\mu\text{s}$, $100\,\mu\text{s}$, $150\,\mu\text{s}$; (bottom) ${}^{\text{DT}}\text{CCS}_{\text{He}} = 74\,\text{Å}^2$ (analyte **#1**), $139\,\text{Å}^2$ (analyte **#2**), $270\,\text{Å}^2$ (analyte **#3**). Except for the analyte mass having a negligible impact on K, all other parameters were kept identical in the experiments: He buffer gas, $L_{\text{D}} = 805.5\,\text{mm}$, $L_{\text{fun}} = 144\,\text{mm}$, $T = 295\,\text{K}$, $z = +1$. For the calculations $Q = 100\,000\,e$, $C_{\text{Clmb}} = 3$, $C_{\text{inj}} = 12$, and $\theta = 1$ were assumed.

HETP through K is evident. Figure 4.4 also demonstrates that HETP might be remarkably different for different analytes under identical experimental

conditions. Considering ions within the same charge state, sharper zones can be achieved for those having larger CCS and thus lower K. Again, the effect can be attributed to the phenomenon that, upon injection, spatially more compact ion packets arise for ions with lower K.

Interestingly, the traces corresponding to different p, t_{inj}, and ${}^{\mathrm{DT}}\mathrm{CCS}_{\mathrm{He}}$ values coincide at low V_{D} in both theory and experiment. Under such conditions, well below $V_{\mathrm{D,opt}}$, diffusion is the dominant dispersion process while the contribution of the injection pulse-width is negligible. Because the extent of diffusional spreading is independent of p, t_{inj}, or the ${}^{\mathrm{DT}}\mathrm{CCS}_{\mathrm{He}}$, the depicted HETP values converge to essentially the same diffusion-controlled limit at low V_{D}. In this context, the anomalous behavior of analyte **#1** requires further discussion. In addition to the deviation from the diffusion limit, HETP and $V_{\mathrm{D,\,opt}}$ for analyte **#1** in the experiment are significantly higher than the respective values predicted by theory. We may attribute these unexpected experimental results to two factors. First, zone broadening due to dynamic chemical phenomena can lead to broader peaks than expected considering only physical dispersion processes, which also explains the stark deviation from the diffusion limit. Second, the exceptionally high K of this ion under the conditions employed may lead to an early depletion of the ion reserve upon injection. The entrance funnel storing ions prior to their injection may become already empty before the injection pulse ends. Consequently, the temporal length of the ion packet could be shorter than the pulse duration, which shifts $V_{\mathrm{D,opt}}$ to higher values.

While the behavior of analytes **#2** and **#2** is generally well-described by the plate-height model, agreement between theory and experiment is of course not perfect. Potential sources for the systematic underestimation of HETP by the model could be the finite detector response time, additional post-cell dispersion (dispersion in the high vacuum region of the instrument was not considered), or the inadequate description of space charge and field inhomogeneity effects. The simplicity, transparency, and general applicability of the model, however, may compensate for many of its limitations. Finally, Figure 4.5 is presented as the equivalent of Figure 4.4, portraying R_{P} instead of HETP. While HETP is traditionally favored in chromatography, R_{P} is more widely used to evaluate DTIM separations. As the present work intends to reach both scientific communities, we show HETP as well as R_{P} values for completeness.

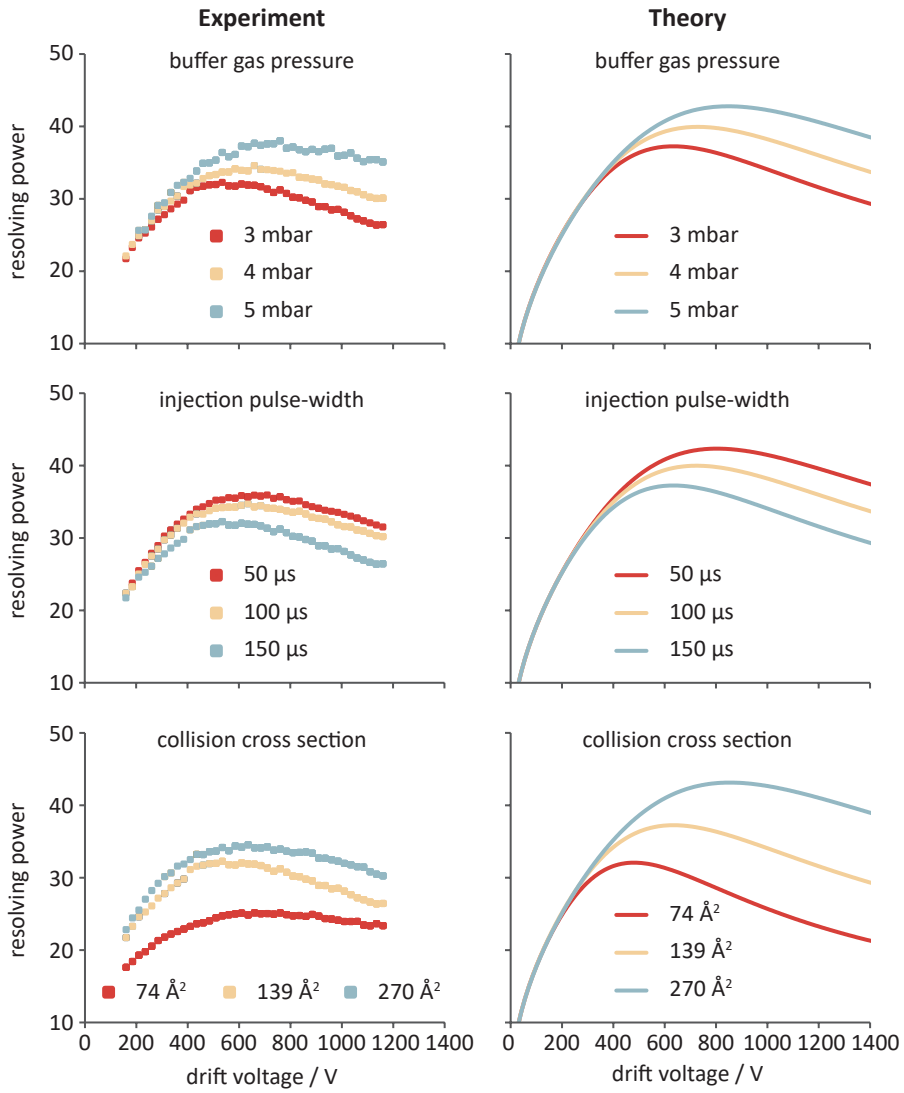

Figure 4.5: Resolving power in DTIM-MS: comparison of experiment and theory. An alternative representation of the data displayed in Figure 4.5, portraying resolving power instead of plate height.

4.2.5 Exploring the model

Having tested its capability to accurately predict zone broadening in DTIM-MS, herein we explore the model in more detail through extensive calculations. The impact of key experimental parameters and analyte features on HETP and R_P are highlighted in four examples. For this purpose, the drift and dispersion of hypothetical analytes is modeled according to Eqs. 4.52 and 4.54 under a range of realistic conditions, considering the dimensions of the iMob instrument.

Injection pulse-width. One of the most effective ways of achieving sharper zones in DTIM separations is to reduce the injection pulse-width. Figure 4.6 highlights the influence of this parameter on HETP and R_P, assuming that the initial ion distribution follows accurately the shape of the rectangular injection pulse. Creating compact ion packets upon injection is essential to come sufficiently close to the fundamental HETP and R_P limits determined by diffusion and Coulomb repulsion. The aforementioned limits, depicted in Figure 4.6 with black dashed lines, correspond to the hypothetical case where ions are introduced as a Dirac delta pulse ($t_{inj} = 0$), meaning that the integrated term $\mathbf{B} = 0$. Considering HETP (R_P), a representative part of the continuum above (below) the dashed line is sampled in ten equidistant steps between $t_{inj} = 25\,\mu s$ and $t_{inj} = 250\,\mu s$. Shortening t_{inj} reduces $\mathbf{B}$, while the other three terms in Eqs. 4.52 and 4.54 are left unaffected. As apparent from Figure 4.6, the narrower the injected ion packet, the higher the V_D value where the curves start to deviate noticeably from the dashed lines. Thus, with decreasing t_{inj}, $V_{D,opt}$ and $R_{P,max}$ shift to higher, while $HETP_{min}$ shifts to lower values, resulting in sharper peaks and more efficient separation.

Buffer gas pressure. Besides t_{inj}, the other most important experimental parameter an analyst may adjust to achieve sharper zones is the buffer gas pressure. As highlighted in Figure 4.7, applying higher p in the drift cell and the exit funnel is an effective way of reducing HETP and increasing R_P. Considering HETP (R_P), the minima (maxima) of the functions are shifted downwards (upwards) and to the right as p increases, which can be attributed to the decrease of $\mathbf{B}$ at elevated pressures. Although p does not appear explicitly in Eqs. 4.52 and 4.54, it has a strong influence on the $\mathbf{B}$-term through K, while the other three terms are unaffected.

Similarly to Figure 4.6, the black dashed lines in Figure 4.7 show the fundamental diffusion- and space charge-controlled limits of HETP and R_P. Importantly, the aforementioned limits do not depend on p: the limiting functions are the same at all values of p and are necessarily identical to

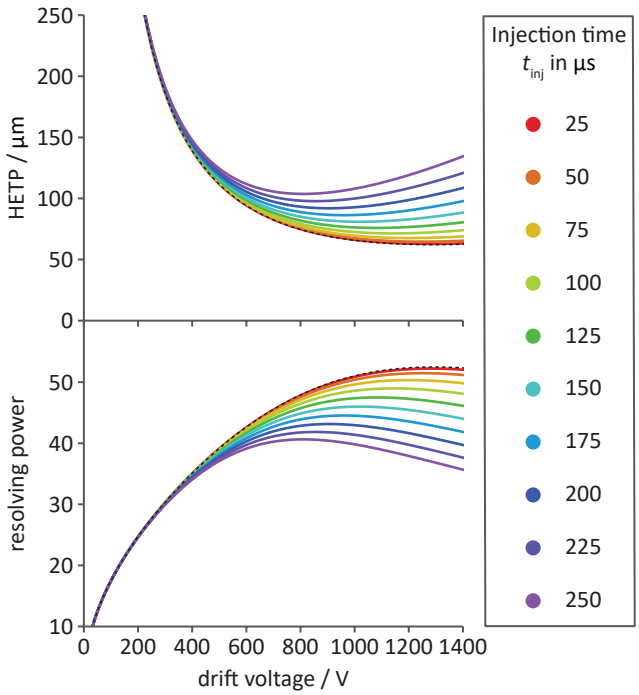

Figure 4.6: Influence of the injection pulse-width on the plate height and the resolving power in DTIM-MS. Different colors encode different t_{inj} values, ranging from 25 µs to 250 µs in ten equidistant steps as indicated. The black dashed lines correspond to an infinitesimally narrow injection pulse. Calculations were performed according to Eqs. 4.52 and 4.54 with the following input parameters: He buffer gas, $p = 4\,\mathrm{mbar}$, $T = 298.15\,\mathrm{K}$, $L_{\mathrm{D}} = 805.5\,\mathrm{mm}$, $L_{\mathrm{fun}} = 144\,\mathrm{mm}$. E_{fun} was kept constant at $10\,\mathrm{V\,cm^{-1}}$. K was derived according to the Mason–Schamp equation for the hypothetical analyte with $\mathrm{CCS_{He}} = 200\,\mathrm{Å}^2$, $m = 1000\,\mathrm{Da}$, and $|z| = 1$. $Q = 100\,000\,e$, $C_{\mathrm{Clmb}} = 3$, $C_{\mathrm{inj}} = 12$, and $\theta = 1$ were assumed in the calculations.

those in Figure 4.6. This is not surprising considering **A**, **C**, and **D** being independent of p. The curves corresponding to higher p values in Figure 4.7 start to deviate from the dashed lines at higher V_{D}. This phenomenon is completely analogous to that observed upon decreasing t_{inj}, as applying higher p or shorter t_{inj} both result in the same effect: lower **B**-terms and spatially more compact injected ion packets. Thus, R_{P} may not increase infinitely with increasing p at a given V_{D} value. R_{P} and HETP can only be improved until the limits set by the pressure-independent contributors are reached, *i.e.* where the spatial spread of the injected ion packet becomes negligible. It may be readily observed at low V_{D} where the various curves overlap. In this region, contribution of the injection pulse-width is still insignificant, leaving diffusion and space charge effects as the dominant dispersion processes.

In conclusion, p exerts its effect on HETP and R_{P} through influencing

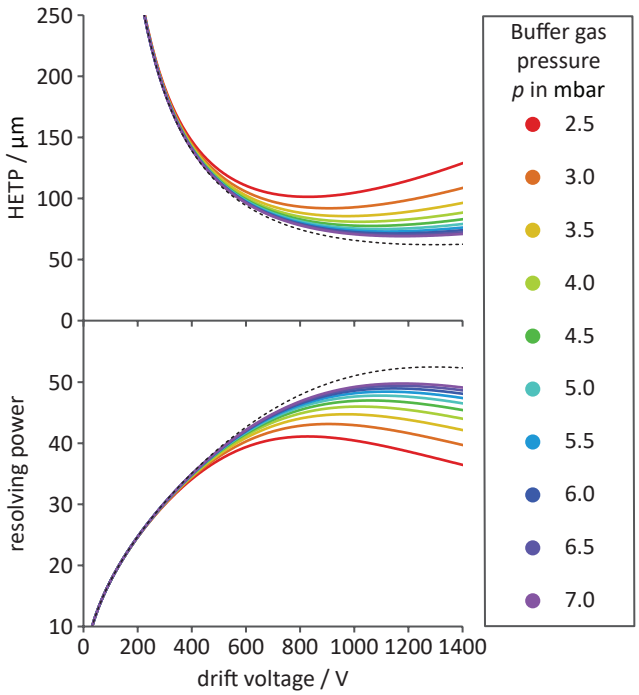

Figure 4.7: Influence of the buffer gas pressure on the plate height and the resolving power in DTIM-MS. Different colors encode different p values, ranging from 2.5 mbar to 7.0 mbar in ten equidistant steps as indicated. The black dashed lines (identical to those in Figure 4.6) correspond to the fundamental HETP and R_P limits determined by diffusion and Coulomb repulsion. These limits are entirely independent of p. Calculations were performed according to Eqs. 4.52 and 4.54 with the following input parameters: He buffer gas, $t_{inj} = 150\,\mu s$, $T = 298.15\,K$, $L_D = 805.5\,mm$, $L_{fun} = 144\,mm$. E_{fun} was kept constant at $10\,V\,cm^{-1}$. K values were derived according to the Mason–Schamp equation for the hypothetical analyte with $CCS_{He} = 200\,Å^2$, $m = 1000\,Da$, and $|z| = 1$. $Q = 100\,000\,e$, $C_{Clmb} = 3$, $C_{inj} = 12$, and $\theta = 1$ were assumed in the calculations.

the spatial spread of the injected ion packet. Furthermore, increasing p inside the separation region also enables the application of higher V_D by reducing the probability of discharges and expanding the low-field limit towards higher DC electric fields.

Collision cross section. As mentioned before, K has a strong impact on zone broadening in DTIM separations. Remarkably different HETP and R_P values may be attained for different analytes under otherwise identical conditions, *e.g.* within a single analytical run. The two most important analyte-related features influencing K are the CCS and the charge state z. Although ionic masses have a weaker influence on K, they play a prominent role when separating isotopologues or, more generally, when they are comparable

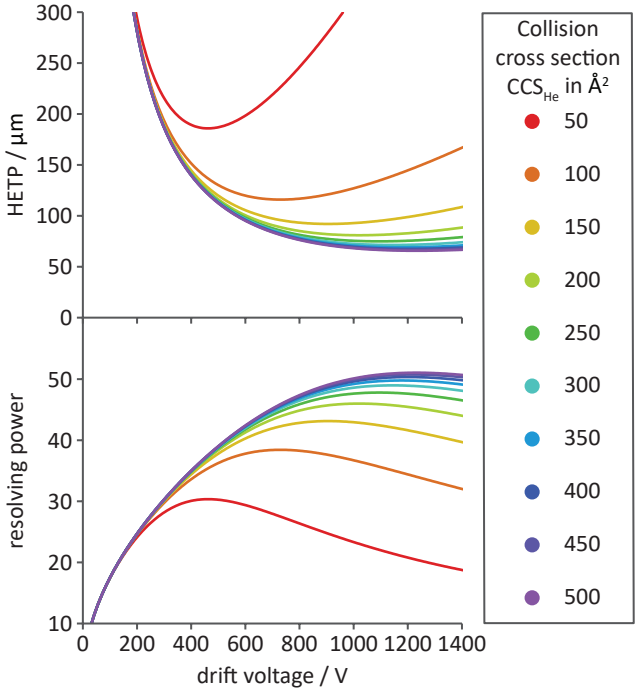

Figure 4.8: Influence of the collision cross section on the plate height and the resolving power in DTIM-MS. Different colors encode different hypothetical analytes with CCS_{He} values ranging from 50 Å^2 to 500 Å^2 in ten equidistant steps as indicated. Calculations were performed according to Eqs. 4.52 and 4.54 with the following input parameters: He buffer gas, $p = 4$ mbar, $t_{inj} = 150$ µs, $T = 298.15$ K, $L_D = 805.5$ mm, $L_{fun} = 144$ mm. E_{fun} was kept constant at 10 V cm^{-1}. K values were derived according to the Mason–Schamp equation for the hypothetical singly charged analytes. Although their influence on K is negligible, ionic masses were adjusted to mimic an isotropic growth pattern: $m = 150$ Da, 350 Da, 650 Da, 1000 Da, 1400 Da, 1850 Da, 2350 Da, 2900 Da, 3500 Da, and 4150 Da (in the order of increasing CCS_{He}). $Q = 100\,000\,e$, $C_{Clmb} = 3$, $C_{inj} = 12$, and $\theta = 1$ were assumed in the calculations.

to the mass of the buffer gas particles.[28,290–292]

Figure 4.8 highlights the effect of the CCS on HETP and R_P, considering the separation of singly charged ions with CCS_{He} values ranging from 50 Å^2 to 500 Å^2, but otherwise under identical conditions. Because CCS_{He} values are not experimentally or computationally determined, the superscript specifying the method is omitted. As CCS_{He} values become larger, $V_{D,opt}$ and $R_{P,max}$ increase monotonously, while $HETP_{min}$ decreases accordingly. Thus, within a single charge state, sharper zones can be achieved for ions with larger CCS_{He}. Since the extent of diffusional and Coulombic broadening is independent of the CCS_{He}, terms **A**, **C**, and **D** are not affected. A change in the CCS_{He} influences only **B**, similarly to the cases of varying t_{inj} and p.

Because the CCS, μ, and thus K are influenced by the nature of the buffer gas, changing the separation medium may not only alter selectivity, but can also affect HETP and R_P. In terms of zone broadening, employing heavier and strongly interacting buffer gases, where higher CCS and μ values lead to decreased mobilities, has a similar effect to increasing p. For example, R_P values achieved in N_2 are often higher than those in He when otherwise identical experimental conditions are applied. This effect, again, can be explained by the reduction of **B**-terms when K values decrease.

Charge state. When dealing with complex samples, analysts often encounter ions in different charge states. Exploring the influence of $|z|$ on zone broadening is therefore of high practical importance. Because in terms of zone broadening the polarity is irrelevant, herein we always refer to the absolute value $|z|$. Figure 4.9 highlights how HETP and R_P vary across various charge states when all other parameters are kept unchanged, including Q being fixed at $100\,000\,e$. In its appearance, Figure 4.9 differs starkly from the previous three examples. First, curves corresponding to ions with different $|z|$ do not overlap at low V_D. This lack of overlap is due to the different **D**-terms reflecting $|z|$-dependent diffusional broadening in the drift cell. A second obvious difference is that curves in Figure 4.9 intersect each other at different V_D values. Besides having a strong impact on **D** and **A** (the latter incorporating diffusion in the funnel), $|z|$ also influences **B** and the spatial spread of the injected ion packet. Because of the latter, $V_\mathrm{D,opt}$ decreases systematically as $|z|$ values increase. Intersections are a result of these two antagonistic effects: decreasing **A** and **D** combined with an increasing **B**-term as $|z|$ adopts higher values. In more detail, as V_D is being increased, the function of an ion with lower $|z|$ intersects and surpasses the curves corresponding to highly charged species when the beneficial effect of a more compact injected ion packet overcomes the detrimental effect of increased diffusional broadening. The stark differences between Figure 4.9 and the previous three examples in this section thus stem from the fact that $|z|$ affects multiple terms in Eqs. 4.52 and 4.54, whereas t_inj, p, and the CCS only influence **B**.

Figure 4.9 also reveals the dependence of $R_\mathrm{P,max}$ and $\mathrm{HETP}_\mathrm{min}$ on $|z|$. Considering $R_\mathrm{P,max}$, it first increases upon moving from $|z| = 10$ towards the doubly charged species, then it drops significantly as $|z|$ is further decreased from 2 to 1. The dependence of $R_\mathrm{P,max}$ and $\mathrm{HETP}_\mathrm{min}$ on $|z|$ is the consequence of Coulomb repulsion and the nonuniformity of the separation field in DTIM-MS. Note that E_fun is kept constant at $10\,\mathrm{V\,cm^{-1}}$, which influences the drift and dispersion of different ions differently. Interestingly, considering stand-alone DTIMS in the absence of space charge effects, $R_\mathrm{P,max}$ and $\mathrm{HETP}_\mathrm{min}$ do

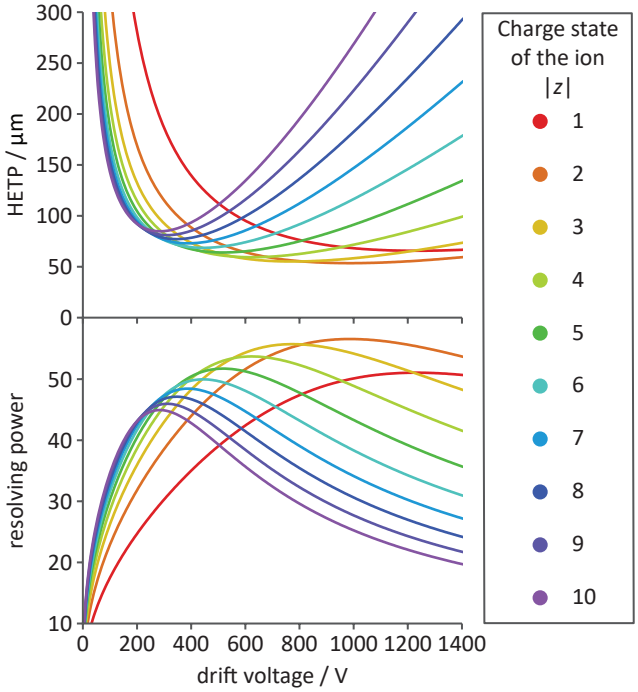

Figure 4.9: Influence of the ionic charge on the plate height and the resolving power in DTIM-MS. Different colors encode different hypothetical analytes with $|z|$ values ranging from 1 to 10, the polarity being irrelevant. Apart from $|z|$, ions were otherwise identical: $CCS_{He} = 500\,Å^2$, $m = 4150\,Da$. Calculations were performed according to Eqs. 4.52 and 4.54 with the following input parameters: He buffer gas, $p = 4\,mbar$, $t_{inj} = 150\,µs$, $T = 298.15\,K$, $L_D = 805.5\,mm$, $L_{fun} = 144\,mm$. E_{fun} was kept constant at $10\,V\,cm^{-1}$. K values were derived according to the Mason–Schamp equation. Irrespective of $|z|$, Q was kept uniformly at $100\,000\,e$. $C_{Clmb} = 3$, $C_{inj} = 12$, and $\theta = 1$ were assumed in the calculations.

not depend on $|z|$. For more detail on this aspect of the injection-diffusion model of stand-alone DTIMS, see Eqs. 4.45 and 4.49 on pages 60 and 61, respectively.

As a brief summary of Section 4.2, an analytical was developed to describe zone broadening in DTIM separations. Similarly to its counterparts in chromatography, the model views zone dispersion as a result of independently acting physical processes (Section 4.2.2). In the center of the model is Eq. 4.52, an extended plate-height equation for DTIM-MS (Section 4.2.3). To test the accuracy of this formula, a series of systematic measurements were performed, resulting in good agreement between experiment and theory (Section 4.2.4). Owing to their simplicity, Eq. 4.52 and related expressions can be readily implemented in spreadsheets, which enables the theoretical prediction of

zone broadening without ion trajectory simulations and extensive numerical calculations (Section 4.2.5). The model also provides the means to directly compare the performance of DTIM separations to that of other differential migration techniques, such as chromatography or zone electrophoresis.

In addition to its merits, we should also mention the limitations of the model at the above presented, incomplete stage of development. Figure 4.8 and Figure 4.9 showed the challenges represented by samples containing a large number of analytes that cover a wide range of K values. Finding the optimal experimental conditions for such separations is difficult, especially if one relies on figures of merit that are defined based on a single peak. Providing adequate solution to this complex issue requires more advanced indices of separation efficiency than HETP, N, or R_{P}. Thus, in the following sections we extend the model using concepts borrowed from the theoretical toolbox of chromatography. Instead of centering our attention on a single, arbitrarily chosen peak, we shall look on increasingly broader sections of the ion mobility spectrum. By doing so, suitable expression can be derived that describe the actual resolution between two neighboring peaks and, ultimately, the maximum number of resolvable components in a single separation.

4.3 Peak-to-peak resolution and selectivity

In Section 4.2 we explored zone broadening in DTIM separations through developing the basis of a plate-height model. Building on these findings, the present section extends the model and explores peak-to-peak resolution in different IMS and IM-MS techniques. Following a brief introduction of the fundamental definition, we present a critical overview of chromatography-influenced resolution equations and provide improvements of existing formulae. In addition, we derive exact resolution equations for DTIM separations that are based on first principles instead of analogy-driven approaches. Finally, upon implementing simple modifications according to a semi-empirical model of TWIMS, the exact resolution equations are extended to separations utilizing traveling potential waves instead of a constant drift field.

4.3.1 Defining peak-to-peak resolution

Single-peak-based measures of zone broadening, such as HETP, N, and R_P, are highly useful indices to characterize and compare the performance of separation methods based on differential migration. However, the analyst facing a practical problem is often more interested in the actual resolution between two neighboring peaks. Peak-to-peak resolution, R_S, is a widely-employed, dimensionless measure of the extent of separation between two Gaussian signals:[36]

$$\begin{aligned} R_\mathrm{S} &= \frac{t_2 - t_1}{2\sigma_{\mathrm{t},1} + 2\sigma_{\mathrm{t},2}} \\ &= \frac{|\Delta t|}{4\langle\sigma_\mathrm{t}\rangle}. \end{aligned} \tag{4.55}$$

In Eq. 4.55, t_1 and t_2 are the centroid t_D (or retention time, migration time, *etc.*) values, while $\sigma_{\mathrm{t},1}$ and $\sigma_{\mathrm{t},2}$ are the corresponding temporal standard deviations of the distributions. By employing the absolute difference $|\Delta t|$ and the arithmetic mean of the standard deviations $\langle\sigma_\mathrm{t}\rangle$, a more concise formulation ensues. Despite the apparent similarity of the two phrases appearing in IMS literature, single-peak R_P and peak-pair-based R_S should not be confused. The first is related to the sharpness of a single zone, while the latter reflects separation between two adjacent peaks, influenced by both the width of the two signals and the distance between them.

The rationale behind Eq. 4.55 is the following: considering two identical Gaussians with the same area and σ_t, R_S is unity when the line tangents to the closer-lying inflection points of the peaks intersect at the baseline. Unit

resolution ($R_S = 1$) in these cases means that each peak overlaps 4.55% of the other peak's area, while baseline resolution ($R_S = 1.5$) results in a 0.27% overlap. The above values, however, vary at constant R_S if the two peaks are not identical: the same R_S value may apply to different peak pairs with different overlap, depending on the ratio of their areas and σ_t values. Thus, R_S is not a direct measure of cross-contamination, and alternative functions were developed that are better suited for preparative separations and non-Gaussian peak profiles.[241,293–295] Although many of these functions reflect peak overlap more accurately, they are much more difficult to calculate from experimental data and have no clear advantages over Eq. 4.55 in analytical separations, impeding their widespread application. Thus, in separation science, Eq. 4.55 serves as a practical and universally recommended index for measuring resolution between peaks. Owing to its simplicity, popularity, direct connection to peak capacity (see later), and the fact that it served as the starting point for predictive resolution equations in chromatography and electrophoresis, we also choose Eq. 4.55 as the basic definition to derive predictive formulae for stand-alone IMS and IM-MS.

4.3.2 Chromatography-influenced resolution equations

Being a general definition and entirely descriptive, Eq. 4.55 merely specifies the way R_S should be calculated in case an ion mobility spectrum, chromatogram, *etc.*, is given. It does not help us identify underlying factors that influence R_S, nor does it help to find the optimal separation conditions. Therefore, predictive equations need to be derived that reveal the fundamental factors determining resolution, aid the optimization of separations in practice, and may estimate R_S under defined experimental conditions. In the present section we follow an analogy-driven strategy to obtain such predictive formulae. Equations derived originally for chromatography may be modified to be applicable to DTIM separations. Although the resulting equations inherit various limitations and have some inherent shortcomings, this approach offers a simple solution to the problem of finding an expression for R_S with predictive potential.

Equal peak width assumption. Assuming $\sigma_{t,1} + \sigma_{t,2} = 2\sigma_{t,2}$, Purnell derived a predictive resolution equation for column chromatography under

linear elution conditions:[296]

$$R_{\mathrm{S,chrom}} = \frac{\sqrt{N_2}}{4}\frac{k_2 - k_1}{1 + k_2} = \frac{\sqrt{N_2}}{4}\frac{\alpha - 1}{\alpha}\frac{k_2}{1 + k_2}. \tag{4.56}$$

In Eq. 4.56, N_2 is the plate number for the later eluting component, k_1 and k_2 are the retention factors of the respective compounds, while α is the separation factor expressing intrinsic selectivity: $\alpha = k_2/k_1$. The subscript in $R_{\mathrm{S,chrom}}$ refers to chromatography. For clarity, in equations that are specific for a certain separation technique, the respective technique is always indicated in the subscript of R_{S}.

Employing the same equal peak width assumption but concentrating on the first peak ($\sigma_{\mathrm{t},1} + \sigma_{\mathrm{t},2} = 2\sigma_{\mathrm{t},1}$), Knox[297] and Thijssen[298] arrived at the following formula:

$$R_{\mathrm{S,chrom}} = \frac{\sqrt{N_1}}{4}\frac{|\Delta k|}{1 + k_1} = \frac{\sqrt{N_1}}{4}(\alpha - 1)\frac{k_1}{1 + k_1}. \tag{4.57}$$

Here, N_1 is the plate count for the earlier eluting solute and $|\Delta k|$ stands for the absolute difference of retention factors. Eqs. 4.56 and 4.57 are equivalent and yield the same result as Eq. 4.55, provided the assumption of equal peak widths is satisfied: $\sqrt{N_1}(1 + k_2) = \sqrt{N_2}(1 + k_1)$. This criterion, however, is often not met in practice, in which case Eqs. 4.56 and 4.57 cease to be equivalent and the choice to apply one or the other becomes arbitrary. If the second peak is broader, as in most cases, R_{S} values predicted by Eq. 4.56 will be systematically lower, while those predicted by Eq. 4.57 will be systematically higher than the reference values calculated according to Eq. 4.55. Detailed derivations of the resolution equations presented in Section 4.3 can be found in Appendix B.

The first predictive resolution equation for DTIMS was based on Eq. 4.56, inheriting its limitations stemming from the equal peak width assumption:[299]

$$R_{\mathrm{S,DTIMS}} = \frac{\sqrt{N_2}}{4}\frac{\alpha - 1}{\alpha}. \tag{4.58}$$

Here, α is defined as the ratio of mobilities instead of the ratio of retention factors as in chromatography ($\alpha \geq 1$ by convention). The subscript indicates that Eq. 4.58 is specific to DTIMS.

The general reasoning to obtain Eq. 4.58 is as follows: the time the ions require to traverse an empty drift cell in perfect vacuum (*i.e.* the analogue of the chromatographic void time) is negligibly short compared to the actual t_D in gas-filled cells (equivalent of the retention time). Therefore, retention factors in DTIMS are virtually infinite, meaning that the chromatographic migration factor $k_2/(1+k_2) \approx 1$ and may be omitted. The above reasoning, however, is not justified by physical models and may be misleading: it implies that DTIMS is a chromatography-like process with retention playing a central role. Instead, DTIMS is a gas-phase electrophoretic process where convective flow or partition between stationary and mobile phases are absent. Therefore, void time and retention (factors) cannot be interpreted in relation to this technique.

Despite the shortcomings of the underlying argumentation, Eq. 4.58 proved to be of high practical utility for DTIMS. Thus, instead of a complete rejection of the above analogy-based approach, it is worth attempting to improve the accuracy of Eq. 4.58 and overcome its limitations that stem from the inadequate equal peak width assumption.

Equal plate number assumption and exact solutions. A generally more valid assumption for close-lying peaks in isocratic elution chromatography and DTIMS is that of equal plate numbers. Assuming $N_1 = N_2 = N$, Karger derived the following equation for chromatography:[300]

$$\begin{aligned} R_\mathrm{S,chrom} &= \frac{\sqrt{N}}{4}\frac{|\Delta k|}{1+\langle k\rangle} \\ &= \frac{\sqrt{N}}{4}\left(2\frac{\alpha-1}{\alpha+1}\frac{\langle k\rangle}{1+\langle k\rangle}\right), \end{aligned} \tag{4.59}$$

where $\langle k\rangle$ is the arithmetic mean of the retention factors. In analogy to Eq. 4.58, from the above equation we may obtain the following formula for DTIMS:

$$R_\mathrm{S,DTIMS} = \frac{\sqrt{N}}{2}\frac{\alpha-1}{\alpha+1}. \tag{4.60}$$

An exact solution requiring no assumption on σ_t or N was derived by Said[301,302] and Suematsu and Okamoto[303] by introducing an effective average plate number:

$$N_\mathrm{avg} = \left(\frac{\langle t_\mathrm{R}\rangle}{\langle \sigma_\mathrm{t}\rangle}\right)^2. \tag{4.61}$$

N_avg corresponds to a hypothetical analyte eluting between the two solutes: $\langle t_\mathrm{R}\rangle$ is the arithmetic mean of the two retention times, while $\langle \sigma_\mathrm{t}\rangle$ is the

arithmetic mean of $\sigma_{t,1}$ and $\sigma_{t,2}$. In practice, the N_1/N_2 ratio is generally close to 1, in which case the arithmetic[302,304] or geometric mean[305] of the plate numbers are good approximations for N_{avg}. The resulting exact predictive resolution equation is very similar to Eq. 4.59,

$$R_{S,chrom} = \frac{\sqrt{N_{avg}}}{4}\frac{|\Delta k|}{1+\langle k\rangle} = \frac{\sqrt{N_{avg}}}{4}\left(2\frac{\alpha-1}{\alpha+1}\frac{\langle k\rangle}{1+\langle k\rangle}\right), \tag{4.62}$$

the only difference being the presence of N_{avg}. The term in parenthesis reflects the relative velocity difference of the analytes. The equation above reveals the influence of fundamental separation parameters on resolution, does not suffer from the shortcomings of Eqs. 4.56 and 4.57, and yields the same R_S values as Eq. 4.55 in all cases, irrespective of the peak width or plate number ratios. From Eq. 4.62 the corresponding accurate formula for DTIMS can be readily obtained:

$$R_{S,DTIMS} = \frac{\sqrt{N_{avg}}}{2}\frac{\alpha-1}{\alpha+1}. \tag{4.63}$$

Here, N_{avg} is calculated according to Eq. 4.61, using t_D instead of t_R values. Inheriting the above-mentioned advantages of Eq. 4.62, Eq. 4.63 appears as a suitable choice for a predictive resolution equation in DTIMS.

Figure 4.10 compares the performance of chromatography-influenced predictive resolution equations for DTIMS, highlighting their trueness under a broad range of settings. The left-hand side portrays the situation with equal plate numbers assumed for the two analytes. R_S values predicted by equations based on the equal peak width assumption (light blue and red traces) show increasing deviation from the true R_S with growing values of α, that is, as the distance between the peaks in the ion mobility spectrum increases. Although the experimentally most relevant region is that of close-lying peaks where α is relatively low, the results clearly indicate the limitations of the equal peak width assumption. The right-hand side represents a different setting: the $\sigma_{t,2}/\sigma_{t,1}$ ratio is swept between 1 and 1.5, while α is held constant at 1.05. As the second peak becomes broader relative to the first, equations based on various assumptions show increasing systematic deviation. Meanwhile, the exact equation (Eq. 4.63) successfully predicts the true value of R_S in the entire range. An empirical formula, where N_{avg} is approximated by the geometric mean of the two plate numbers, yields results sufficiently close to the true value and thus proves to be a good alternative in practice. Interestingly,

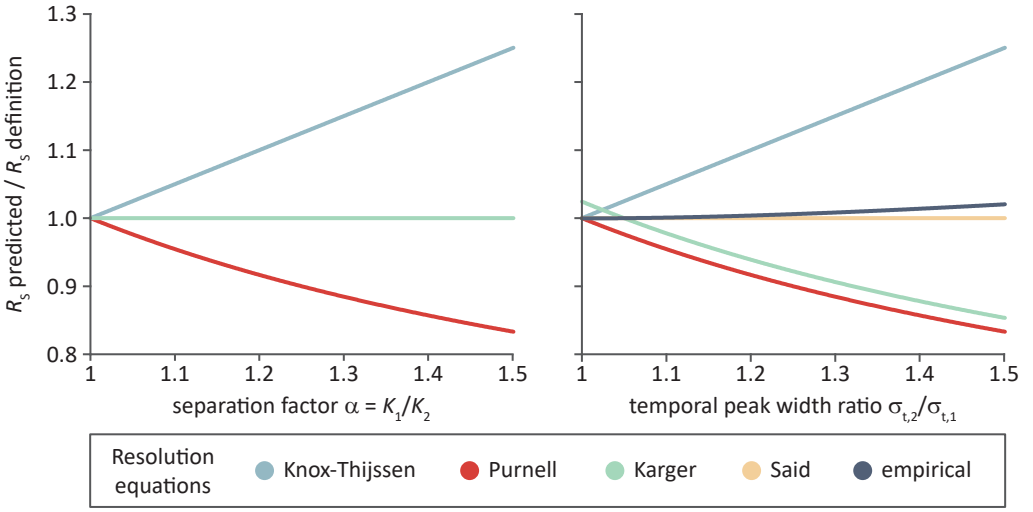

Figure 4.10: Comparison of chromatography-influenced resolution equations for drift tube ion mobility spectrometry. Peak-to-peak resolution R_S calculated according to the various predictive resolution equations for DTIMS. Equations are color coded, and the names refer to the respective chromatographic equations they derive from. In the empirical formula (dark blue trace), N_{avg} is approximated by the geometric mean of the plate numbers: $\sqrt{N_1 N_2}$. Predicted R_S values are divided by the exact value of R_S as defined in Eq. 4.55, that is, a value of 1 represents perfect agreement. As $\alpha = 0$ leads to zero R_S, the plotted functions are not defined at this point. (left) Trueness of predicted R_S as a function of α, the ratio of ion mobilities. In these calculations, equal plate counts were assumed for the two components ($N_1 = N_2$). Owing to the normalization of R_S values the absolute number of plates is indifferent. The exact and empirical equations would coincide with the green trace. (right) Trueness of predicted R_S as a function of the temporal peak width ratio, $\sigma_{t,2}/\sigma_{t,1}$. The ratio of plate numbers changed according to the peak width ratio ($\sqrt{N} \propto 1/\sigma_t$). In the calculations, α was fixed at 1.05, corresponding to 5% difference in mobilities. For calculating the green trace (equal plate number assumption), N_2 was used when the two plate counts differed.

the green trace reproduces the true value at exactly one point: where the peak width ratio equals the value $\alpha = 1.05$. At this point $N_1 = N_2$, meaning the assumption the equation is based on is satisfied.

4.3.3 Resolution equations from first principles

To give a more solid physical foundation to the prediction of R_S values in DTIMS, and to circumvent the controversial argumentation behind the chromatography-influenced formulae in the previous section, herein we rely on first principles and simple algebra to derive suitable resolution equations for this separation technique. Starting from Eq. 4.55 on page 75, it can be shown that in all differential migration methods R_S depends on two independent

factors: the rate of dispersion expressed by N_{avg}, and the relative velocity difference of the analytes, δ_{v}:[249]

$$\begin{aligned} R_{\mathrm{S}} &= \frac{|\Delta t|}{4\langle\sigma_{\mathrm{t}}\rangle} \\ &= \frac{\sqrt{N_{\mathrm{avg}}}}{4}\frac{|\Delta t|}{\langle t\rangle} \\ &= \frac{\sqrt{N_{\mathrm{avg}}}}{4}\frac{|\Delta v|}{\langle v\rangle} \\ &\equiv \frac{\sqrt{N_{\mathrm{avg}}}}{4}\delta_{\mathrm{v}}. \end{aligned} \tag{4.64}$$

In Eq. 4.64, v_{i} is the average velocity of the ith analyte zone through the separation field, defined as $v_{\mathrm{i}} = L/t_{\mathrm{i}}$. As each analyte migrates through the same conduit (tube, column, *etc.*) with length L, $|\Delta t|/\langle t\rangle = \delta_{\mathrm{v}}$. Although in stand-alone DTIMS, zone electrophoresis, and column chromatography under isocratic conditions, the analytes migrate at constant velocity, there is no need to assume constant velocity to arrive at the above equation. We may look at δ_{v} as the operational selectivity, describing the relative migration of two analytes in the same separation field. In DTIMS, δ_{v} is the ratio of the difference and the arithmetic mean of two v_{D} values, and as such, adopts values in the range $0 \leq \delta_{\mathrm{v}} < 2$. Although cases where one of the analyte zones is stagnant or the velocity vectors point to opposite directions are interesting on their own merit, due to their irrelevance to standard DTIMS these are not considered here in relation to δ_{v}.

In Eqs. 4.59 and 4.62, δ_{v} is expressed using retention factors and the separation factor, α being inherited by the corresponding equations for DTIMS. Instead of relying on chromatographic parameters stemming from an analogy-driven approach, this section aims to utilize first principles and relate δ_{v} to fundamental parameters of IMS itself. In DTIMS, v_{D} is directly proportional to K, the proportionality factor being E_{D}. Thus, from Eq. 4.64 that is valid for various differential migration processes, we arrive at the following DTIMS-specific equation:

$$R_{\mathrm{S,DTIMS}} = \frac{\sqrt{N_{\mathrm{avg}}}}{4}\frac{|\Delta K|}{\langle K\rangle}. \tag{4.65}$$

The above formula is very similar to its well-known counterpart for zone electrophoresis, the main differences being the appearance of gas-phase K values instead of their condensed-phase analogues, and the absence of an

equivalent for the electroosmotic flow.[306] By employing the relation $\alpha = K_1/K_2$[299], Eqs. 4.63 and 4.65 can be shown to be equivalent, providing a mutual validation. Because no assumption was made during derivation, Eq. 4.65 is exact, and clearly shows how to improve R_S in practice. Besides the possibility of decreasing zone broadening, one may try to influence the relative mobility of the two analytes through altering the separation conditions. If we aim to apply Eq. 4.65 for DTIM-MS instead of stand-alone DTIMS, N_{avg} can be simply multiplied with $(1 - F)^2$ according to Eq. 4.38 on page 58. For simplicity, we use uniformly DTIMS in the subscript of predictive resolution equations.

To explore the possibility of influencing the relative mobility in detail, let us utilize the Mason–Schamp equation and relate K to quantities more closely related to the ion structure and the characteristics of the collision complex:

$$K = C\frac{z}{\mathrm{CCS}\sqrt{\mu}}. \tag{4.66}$$

In Eq. 4.66, C integrates all factors (physical constants, measurement conditions, *etc.*) that are the same for all ions in an experiment, thereby emphasizing the three analyte-specific features. These can be combined into a single variable, the reduced mass and charge-normalized collision cross section:

$$\mathrm{CCS'} = \frac{\mathrm{CCS}\sqrt{\mu}}{|z|}. \tag{4.67}$$

Ultimately, DTIMS separates gas-phase ions according to their CCS' values. Thus, employing CCS' that we defined as a positive quantity, Eq. 4.65 may be reformulated to obtain the following expression for DTIMS:

$$R_{S,\mathrm{DTIMS}} = \frac{\sqrt{N_{avg}}}{4}\frac{|\Delta\mathrm{CCS'}|}{\langle\mathrm{CCS'}\rangle}. \tag{4.68}$$

This solution is exact and relates δ_v to CCS' values of the analytes in the given buffer gas, which are characteristic to the ion-–neutral complex and can potentially be stored in databases. Thus, Eq. 4.68 is accurate and practical, has a high predictive potential, and reveals how δ_v can be influenced in DTIM separations, which we address below in detail.

Influence of the reduced mass on selectivity. The dependence of CCS' on μ enables analysts to optimize conditions for separations concerning ions with nonidentical masses, such as the separation of isotopes or isotopologues in stand-alone IMS. The larger the mass of the gas particles compared to the masses of the two ions, the larger the relative difference between the μ values

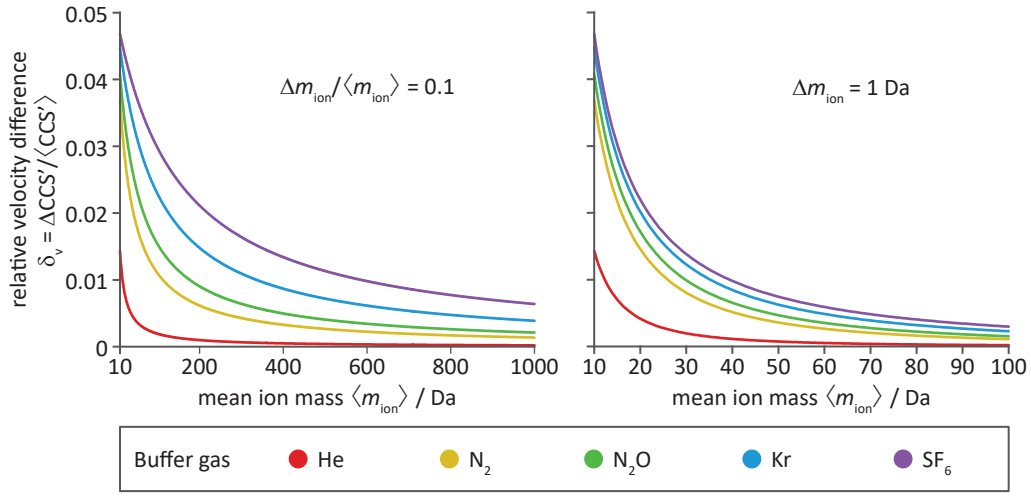

Figure 4.11: Influence of the reduced mass difference on selectivity in DTIMS. (left) Relative velocity difference $\delta_v = |\Delta CCS'|/\langle CCS'\rangle$ of ion pairs with identical CCSs and nonidentical masses (mimicking isotopologue separations), plotted as a function of the mean ion mass $\langle m_{ion}\rangle$. Colors encode representative buffer gases, ranging from the lightest (He) to the heaviest (SF_6) gas applied in practice. The relative mass difference of the ion pairs, $\Delta m_{ion}/\langle m_{ion}\rangle$, was held constant at 0.1. (right) Analogous δ_v *v.* $\langle m_{ion}\rangle$ plot showing the effect of a constant absolute mass difference Δm_{ion}. Instead of keeping $\Delta m_{ion}/\langle m_{ion}\rangle$ fixed as on the left, here the absolute value Δm_{ion} was held constant at 1 Da, resulting in a more rapid drop of δ_v with increasing ion mass. Note the difference between the ion mass ranges on the two plots. For completeness, the buffer gases used in the calculations with their rounded standard atomic/molecular weight in Da: He 4, N_2 28, N_2O 44, Kr 84, SF_6 146. In the calculations, all stable isotopes/isotopologues of the buffer gas particles were considered, weighted with their relative abundances.

of the respective collision complexes will be, provided the ion masses differ. Thus, δ_v may be tailored and R_S consequently improved by the adjustment of the buffer gas atomic/molecular weight for the separation of lighter ions with different masses.[291,307]

Figure 4.11 explores in detail how differences in μ can be exploited to influence selectivity in DTIMS. To study the effect of reduced mass difference on δ_v independently of other influencing factors, the CCS and z were assumed to be identical, the absolute values being irrelevant. Although kinetic theory[308,309] and some experiments[291] suggest that isotopologues may have extremely small differences in their CCS values, for practical purposes the assumption of identical CCSs remains generally valid.[290,292] The two plots in Figure 4.11 depict for analyte pairs with nonidentical masses δ_v as a function of their mean mass $\langle m_{ion}\rangle$. The colors represent different buffer gases, ranging from the lightest (He) to the heaviest (SF_6) gas applied in practice. It is apparent that δ_v decreases rapidly with increasing $\langle m_{ion}\rangle$, and that heavier

gases lead to improved selectivity for isotopologues: the heavier the gas relative to the ions, the larger δ_v will be. On the left, the relative mass difference of ions, $\Delta m_{ion}/\langle m_{ion}\rangle$, was kept constant at 0.1. For an ion pair with 10 Da average mass, it means 1 Da absolute difference, that is, 9.5 and 10.5 Da for the two species. For a pair with 100 Da mean mass, the difference is 10 Da. With the gas particles becoming heavier, μ approaches m_{ion}. Consequently, for any given value of $\langle m_{ion}\rangle$, δ_v converges to $(\Delta\sqrt{m_{ion}})/\langle\sqrt{m_{ion}}\rangle$ (corresponding uniformly to roughly 0.05 in Figure 4.11, left panel) as the mass of the gas particles increases. It is apparent that for heavy ions the aforementioned convergence of δ_v is very slow, and the values remain low under experimentally feasible conditions ($m_{gas} < 150\,\mathrm{Da}$). On the right-hand side of Figure 4.11, the absolute mass difference between the members of each ion pair was fixed at 1 Da. Thus, $\Delta m_{ion}/\langle m_{ion}\rangle$ decreases with increasing $\langle m_{ion}\rangle$, and δ_v drops even more rapidly as the analytes become heavier. Note the difference between the range of $\langle m_{ion}\rangle$ values chosen in the two plots. The above analysis did not involve gas mixtures, but the presence of multiple gas isotopes/isotopologues were considered.[290,310] Despite the simplicity of the model, the main trends and strategies to exploit differences in ion mass to improve δ_v could be revealed.

Influence of the collision cross section on selectivity. As the ratio of two ions' CCSs may also depend on the buffer gas composition, the effect of different buffer gases[311–313] and gas-phase modifiers[314,315] on selectivity have been extensively studied. Altering the ratio of the CCSs through changing or doping the buffer gas potentially enables the analyst to tailor selectivity in (low-field) DTIMS, with particular relevance to isomer separations. However, in comparison to more flexible chromatographic and condensed-phase electrophoretic separations where selectivity can be influenced by tuning a myriad of parameters and conditions over a broad range, the possibilities in IMS are more restricted, and the resulting effects are less striking. The choice of buffer gas may of course also affect N through influencing transport properties, which is important as R_S depends on both N_{avg} and δ_v.

Arguably the most important application of DTIMS is the separation of isomers, where differences in the CCSs represent the only aspect of selectivity. As μ is the same for isomeric species, Eq. 4.68 can be simplified (assuming the two analytes are in the same charge state):

$$R_{S,DTIMS} = \frac{\sqrt{N_{avg}}}{4}\frac{|\Delta CCS|}{\langle CCS\rangle}. \tag{4.69}$$

Eq. 4.69 is similar to that proposed by Dodds *et al.*[316], the difference being the appearance of N_{avg} defined according to Eq. 4.61 on page 78. As shown

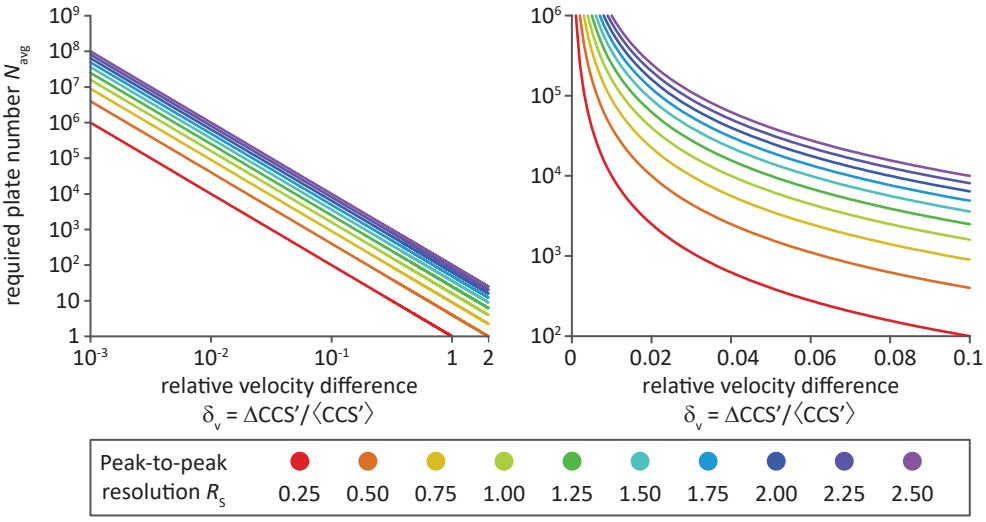

Figure 4.12: Number of theoretical plates needed to achieve defined resolution between two peaks in DTIMS. (left) Double-log plot showing the required N_{avg} to reach specified R_S values as a function of the two analytes' relative velocity difference. In DTIMS $0 \leq \delta_v < 2$ but values close to the theoretical upper limit are of little practical relevance. $R_S = 1.5$ corresponds to baseline separation. An n-fold increase in R_S requires an n^2-fold increase in N_{avg}. (right) Single-log plot highlighting the most relevant and experimentally accessible region. Separations in practice usually concern analyte pairs with $\delta_v < 0.1$. At present, state-of-the-art high-pressure linear DTIMS instruments may achieve theoretical plates on the order of 10^5.

in Figure 4.12, Eqs. 4.68 and 4.69 can also be utilized to calculate the number of plates required to achieve a specified R_S value for a given analyte pair. The plots highlight the intertwined influence of resolving power (expressed by N_{avg}) and selectivity (expressed by $|\Delta CCS'|/\langle CCS' \rangle$) on the ultimately achieved peak resolution in DTIMS. In general, $R_S = 0.75$ is required to readily distinguish two peaks, whereas $R_S = 1.5$ marks baseline separation by convention. As cutting-edge high-pressure DTIMS instruments may achieve plate numbers on the order of 10^5, separating isomers with roughly 0.5–1% CCS difference represents the current limit of this technique.[175]

There is little playing field for the analyst to influence z selectively, but its effect is important to understand and predict R_S for ions having the same m/z value but different mass and charge, such as various oligomers. In the discussion above, the separation of isotopologues, isomers, and oligomers serve as representative examples. In most analytical problems, especially those concerning stand-alone DTIMS, it is the combined effect of z, μ, and the CCS that needs to be evaluated in relation to selectivity, as expressed by the single variable CCS' in Eq. 4.68.

As a final remark to Section 4.3.3, in relation to Eqs. 4.65, 4.68, and 4.69, we shall briefly address the possibility of predicting selectivity in DTIMS relying solely on theoretical approaches. First, state-of-the-art computational methods are capable of generating correct structural models for gas-phase molecular ions of ever-increasing complexity. Second, two-body interactions governing separation in IMS are much more amenable to computational treatment than many-body encounters determining retention in chromatography.[317]. If the aforementioned suitable ion structures are available, K and the CCS can be calculated in a variety of buffer gases with satisfying accuracy.[30,195–199] Thus, with increasing computational power and further progress of theoretical methods, the prospect of predicting selectivity in DTIMS entirely computationally, at least for simpler systems, does not seem far-fetched.

4.3.4 From constant fields to traveling waves

By extending the approach employed for DTIMS above, in this section we aim to find a predictive resolution equation for TWIMS.[177,178] Due to the lack of a complete, general analytical model that would describe the electrophoretic motion of ions propelled by traveling potential waves, we cannot attempt to address zone broadening in TWIMS the way it was done for DTIM separations in Section 4.2. However, based on a widely-employed, semi-empirical model of TWIMS, we may readily address the subject of selectivity in this technique. In contrast to DTIMS, where v_D is directly proportional to K, this dependence in TWIMS is nonlinear and cannot be traced back to first principles.[180] Therefore, Eq. 4.65 on page 81 and subsequent equations derived from this formula are not applicable to the latter IMS technique.

A possible solution to the above problem is to transfer TWIM separations from their fundamental spatial and temporal dimensions into the CCS domain, that is, accounting for the altered selectivity by including its effect into a modified CCS-based definition of N or R_P.[316] While this approach has some advantages, it ultimately blurs the clear distinction between two independent aspects of peak resolution: zone broadening and selectivity. The method-specific, arbitrary modification of fundamental definitions (N and R_P) also leads to some dissonance between this approach and the unified theoretical toolbox of differential migration methods.[36]

Here, we provide a solution that is mathematically equivalent to that mentioned above, but fits into the general formalism of separation science. To obtain the desired formula for TWIMS, a suitable expression has to be found for δ_v and substituted into Eq. 4.64. In general, the following power function is employed for CCS calibration in TWIMS, that is, to describe the relation

between CCS' and the ion transit time through the mobility cell:[182,183]

$$\text{CCS'} = a \cdot (t_\text{D})^b. \tag{4.70}$$

The above equation is identical to Eq. 2.5 on page 24, written in a more concise form using the notation CCS'. The parameters a and b depend on measurement conditions, and may be readily determined through the general CCS calibration procedure for TWIMS using suitable calibrants. Employing the above semi-empirical relation to express δ_v, and introducing the notation $1/b = \gamma$, the following predictive resolution equation can be formulated for TWIMS:

$$R_{\text{S, TWIMS}} = \frac{\sqrt{N_\text{avg}}}{4} \frac{(\text{CCS'}_2)^\gamma - (\text{CCS'}_1)^\gamma}{\langle(\text{CCS'})^\gamma\rangle}. \tag{4.71}$$

The exponent γ accounts for the altered selectivity in TWIMS. While in DTIM separations $\gamma = 1$, in TWIMS it exceeds 1 in general, with clearly favorable consequences to δ_v and R_S. Besides determination through calibration, γ may be estimated theoretically for close-lying peaks under certain assumptions. As an illustrative example, for symmetric triangular waveforms γ adopts a value of 2 if the maximum ion velocity is much lower than the wave velocity.[180,181]

As of today, no complete analytical model has been developed that could accurately describe ion motion in TWIMS cells operated with discretely stepping potential waves, which makes the technique dependent on suitable calibrants. However, the recent development of a model for hypothetical, smoothly moving waves[180] marks a significant step towards the ultimate goal of TWIMS theory: an exact equation derived from first principles, describing the universal relation between K and the ions' transit time through the mobility cell. If such a model was available for TWIMS, it would be possible to depart from semi-empirical equations and place selectivity and zone broadening on purely theoretical foundations.

4.4 Peak capacity in ion mobility separations

In Section 4.2 we centered out attention on single peaks, aiming to model zone broadening in DTIMS and DTIM-MS. However, the very essence of separations is difficult to capture when we look at only one component at a time. Therefore, building on the findings concerning zone broadening, in Section 4.3 we looked at pairs of neighboring peaks, searching for exact resolution equations with high predictive potential. The connection between zone broadening and resolution was selectivity, which we expressed as the relative difference of drift velocities. Making a step further in this direction, *i.e.* concentrating on an ever-increasing number of peaks in the ion mobility spectrum simultaneously, we may finally arrive at the idea of peak capacity: the maximum number of peaks resolvable in a single separation.

4.4.1 The peak capacity concept

The peak capacity, P_C, was introduced by Giddings for elution chromatography as a holistic measure of the separation efficiency.[318] As the concept is abstract and not linked to any physical model, it can be readily transferred to other differential migration methods. Briefly, P_C represents the maximum number of resolved peaks that can be fit into the separation window, *e.g.* a chromatogram, electropherogram, or ion mobility spectrum. It reflects the hypothetical case when peaks are ideally distributed, meaning that R_S is the same for any two neighboring peaks within a single dimension of the separation window. Although the exact value of R_S may be set arbitrarily, in general it is chosen to be 1 or 1.5 for practical reasons: values lower than unity would express significant peak overlap, whereas values higher than that of baseline separation would correspond to the suboptimal utilization of the separation window, with unoccupied, empty sections between peaks.

In addition to the predefined R_S value, P_C depends on two factors: the width of the peaks and the actively utilized size of the separation window. The narrower the peaks and the larger this window between the first and the last peak, the higher the peak capacity. Due to nonideal, often random distribution of peaks in real separations, the number of resolved components in reality is merely a fraction of this number as shown by Poisson statistics.[169,319] Thus, P_C may be viewed as an estimate of the total number of resolvable components, serving as a comprehensive measure of the overall separation performance. As it considers the separation window as a whole instead of one or two selected peaks, P_C is arguably the most suitable index to evaluate and compare separation methods dealing with complex mixtures. Electrophoretic techniques may generate extremely high plate counts, but the separation

window in these methods is rather narrow in comparison to chromatography, both in the liquid and the gas phase. For this reason, it is essential to obtain a suitable model for peak capacity in IMS.

To formulate an exact definition of P_C in the language of mathematics, let us consider the number of peaks n in an infinitesimally narrow section of the separation window:[320]

$$\frac{dn}{dt_D} = \frac{1}{4R_S\sigma_t(t_D)}. \tag{4.72}$$

Here, $\sigma_t(t_D)$ emphasizes that the peak width may vary across the ion mobility spectrum as a function of t_D, while R_S has a predefined and constant value (usually 1 or 1.5). From the integral form of Eq. 4.72,

$$\int_1^n dn = \frac{1}{4R_S}\int_{t_{D,1}}^{t_{D,n}} \frac{dt_D}{\sigma_t(t_D)}, \tag{4.73}$$

we may directly obtain the general, mathematical definition of P_C:[321]

$$P_C \equiv n = 1 + \frac{1}{4R_S}\int_{t_{D,1}}^{t_{D,n}} \frac{dt_D}{\sigma_t(t_D)}. \tag{4.74}$$

To highlight the dependence of P_C on the plate count, Eq.4.74 can be rewritten in the following alternative form:

$$P_C = 1 + \frac{1}{4R_S}\int_{t_{D,1}}^{t_{D,n}} \frac{\sqrt{N(t_D)}}{t_D} dt_D, \tag{4.75}$$

where N may also be a function of t_D.

The way N and σ_t depend on t_D is central to the peak capacity problem. Solving Eq. 4.74 or Eq. 4.75 to yield the desired closed-form expressions for P_C requires the explicit form of $N(t_D)$ or $\sigma_t(t_D)$ be known. In the following section, we first present two approximate solutions that are based on assumptions concerning the functions $N(t_D)$ and $\sigma_t(t_D)$. Following these assumption-based equations, we also present an exact solution to the peak capacity problem, derived from a suitable physical model of peak broadening in DTIMS.

4.4.2 Assumption-based peak capacity equations

The first P_C equations in chromatography were derived without considering actual physical models of band broadening.[318,320,322] Instead, they are based on different assumptions about N and σ_t, shown graphically in Figure 4.13. For completeness and comparison, in this section we present the equivalents of these assumption-based equations for DTIMS and TWIMS, and discuss the validity of the resulting formulae on the basis of the physical model developed in Section 4.2.

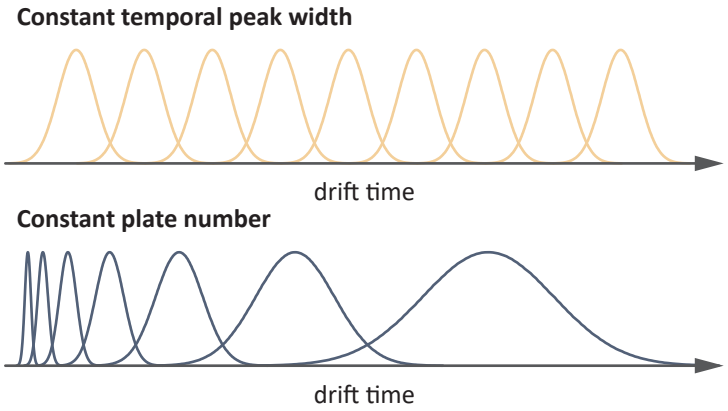

Figure 4.13: Constant temporal peak width (top) is often assumed in gradient elution chromatography, and may be applicable to DTIMS when the injection pulse determines the peak width. Constant plate count (bottom) means that the temporal width of each peak is directly proportional to its drift time. This assumption may be valid in chromatography under isocratic conditions, and in DTIMS when diffusion is the dominant dispersion process.

The constant plate number assumption. Assuming that N is the same for each peak and independent of t_D, that is, $\sigma_\mathrm{t}(t_\mathrm{D}) = t_\mathrm{D}/\sqrt{N}$ where N is constant, the solution of Eq. 4.75 yields the following equation:

$$\begin{aligned} P_{\mathrm{C},N} &= 1 + \frac{\sqrt{N}}{4R_\mathrm{S}} \int_{t_{\mathrm{D},1}}^{t_{\mathrm{D,n}}} \frac{\mathrm{d}t_\mathrm{D}}{t_\mathrm{D}} \\ &= 1 + \frac{\sqrt{N}}{4R_\mathrm{S}} \ln \frac{t_{\mathrm{D,n}}}{t_{\mathrm{D},1}}. \end{aligned} \tag{4.76}$$

Here, $t_{\mathrm{D},1}$ and $t_{\mathrm{D,n}}$ correspond to the first and last peak, respectively, while the subscript of $P_{\mathrm{C},N}$ indicates that N was assumed to be constant. The above equation is still general, and upon changing t_D to t_R it becomes identical to the simple formula for isocratic elution chromatography.[318,320]

From the inverse proportionality between t_D and K, a more revealing DTIMS-specific equation results:

$$P_{\mathrm{C,DTIMS},N} = 1 + \frac{\sqrt{N}}{4R_\mathrm{S}} \ln \frac{K_1}{K_\mathrm{n}}. \tag{4.77}$$

The error stemming from ignoring the mobility independent contributions to t_A in DTIM-MS is usually negligible, and thus Eq. 4.77 can also be applied when DTIMS is coupled to MS analysis. Instead of K, we may also use CCS' values to formulate a specific equation for DTIMS (and DTIM-MS):

$$P_{\mathrm{C,DTIMS},N} = 1 + \frac{\sqrt{N}}{4R_\mathrm{S}} \ln \frac{\mathrm{CCS'}_\mathrm{n}}{\mathrm{CCS'}_1}. \tag{4.78}$$

Since in DTIM separations N_{diff} is the same for all ions within the same charge state, assuming a constant N across the whole ion mobility spectrum may be justified when diffusion is the dominant dispersion process, while the initial spread of the injected ion cloud is negligible. Thus, considering the separation of ions within a single charge state at V_{D} values well below the optimum, Eqs. 4.77 and 4.78 give a good estimate of P_{C}.

For separations utilizing the traveling wave technique, Eq. 4.78 can be modified according to Eq. 4.70 on page 87, using the notation $1/b = \gamma$:

$$P_{\mathrm{C,TWIMS},N} = 1 + \frac{\sqrt{N}}{4R_{\mathrm{S}}}\gamma \ln \frac{\mathrm{CCS'}_{\mathrm{n}}}{\mathrm{CCS'}_{1}}. \tag{4.79}$$

The above equation shows that, considering the same ratio of CCS' values and same constant N, $P_{\mathrm{C},N}$ is higher for TWIMS than for DTIMS by the factor γ. Practical values of γ normally fall in the range between 1.5 and 2.[184,185] Owing to the nonlinear dependence of t_{D} on the CCS', the separation window in TWIMS is broader relative to the temporal width of peaks than in an analogous DTIM separation. Consequently, the TWIM spectrum can encompass more resolved components, provided N is the same in the two IMS techniques.

The constant temporal peak width assumption. Let σ_{t} be constant across the whole separation window, meaning that $N(t_{\mathrm{D}}) = t_{\mathrm{D}}^2/\sigma_{\mathrm{t}}^2$ where σ_{t} is independent of t_{D}. In this case, the solution of Eq. 4.74 appears as

$$\begin{aligned} P_{\mathrm{C},\sigma} &= 1 + \frac{1}{4\sigma_{\mathrm{t}}R_{\mathrm{S}}} \int_{t_{\mathrm{D},1}}^{t_{\mathrm{D,n}}} \mathrm{d}t_{\mathrm{D}} \\ &= 1 + \frac{t_{\mathrm{D,n}} - t_{\mathrm{D},1}}{4\sigma_{\mathrm{t}}R_{\mathrm{S}}}. \end{aligned} \tag{4.80}$$

The subscript denotes that σ_{t} is constant. Alternatively, employing $\sigma_{\mathrm{t}} = t_{\mathrm{D},1}/\sqrt{N_1}$ where N_1 is the plate count for the first peak, Eq. 4.80 can be rewritten:

$$P_{\mathrm{C},\sigma} = 1 + \frac{\sqrt{N_1}}{4R_{\mathrm{S}}} \frac{t_{\mathrm{D,n}} - t_{\mathrm{D},1}}{t_{\mathrm{D},1}}. \tag{4.81}$$

The two equations above are analogous to those derived for gradient elution chromatography.[320,322]

From Eqs. 4.80 and 4.81 we can obtain equations specific for DTIM separations:

$$P_{\mathrm{C,DTIMS},\sigma} = 1 + \frac{\sqrt{N_1}}{4R_{\mathrm{S}}} \frac{K_1 - K_{\mathrm{n}}}{K_{\mathrm{n}}}, \tag{4.82}$$

$$P_{\mathrm{C,DTIMS},\sigma} = 1 + \frac{\sqrt{N_1}}{4R_\mathrm{S}} \frac{\mathrm{CCS'_n} - \mathrm{CCS'_1}}{\mathrm{CCS'_1}}. \tag{4.83}$$

Because t_inj is the same for all ions within a single separation, the constant peak width assumption is valid when σ_t is determined predominantly by the injection pulse, while diffusional broadening is a minor effect in comparison. Such situations arise well above $V_\mathrm{D,opt}$, in which cases Eqs. 4.82 and 4.84 can be applied.

Finally, for TWIM separations the respective semi-empirical equation adopts the following form:

$$P_{\mathrm{C,TWIMS},\sigma} = 1 + \frac{\sqrt{N_1}}{4R_\mathrm{S}} \frac{(\mathrm{CCS'_n})^\gamma - (\mathrm{CCS'_1})^\gamma}{(\mathrm{CCS'_1})^\gamma}. \tag{4.84}$$

Thus, γ values exceeding 1 lead to an increase in $P_{\mathrm{C},\sigma}$.

4.4.3 An exact peak capacity equation

Although equations based on the constant N and the constant σ_t assumptions are certainly helpful, their value lies mainly in their simplicity. Assuming constant N may be justified when diffusion determines σ_t, while the constant temporal peak width assumption can be applied if the contribution of the injection pulse dominates. In practice, however, the contributions of these two sources are generally comparable, especially under conditions where N and R_P are expected to be highest. As such, the above P_C equations have limited applicability in the experimentally most relevant cases.

To overcome these limitations and derive an exact, universally applicable P_C equation for DTIMS, a suitable physical model of zone broadening needs to be considered (see Section 4.2). The two major contributors to the total variance in DTIMS are diffusion and the injection pulse-width. Instead of summing spatial variances as in Section 4.2.3, let us use here their temporal equivalents:

$$\begin{aligned}
\sigma_{\mathrm{t,DTIMS}}(t_\mathrm{D}) &= \sqrt{\sigma^2_{\mathrm{t,inj}} + \sigma^2_{\mathrm{t,diff}}(t_\mathrm{D})} \\
&= \sqrt{\sigma^2_{\mathrm{t,inj}} + t^2_\mathrm{D} \frac{2k_\mathrm{B}T}{qV_\mathrm{D}}} \\
&= \sqrt{\sigma^2_{\mathrm{t,inj}} + \frac{t^2_\mathrm{D}}{N_\mathrm{diff}}}.
\end{aligned} \tag{4.85}$$

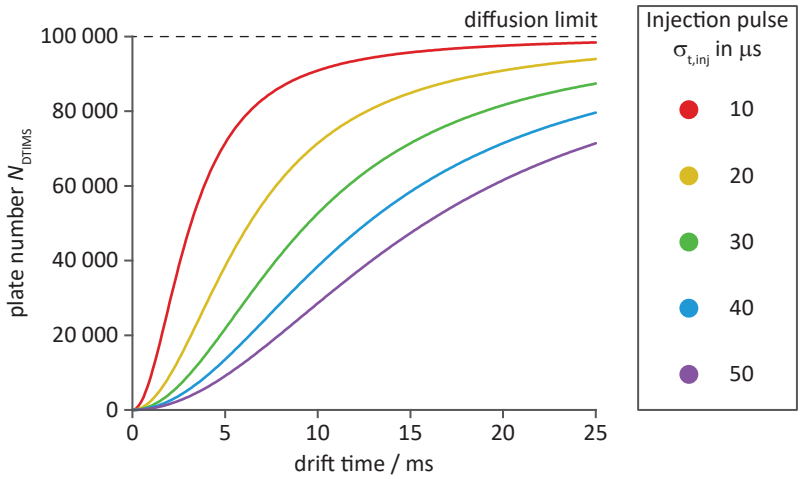

Figure 4.14: Systematic variation of the plate number across a drift tube ion mobility spectrum. Considering the finite width of the injection pulse and subsequent diffusional broadening of the ion packets (injection–diffusion model), N_{DTIMS} appears different for each peak within a single separation at fixed V_{D}. N_{DTIMS} for a given analyte depends on its t_{D}, which is inversely proportional to the ion's mobility. The calculations rely on the assumption that all ions have the same charge. The diffusion limit of theoretical plates N_{diff} was set at 100 000 (black dashed line), corresponding to $V_{\mathrm{D}} = 5.14\,\mathrm{kV}$ for singly charged species at room temperature. Each color-coded curve represents a different $\sigma_{\mathrm{t,inj}}$ value. At extremely short t_{D} the functions bear little practical relevance and should be interpreted carefully. For ions with very high K the reduced field will inevitably exceed the low-field limit.

From Eq. 4.85, N_{DTIMS} can be readily obtained:

$$N_{\mathrm{DTIMS}}(t_{\mathrm{D}}) = \frac{t_{\mathrm{D}}^2}{\sigma_{\mathrm{t,inj}}^2 + \frac{t_{\mathrm{D}}^2}{N_{\mathrm{diff}}}}. \tag{4.86}$$

The above formula is equivalent to Eq. 4.46 on page 60, where N_{DTIMS} was expressed with spatial rather than temporal quantities. Because q is the only analyte-specific parameter influencing N_{diff}, Eqs. 4.85 and 4.86 adequately describe the systematic variation of σ_{t} and N_{DTIMS} with t_{D} for a set of ions in an ion mobility spectrum, provided the ions are in the same charge state. Due to their relatively small contribution, space charge effects were not considered. Figure 4.14 shows graphically the aforementioned systematic dependence of N_{DTIMS} on t_{D} according to the injection–diffusion model of peak broadening. In other words, the figure reflects the dependence of N_{DTIMS} on the ions' varying K values in a single separation, with V_{D} and N_{diff} being constant.

Upon substituting Eq. 4.85 into Eq. 4.74 or Eq. 4.86 into Eq. 4.75 on

page 89, we obtain

$$P_{\mathrm{C,DTIMS}} = 1 + \frac{1}{4R_{\mathrm{S}}} \int_{t_{\mathrm{D,1}}}^{t_{\mathrm{D,n}}} \frac{\mathrm{d}t_{\mathrm{D}}}{\sqrt{\sigma_{\mathrm{t,inj}}^2 + \frac{t_{\mathrm{D}}^2}{N_{\mathrm{diff}}}}}. \tag{4.87}$$

The solution of Eq. 4.87 can be traced back to the following basic integral:[323]

$$\begin{aligned} \int \frac{\mathrm{d}x}{\sqrt{1+x^2}} &= \operatorname{arsinh}(x) \\ &= \ln\Big(x + \sqrt{x^2+1}\Big), \end{aligned} \tag{4.88}$$

where arsinh is the inverse hyperbolic sine function. For brevity, the constant of integration was omitted. Using the above integral, the solution of Eq. 4.87 gives the following closed-form expression:

$$P_{\mathrm{C,DTIMS}} = 1 + \frac{\sqrt{N_{\mathrm{diff}}}}{4R_{\mathrm{S}}} \ln \frac{t_{\mathrm{D,n}} + \sqrt{t_{\mathrm{D,n}}^2 + N_{\mathrm{diff}}\,\sigma_{\mathrm{t,inj}}^2}}{t_{\mathrm{D,1}} + \sqrt{t_{\mathrm{D,1}}^2 + N_{\mathrm{diff}}\,\sigma_{\mathrm{t,inj}}^2}}, \tag{4.89}$$

which is an exact solution to the peak capacity problem in DTIMS, considering injection and longitudinal diffusional as sources of zone broadening. Owing to similarities of the underlying mathematics, the above equation is similar to the peak capacity equation in chromatography in case extra-column band broadening is taken into account.[324] A detailed, step-by-step derivation of Eq. 4.89 is presented in Appendix C.

As a verification of Eq. 4.89, let us examine its behavior at limiting cases. If $\sigma_{\mathrm{t,inj}}$ is assumed to be zero (infinitesimally short injection), Eq. 4.89 becomes

$$P_{\mathrm{C,DTIMS,diff}} = 1 + \frac{\sqrt{N_{\mathrm{diff}}}}{4R_{\mathrm{S}}} \ln \frac{t_{\mathrm{D,n}}}{t_{\mathrm{D,1}}}. \tag{4.90}$$

The subscript indicates that only diffusional broadening was considered. The above equation is essentially the same as Eq. 4.76 on page 90, which was obtained by assuming constant N and may be applied when diffusion determines the zone width. At the other extreme, $\sigma_{\mathrm{t,diff}}$ is negligibly small compared to $\sigma_{\mathrm{t,inj}}$. In this case, employing the Maclaurin series of $\operatorname{arsinh}(x)$, Eq. 4.89 adopts the following form:

$$\begin{aligned} P_{\mathrm{C,DTIMS,inj}} &= 1 + \frac{t_{\mathrm{D,n}} - t_{\mathrm{D,1}}}{4\sigma_{\mathrm{t,inj}} R_{\mathrm{S}}} \\ &= 1 + \frac{\sqrt{N_{\mathrm{inj,1}}}}{4R_{\mathrm{S}}} \frac{t_{\mathrm{D,n}} - t_{\mathrm{D,1}}}{t_{\mathrm{D,1}}}. \end{aligned} \tag{4.91}$$

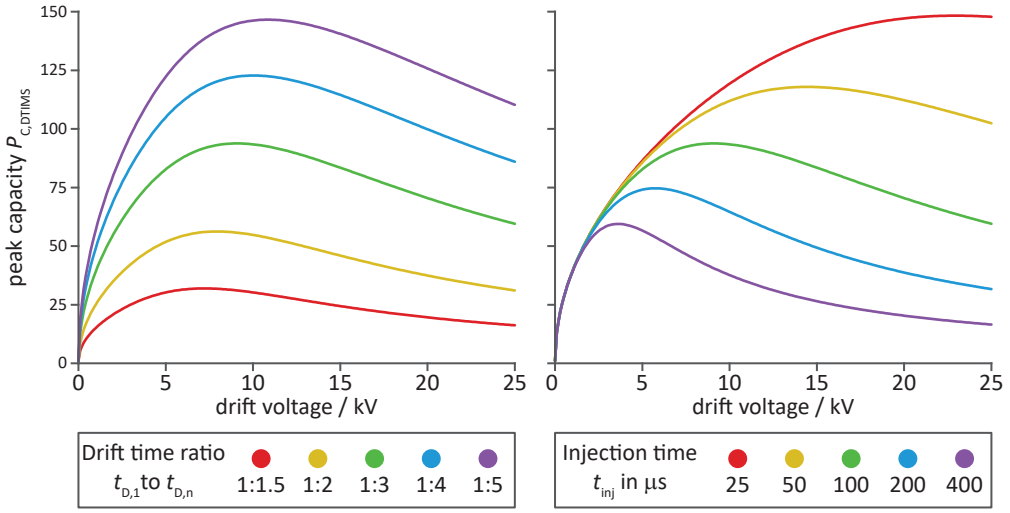

Figure 4.15: Peak capacity in drift tube ion mobility spectrometry based on the injection–diffusion model of zone broadening. $P_{C,DTIMS}$ was calculated according to Eq. 4.89 and depicted as a function of V_D. (left) Curves are color-coded according to the drift time ratio between the first and the last peak. Here, t_{inj} was fixed at 100 µs. (right) Colors encode different t_{inj} values, varied from 25 µs to 400 µs, forming an equirational progression. The drift time ratio was chosen to be 1:3. The two green curves in the two plots are thus identical. Calculations on both panels mimic real-life DTIMS experiments, performed at 293.15 K in a 150 mm long drift cell using N_2 or air as buffer gas at atmospheric pressure. Ions were assumed to be singly charged and R_S was chosen to be 1 (unit resolution). The mobility of the first species was fixed at $2.5 \times 10^4\,m^2\,V^{-1}\,s^{-1}$, the mobility of the last species was changed according to the defined drift time ratio.

Details of the series expansion can be found in Appendix C. The subscript reflects that the peak width is determined solely by the injection pulse. $N_{inj,1}$ is the plate count for the first peak, defined as $t_{D,1}^2/\sigma_{t,inj}^2$. The above equation appears equivalent to Eqs. 4.80 and 4.81 on page 91, which were obtained by assuming constant temporal peak width on the basis of negligible diffusional broadening. Thus, Eq. 4.89 successfully reproduces the two assumption-based equations when the respective assumptions are justified on the basis of a physical model.

Figure 4.15 explores peak capacity in DTIMS according to Eq. 4.89, highlighting the influence of the most important experimental parameters such as V_D or the injection time t_{inj}. The latter is the actual experimentally controlled duration of the injection pulse, and $\sigma_{t,inj}$ can be readily calculated using the relation $\sigma_{t,inj} = t_{inj}/\sqrt{12}$ assuming rectangular pulse profile. Calculations portrayed in Figure 4.15 mimic real-life DTIM separations, and K values were chosen to reflect atmospheric pressure experiments. In general, $P_{C,DTIMS}$ depends on several parameters in a complex manner as shown by

Eq. 4.89. For example, V_D affects both N_diff and t_D, and thus the impact of this parameter on $P_\mathrm{C,DTIMS}$ is double-edged. To make such influences more transparent, the most important trends are revealed here graphically. Based on the left-hand side of the figure it is evident that a broader separation window may encompass more peaks. In contrast to chromatography, however, the analyst has little control over this aspect of the separation in DTIMS. In principle, factors that efficiently increase N_DTIMS across the whole spectrum also lead to higher $P_\mathrm{C,DTIMS}$, such as employing shorter t_inj, shown on the right-hand side of Figure 4.15. Albeit less obvious, the influence of the buffer gas pressure is highly important. Higher p leads to lower absolute K values, manifesting in longer t_D without altering $\sigma_\mathrm{t,inj}$ or N_diff. Thus, raising p ultimately results in increased N_DTIMS and $P_\mathrm{C,DTIMS}$ values. Similarly to N_DTIMS, $P_\mathrm{C,DTIMS}$ reaches its maximum at an optimal V_D. The positions of these maxima along the abscissa fall between the V_D values where N_DTIMS for the first and last peak are highest (data not shown).

Being the solution of Eq. 4.87, we may view Eq. 4.89 as a formula accounting for the variation of N_DTIMS across the whole spectrum. When relying merely on single-peak-based measures of zone broadening, experimental conditions such as V_D, t_inj, and p are optimized considering arbitrarily chosen components of a mixture. The concept of peak capacity, on the other hand, enables us to optimize separations considering the whole set of analytes at the same time. Thus, it serves as a more comprehensive index of the separation performance, and a better guide for the analyst dealing with a large number of ions simultaneously.

4.5 The plate-height model in practice: an example of glycan analysis

Having addressed zone broadening, resolution, and peak capacity in DTIM separations from a predominantly theoretical point of view, herein we show how the plate-height model can be employed in everyday practice. In Section 4.3.3 we saw that the resolution between two peaks is related to δ_v, the relative velocity difference of the respective analytes. We interpreted δ_v as the measure of selectivity, and showed in Eq. 4.68 that it can be traced back to the relative CCS' difference of the two ions. Thus, Eq. 4.68 revealed the possibilities to influence selectivity in DTIMS, which is a key element of optimizing any separation.

In general, the most efficient way to enhance δ_v is to increase the CCS difference of the analytes. In low-field DTIM separations this is most often attempted by varying the composition of the buffer gas, or by influencing the three-dimensional structure of ions through adduct formation. An alternative strategy to influence selectivity is derivatization.[325,326] Fluorescent labels are widely employed in glycomic workflows and affect several aspects of such multidimensional analytical methods.[327,328] Besides enabling sensitive fluorescence detection and thereby straightforward quantification, labeling with fluorophores also influences the electrophoretic migration and chromatographic retention of glycans, as well as their ionization efficiency and rearrangement reactions in MS.[329–334] To fully exploit the potential of multidimensional HPLC-DTIM-MS glycomic workflows, it is important to evaluate also the impact of fluorescent labeling on the relative CCS difference of glycan isomers.

For this purpose, we chose the Lewis b (Le^b) and Lewis y (Le^y) fucosylated isomeric tetrasaccharides as model structures, which were analyzed following different sample preparation procedures: as native glycans, as reduced species carrying an open-ring alditol at their reducing end, and following fluorescent labeling with 2-aminobenzoic acid (2-AA), 2-aminobenzamide (2-AB), or procainamide (PCA) *via* reductive amination (Figure 4.16). Thus, we obtained five different chemical compounds for each isomer. These compounds were electrosprayed in both positive and negative ion mode, giving rise to five different singly charged ions per "neutral": Li^+, Na^+, and K^+ adducts, as well as protonated and deprotonated species. DTIM-MS experiments were performed in He buffer gas on a modified Synapt G2-S HDMS instrument, equipped with a nESI source and an RF-confining drift cell (see Section 3.2). Mobilities were determined using the stepped-field approach, and the respective ${}^{DT}CCS_{He}$ values were derived according to the Mason–Schamp equation. Details of the sample preparation and experiments are addressed

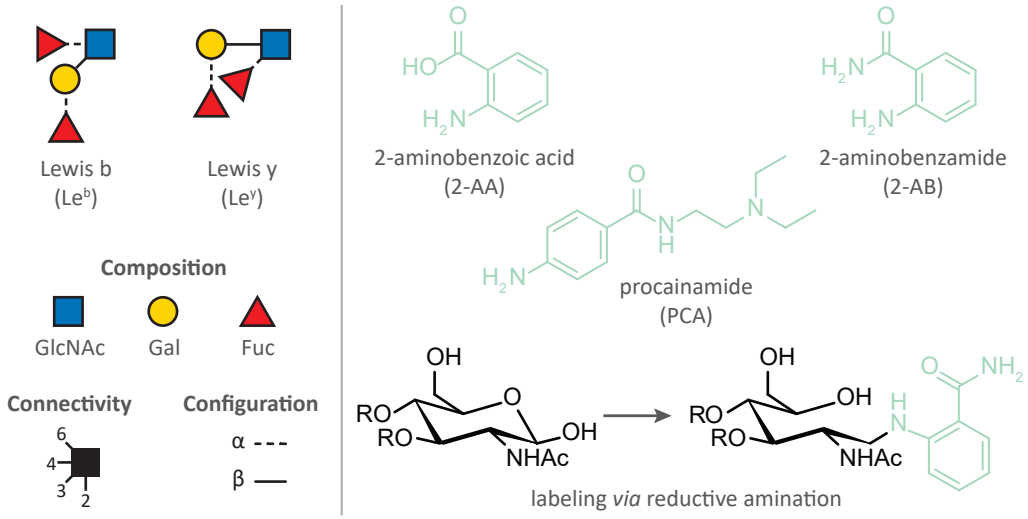

Figure 4.16: Overview of the glycan isomers and fluorescent labeling strategies employed in the study. (left) Structures of the fucosylated tetrasaccharides Lewis b and Lewis y, represented using the SNFG nomenclature. (right) Structures of the three fluorophores 2-aminobenzoic acid, 2-aminobenzamide, and procainamide. Labeling is performed *via* reductive amination, resulting in an open-ring GlcNAc alditol moiety at the reducing end of the glycans.

extensively in the respective publication (C. Manz, M. Grabarics, F. Hoberg, M. Pugini, A. Stuckmann, W. B. Struwe, K. Pagel, *Analyst* **2019**, *144*, 5292–5298). Herein we confine ourselves to demonstrating the utility of the plate-height model with respect to selectivity and resolution, employing the above described set of glycans as representative example.

Considering the Le^b/Le^y pair, the combination of five different derivatization strategies with five different approaches to generate molecular ions using nESI resulted in 50 intact singly charged species and 50 unique ${}^{DT}CCS_{He}$ values. Thus, we obtained 25 pairs of isomeric ions, each pair with a characteristic relative ${}^{DT}CCS_{He}$ difference. This dataset can be readily represented as a 5×5 matrix, highlighted at the top of Figure 4.17. Interestingly, the highest selectivity was observed for alkali metal adducts derivatized with 2-AB and 2-AA. For the respective protonated and deprotonated species, as well as for native and reduced compounds, the relative ${}^{DT}CCS_{He}$ difference was significantly lower. Although essential for the prediction of resolution between isomers, this information alone does not reflect the separation efficiency. The link between the CCS difference and R_S is the plate count (see Eq. 4.69 on page 84). As shown at the bottom of Figure 4.17, $N_{avg} = 25\,000$ (corresponding to $R_{P,avg} = 67$) would lead to fully resolved peak pairs ($R_S \geq 1.5$) in

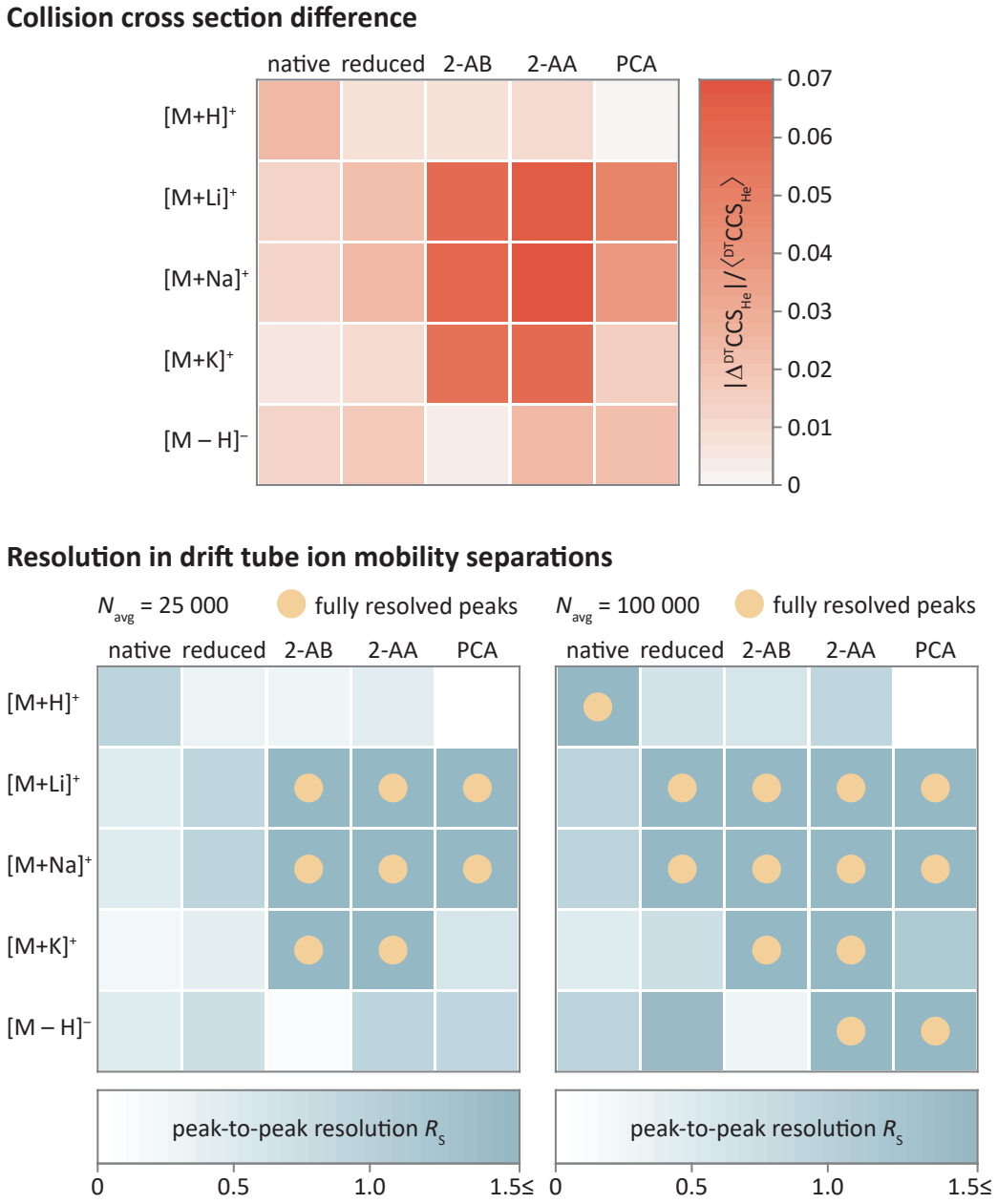

Figure 4.17: (top) Collision cross section difference and (bottom) resolution between Lewis b and Lewis y isomers, influenced by different derivatization strategies and (de)protonation/adduct formation. R_S values were calculated according to Eq. 4.69, assuming 25 000 and 100 000 theoretical plates as indicated. Fully resolved peaks with $R_S \geq 1.5$ are marked with a yellow dot. For simplicity, R_S values above the baseline resolution limit are not distinguished in the graphic.

eight cases. When raising N_{avg} to 100 000 ($R_{\mathrm{P,avg}} = 134$), complete separation would become possible in five additional instances. While $N_{\mathrm{avg}} = 25\,000$ can be considered representative for today's low-pressure DTIM-MS instruments, $N_{\mathrm{avg}} = 100\,000$ may be achieved with high-resolution DTIMS devices operated at atmospheric pressure. To date, the highest reported values in DTIMS are on the order of 300 000 theoretical plates[175], meaning that isomers with a relative CCS difference of 0.01 could be baseline resolved.

As demonstrated on the example of fluorescently labeled glycans, one may efficiently influence selectivity in DTIMS through derivatization and metal ion adduction. Because the impact of the aforementioned factors on the CCS values is rather unpredictable, the strategy today is mainly empirical. However, further progress in electronic structure calculations, improved methods to sample the vast conformational space of glycan ions *in vacuo*, and advanced computational tools for calculating collision integrals may eventually make computational chemistry a viable guide of the analyst, helping to optimize DTIM separations in practice.

4.6 Conclusions

Building on shared characteristics of differential migration methods but considering specific physical laws governing gaseous ion transport, Chapter 4 introduced a plate-height model for ion mobility separations. Through this model we explored zone broadening, resolution, and peak capacity in detail, thereby providing a framework to evaluate the efficiency of ion mobility separations and compare it to other separation methods.

We started by describing zone broadening as the consequence of independently acting dispersion processes (Section 4.2.2), and used these findings to construct plate-height equations in analogy to those in chromatography (Section 4.2.3). The accuracy of these equations was successfully verified by comparison with experiments (Section 4.2.4), which encouraged us to explore the model through a series of calculations, revealing the influence of key experimental parameters on zone broadening and resolving power (Section 4.2.5).

While the single-peak-based measures of plate height and resolving power are highly useful, in practice the analyst is more concerned about the actual resolution between peaks. In relation to peak-to-peak resolution, existing chromatography-influenced equations for DTIMS were critically evaluated and refined (Section 4.3.2). We also derived resolution equations from first principles that directly link selectivity and the relative velocity difference of zones to the transport properties and the CCS of ions (Section 4.3.3). Through revealing key factors influencing resolution, these predictive formulae may significantly benefit method optimization in everyday practice. Using a semi-empirical approach, equations obtained for linear DTIM separations could be also extended to separations utilizing traveling potential waves (Section 4.3.4).

In a journey starting from a single selected peak and moving towards an ever-increasing number of components, we finally arrived at the notion of peak capacity. Based on the constant plate count and constant temporal peak width assumptions, simple peak capacity equations were obtained for DTIM and TWIM separations (Section 4.4.2). In addition, considering the injection–diffusion model of peak broadening, an exact peak capacity equation could be derived for DTIMS (Section 4.4.3). These equations may prove especially fruitful in applications utilizing stand-alone IMS without MS analysis, and in general when extremely complex samples need to be analyzed. Besides enabling the calculation and optimization of peak capacity within a single ion mobility separation, the equations will also help to estimate the overall peak capacity in multidimensional workflows incorporating ion mobility separations.

Finally, the utility of the model was demonstrated through a practical

example: the prediction of resolution based on differences in the CCS of fluorescently labeled glycan isomers. We hope the plate-height model described herein will serve as a small step towards integrating ion mobility separations into the unified language of separation science, and facilitate further progress in this exciting field of research.

Chapter 5

Cold-ion infrared spectroscopy of glycosaminoglycans

Glycosaminoglycans are a unique class of acidic carbohydrates with an ever-increasing list of biological functions and newly discovered binding partners. The scientific endeavor to unravel the underlying structure–function relationships, however, has been hindered by the lack of suitable analytical methods capable of deciphering the sequence of these complex glycans. In this chapter we demonstrate the potential of cold-ion infrared spectroscopy to expand the mass spectrometry-based glycomics toolbox and provide structural information on well-defined glycosaminoglycan oligosaccharides. In particular, we focus on the analysis of heparan sulfate stereoisomers that contain epimeric hexuronic acid building blocks. In addition to providing diagnostic vibrational fingerprints that enable the distinction of isomers with minute structural differences, the experiments also revealed intriguing structure–spectrum correlations, which may have promising implications for the structural assignment of unknown glycosaminoglycan sequences in the future.

Chapter 5 is based on the following publications:

M. Lettow, M. Grabarics, E. Mucha, D. A. Thomas, L. Polewski, J. Freyse, J. Rademann, G. Meijer, G. von Helden, K. Pagel; IR action spectroscopy of glycosaminoglycan oligosaccharides, *Analytical and Bioanalytical Chemistry* **2020**, *412*, 533–537.

M. Lettow, M. Grabarics, K. Greis, E. Mucha, D. A. Thomas, P. Chopra, G.-J. Boons, R. Karlsson, J. E. Turnbull, G. Meijer, R. L. Miller, G. von Helden, K. Pagel; Cryogenic infrared spectroscopy reveals structural modularity in the vibrational fingerprints of heparan sulfate diastereomers, *Analytical Chemistry* **2020**, *92*, 10228–10232.

5.1 Glycosaminoglycan analysis in the gas phase

As discussed in Section 2.2, sulfated glycosaminglycans (GAGs) display remarkable structural complexity and represent an immense challenge for traditional glycan analysis methods. In contrast to the core proteins of proteoglycans that possess a well-defined primary structure, the GAG chains attached to a specific site of a certain core protein vary in length (polydispersity) as well as in the sequence of monomer units (microheterogeneity). These unique structural characteristics are direct consequences of their biosynthesis: sulfated GAGs may be actively remodeled during their assembly, as the final structure ensues from the collective action of an orchestra of enzymes, *e.g.* glycosyltransferases, sulfotransferases, and epimerases.[90,98,335]

While we may not be able to render a single well-defined sequence to these biopolymers, the arrangement of the repeating disaccharide units with different sulfation motifs and hexuronic acid stereochemistry is far from being random. For example, heparan sulfate (HS) chains display a characteristic domain structure, where highly sulfated NS (*i.e.* *N*-sulfated) regions are separated by mostly unmodified NA (*N*-acetylated) sections.[60] Today it is a widely-accepted notion that shorter protein-binding sequences along the polysaccharide chains are responsible for specific biological functions. The best-known example of a well-defined bioactive GAG sequence is the antithrombin III binding site of heparin, which contains a rare 3-*O*-sulfated glucosamine residue in the middle of a pentasaccharide segment.[97,336] The high specificity of this interaction and the strong structure–activity relationships have been successfully exploited for the development of fondaparinux, a fully synthetic heparin analogue anticoagulant.[337,338] Another specific interaction where 3-*O*-sulfation seems essential is the binding of the herpes simplex virus glycoprotein gD to HS chains on the host cell's surface, which facilitates viral attachment and entry.[97,339] While most GAG–protein interactions are less specific and do not involve such rare modifications as the two examples above, elucidating the structure of the participating bioactive GAG sequences is key to understanding the biological roles of these molecules, and has been in the center of GAG research.[69,85]

Determining the sequence of sulfated GAGs, however, turned out to be extremely challenging. Top-down sequencing of an entire HS polysaccharide chain is far beyond the capabilities of today's methods. Even shorter GAG oligosaccharides – obtained by partial depolymerization of longer chains or by chemical and (chemo)enzymatic synthesis – pose a formidable challenge to state-of-the-art analytical techniques. Synthetic oligosaccharides may only be

available in minute amounts, while those isolated from natural sources often occur as components of complex mixtures. Although MS-based techniques successfully cope with the two aforementioned challenges and therefore became the method of choice for GAG sequencing, conventional tandem MS with slow-heating ion activation methods often struggles to distinguish isomeric structures. In addition to containing potentially isomeric building blocks that may only differ in the position of sulfate groups or the configuration of a single stereocenter, sulfated GAG ions also display remarkable fragility in the gas phase, which impedes structural assignment.

Indeed, a major challenge in the MS-based analysis of highly sulfated species is the undesirable decomposition of sulfate modifications, appearing in the form of SO_3 neutral loss (79.96 Da).[340] Sulfate loss is an unimolecular reaction with a low activation barrier in the gas phase, hampering compositional analysis and the localization of sulfate modifications. As slow-heating methods such as CID and infrared multiphoton dissociation (IRMPD) favor fragmentation channels with the lowest barriers, sulfate loss products often dominate the respective product ion spectra. Being essentially a proton-catalyzed process, sulfate loss may be inhibited through deprotonating the respective sulfate groups. Exchanging the neutralizing proton to an aprotic tetraalkylammonium/metal cation is a common strategy to reduce intramolecular Coulomb repulsion between charged moieties, thereby facilitating deprotonation in densely sulfated species, as highlighted in Figure 5.1.

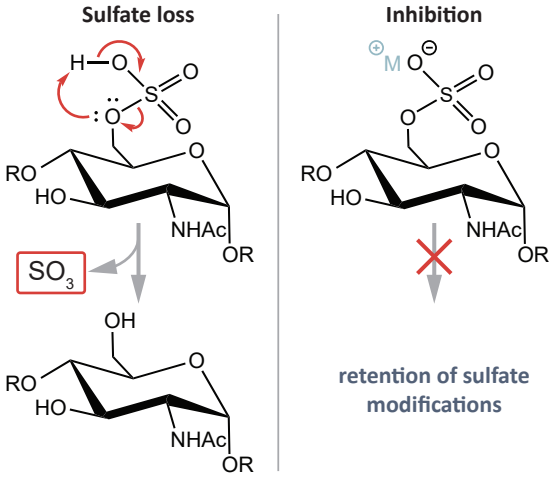

Figure 5.1: Sulfate equivalent loss of glycosaminoglycans in the gas phase. (left) Sulfate loss in the form of neutral SO_3 upon ion heating. Protonated sites are more prone to undergo decomposition. (left) Deprotonation of sulfate groups inhibits the reaction. Quaternary ammonium or metal ions (M^+) may neutralize the charge of deprotonated sulfate groups, reducing intramolecular Coulomb repulsion and facilitating the removal of protons.

In recent years, three distinct solutions emerged to tackle the above-mentioned challenges in MS-based GAG analysis, to facilitate the distinction of isomers, and provide structural information on the underlying GAG sequence. First, innovative fragmentation techniques such as ultraviolet photodissociation (UVPD) or electron-mediated dissociation (ExD) methods successfully overcame the main shortcomings associated with CID and IRMPD, *i.e.* the loss of sulfates and the lack of diagnostic cross-ring fragments. In contrast to slow-heating activation methods that induce fragmentation by gradual vibrational excitation, UVPD and ExD provide rapid energy deposition in a single step. Upon collision with energetic (typically 15–30 eV) electrons or absorption of UV photons, GAG ions undergo electronic excitation and electron detachment, which initiates alternative, radical-driven dissociation pathways. The resulting extensive glycosidic cleavages provide high sequence coverage, while informative cross-ring fragments help to determine the position of sulfate modifications within monomer units.[341–347] In addition, labile sulfate groups are largely retained. Although in certain cases product ion spectra also allowed for the distinction of GAG stereoisomers, ExD and UVPD MS are generally more efficient in localizing sulfate modifications than providing stereochemical information on hexuronic acid residues.[348–351]

While MS alone is restricted to counting ions with different m/z ratios, coupling it to IMS results in a powerful hyphenated technique that is directly sensitive to the three-dimensional structure of ions. In case of GAGs, this capability of IM-MS has been successfully exploited to separate diastereomers differing only in hexuronic acid stereochemistry.[352–355] Recently, a fragment-based shotgun DTIM-MS sequencing workflow was developed to determine the structure of HS oligosaccharides.[356] The method is based on comparing m/z and CCS values of unknown intact and fragment ions with those of known structures in a comprehensive library, and thus it is mainly limited by IMS resolving power and the accuracy of the aforementioned values.

Finally, the MS-based GAG analysis toolbox has recently been expanded with IR action spectroscopy on mass-selected ions. The first experiments were performed on small mono- and disaccharides, employing IRMPD and messenger-tagging spectroscopy.[357–360] Although hexuronic acid epimers as monosaccharides could be distinguished based on their IRMPD spectra between 2700 and 3700 cm^{-1} despite limited spectral resolution, and messenger-tagging spectroscopy at cryogenic temperatures revealed diagnostic absorption features in the OH stretch region for isomeric disaccharides with different sulfation motifs, GAG sequencing workflows may significantly benefit from spectroscopic information on larger oligosaccharides. Mono- and disaccharides do not provide sufficient sequence overlap, and disaccharides resulting from lyase-mediated depolymerization contain only a single $\Delta^{4,5}$-unsaturated

hexuronic acid at the reducing end, *i.e.* no intact uronic acid residues where the essential stereochemical information is preserved.

To overcome these limitations, we set out to perform a series of systematic experiments on GAG tetrasaccharides using cold-ion IR spectroscopy. The model compounds represent different GAG families, contain intact hexuronic acid building blocks, exhibit varying degrees of sulfation, and are comparable in size to the smallest GAG oligosaccharides performing specific biological functions. To the best of our knowledge, these are the first spectroscopic experiments on multiply charged anions embedded in He droplets.

5.2 Spectroscopy of hyaluronan tetrasaccharides in helium droplets

To evaluate the capabilities of cold-ion IR spectroscopy for the structural characterization of GAG oligosaccharides, a systematic set of model compounds with well-defined structures proved indispensable. However, as the chemical and (chemo)enzymatic synthesis of GAG oligosaccharides is extremely challenging and still subject of fundamental research,[361–370] the accessibility of well-defined synthetic standards is not comparable to that found in the fields of peptide and nucleic acid research. Thus, synthetic GAG oligosaccharides were obtained from expert academic research groups. The two hyaluronan (HA) tetrasaccharides highlighted in 5.2 were kindly provided by Prof. Jörg Rademann (Freie Universität Berlin, Berlin, Germany).[371] The reducing end azido groups – fixed in β-anomeric configuration – result from chemoenzymatic synthesis and allow for azide–alkyne coupling reactions for binding assays. The two compounds share the same glycan core and differ only in their degree of sulfation: the nonsulfated tetrahyaluronan (HA_4) mimics a native dp4 fragment, while the doubly sulfated analogue (sHA_4) carries a sulfate modification in the 6-*O*-positionon of each of the two GlcNAc residues. Although HA does not carry sulfate modifications in its native form, sulfated derivatives have been the subject of active research in recent years with the aim of tailoring GAG–protein interactions, studying structure–activity relationships, and developing GAG-based molecules and materials for therapeutic purposes.

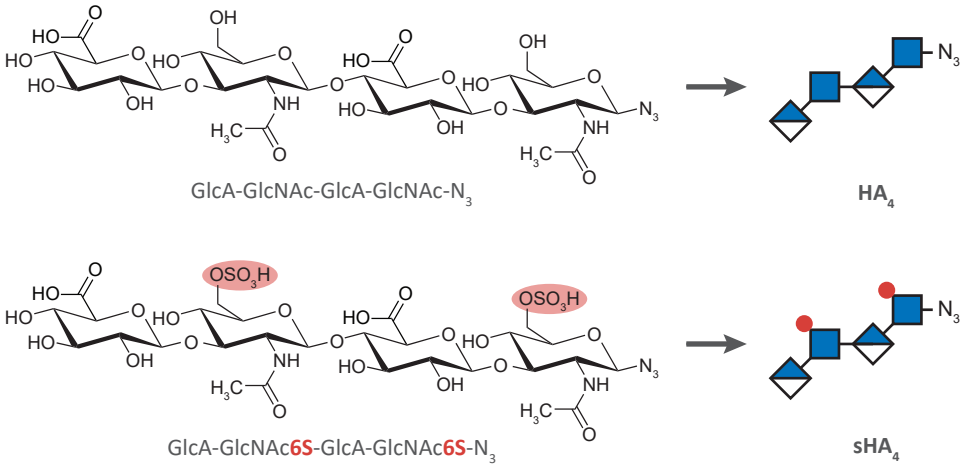

Figure 5.2: Synthetic hyaluronan model compounds with well-defined structures. (top) Nonsulfated tetrasaccharide (HA_4) and (bottom) its doubly sulfated analogue (sHA_4) with identical glycan backbone. The molecules are azide-functionalized at their reducing end.

Owing to their acidic functional groups, the HA tetrasaccharides display high ionization efficiency upon nESI in negative ion mode. To avoid the simultaneous presence of different deprotonation site isomers in the ion trap, as well as potential charge migration due to rapid proton exchange between sites of comparable gas-phase basicity[372] (two phenomena that may unnecessarily complicate the recorded IR spectra), the glycans were analyzed as doubly deprotonated species. Thus, the number of negative charges equaled that of carboxylates in case of HA_4, and that of sulfates in case of sHA_4. Due to differences in the respective proton affinities, it is rather unlikely that a negatively charged sulfate group in $[sHA_4 - 2H]^{2-}$ would abstract a proton from a neutral carboxyl.

Cold-ion IR spectra were recorded in the fingerprint region between 1000 and 1800 cm^{-1}, and are highlighted in Figure 5.3. While the structural complexity of the tetrasaccharides impedes the computation of suitable structural candidates and corresponding IR spectra, the well-resolved spectral features allow for qualitative band assignment. In case of the $[HA_4 - 2H]^{2-}$ ion, the spectral region between 1000 and 1150 cm^{-1} is dominated by absorption features corresponding to C–C–C, C–C–O, and C–O–C skeletal vibrations of pyranose rings. Between 1150 and 1350 cm^{-1} the spectrum is largely empty,

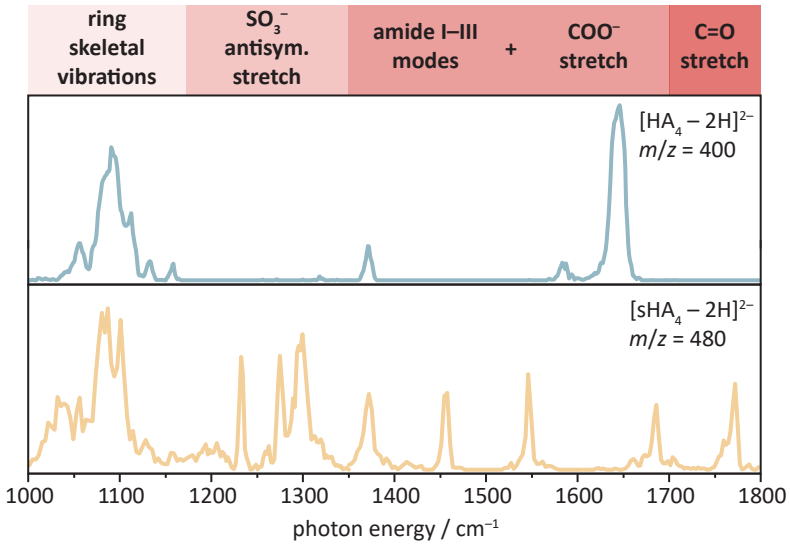

Figure 5.3: Cold-ion IR spectra of hyaluronan tetrasaccharide dianions in the fingerprint region. (top) Vibrational spectrum of doubly deprotonated HA_4 and (bottom) that of its doubly sulfated analogue, $[sHA_4 - 2H]^{2-}$. The various spectral regions highlighted above the IR spectra are designated based on the respective dominant vibrational modes. They are intended to serve as a practical guide rather than exact, quantitative rules for assignment. The depicted boundaries of the regions are not strictly defined and should be interpreted with care.

as no band corresponding to the symmetric stretch of the azido group is visible. The weak signals centered at 1372 and 1585 cm^{-1} can be attributed to the amide III and amide II vibrations of the GlcNAc residues, respectively. The strongest band at 1645 cm^{-1} results from the antisymmetric stretching vibration of the carboxylates, confirming the deprotonation of these functional groups. This intense peak likely overlaps with the amide I bands that mainly reflect C=O stretching of the acetylamino groups in GlcNAc units.

Considering the infrared spectrum of the doubly sulfated analogue $[sHA_4 - 2H]^{2-}$, the region dominated by skeletal vibrations may also encompass bands corresponding to the symmetric stretching mode of the deprotonated sulfate groups. However, without theoretical IR spectra, the exact origin of each spectral feature in this region cannot be determined. Between 1200 and 1350 cm^{-1}, in a region where the nonsulfated species lacks notable absorption features, intense bands appear that likely correspond to antisymmetric sulfate stretches. The amide III, amide II, and amide I bands appear at 1372, 1547, and 1685 cm^{-1}, respectively, while the peak at 1455 cm^{-1} may be attributed to the O–H bending mode of the neutral carboxyl groups. The feature with maximum at 1770 cm^{-1} can be assigned to the C=O stretch of neutral carboxyls. This observation – in combination with the absence of signals corresponding to the stretching modes of deprotonated carboxylates – also indicates that the negative charges are localized at the two sulfate groups.

In summary, cold-ion IR spectroscopy provides highly resolved vibrational spectra for mass-selected HA tetrasaccharide anions. Importantly, exciting the stretching vibrations of sulfate groups gives rise to well-resolved bands that appear in a spectral region largely devoid of other absorption features. The above findings demonstrate the potential of He droplet action spectroscopy for the structural characterization of GAG oligosaccharides, and provide motivation for more ambitious and exciting studies dealing with the analysis of isomers with minute structural differences.

5.3 Vibrational fingerprints of heparan sulfate stereoisomers

Following the first promising experiments on HA tetrasaccharides with varying degree of sulfation, we applied cold-ion IR spectroscopy to study GAG diastereomers that have identical mass and sulfation motifs but differ in their hexuronic acid stereochemistry. Opposed to HA and CS that contain exclusively β-D-glucuronic acid (GlcA), HS and heparin chains may also contain its $C5$ epimer, α-L-iduronic acid (IdoA). Together with differences in the position of sulfate modifications, this unique backbone diversity is responsible for the emergence of isomeric HS and heparin sequences, and as such, represents a major challenge for MS-based analytical methods.

To approach this analytical problem systematically, a set of four synthetic HS stereoisomers were chosen as model compounds, provided by Prof. Geert-Jan Boons (University of Georgia, Athens, United States and Utrecht University, Utrecht, The Netherlands). Highlighted in Figure 5.4, the tetrasaccharides contain two intact hexuronic acid residues and carry 6-O-sulfate modifications on their GlcNAc units. Being otherwise identical, the molecules differ only in their hexuronic acid building blocks (β-D-GlcA *vs.* α-L-IdoA). In this respect, they represent all possible variations with repetitions allowed ($2^2 = 4$ isomers). Each of the four molecules possesses 20 asymmetric carbons, and differs from the other three isomers in the configuration of merely one or two of these stereocenters. Not surprisingly, distinction and structural assignment of HS oligosaccharides with such minute structural differences is extremely challenging, even employing state-of-the-art tandem MS instrumentation with advanced ion activation methods optimized for GAGs.[350]

To obtain highly resolved vibrational fingerprints using cold-ion IR spectroscopy, the HS tetrasaccharides were studied as doubly deprotonated species. With the number of negative charges equal to the number of sulfate groups, the possibility of charge migration and the presence of multiple deprotomers could be minimized. IR spectra of the mass-selected and He-embedded ions were recorded in the fingerprint region between 1000 and 1800 cm^{-1}, and are shown in Figure 5.5. Despite the structural differences being extremely small, well-resolved absorption features and the unique combination of diagnostic bands allows for the unambiguous distinction of all four diastereomers. In addition to experimental and theoretical data reported in previous spectroscopic studies dealing with GAGs in solution or the gas phase,[359,373] the qualitative band assignment provided below is also supported by theoretical IR spectra calculated for structurally related disaccharides that represent fragments of

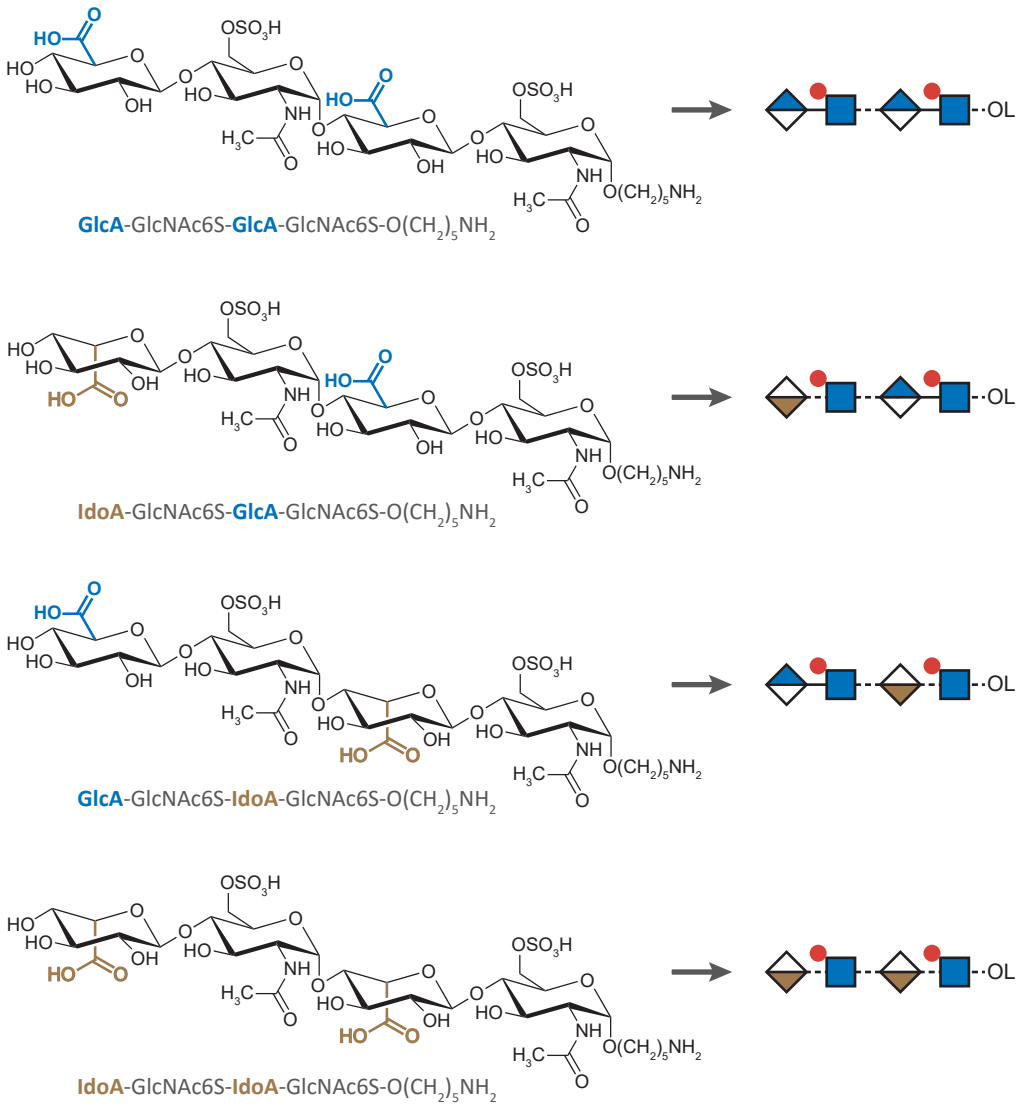

Figure 5.4: Synthetic heparan sulfate tetrasaccharides forming a systematic set of stereoisomers. Each isomer contains two hexuronic acid building blocks that may be either β-D-glucuronic acid or its $C5$ epimer, α-L-iduronic acid. Locked in α-anomeric configuration, the glycans carry an aminopentyl linker (abbreviated with L) at their reducing end, which is a remainder of the chemical synthesis.

the tetrasaccharides studied herein. The disaccharides and the calculations will be addressed in more detail at the end of this section.

As indicated in Figure 5.5, the spectra of the four HS stereoisomers between 1000 and 1150 cm^{-1} are dominated by absorption features corresponding to skeletal vibrations of the pyranose rings, which may also overlap with signals

arising from the symmetric sulfate stretches. Although these features are reproducible and clearly different for each isomer, spectral congestion may slightly limit their diagnostic potential. Importantly, well-resolved bands emerge between 1150 and 1350 cm^{-1}, which can be readily assigned to the antisymmetric stretching modes of the 6-*O*-sulfate groups. These bands appear in a unique combination for each diastereomer, enabling their unambiguous distinction. Less intense spectral features between 1200 and 1500 cm^{-1} can be attributed to various C–H and O–H bending modes. Amide bands stemming from mixed vibrations of the sulfated GlcNAc units' secondary amide groups are expected between 1500 and 1700 cm^{-1}. The weak absorption features above 1700 cm^{-1} can be attributed to the C=O stretching vibration of neutral carboxyl groups in the hexuronic acid residues.

In addition to recognizing the analytical utility of these well-resolved vibrational fingerprints, one may also observe surprisingly strong correlations between key structural elements of the analytes and the appearance of certain diagnostic bands. For example, a band centered around 1175 cm^{-1} (marked with an empty blue circle in Figure 5.5) appears in the spectra of the two isomers carrying a GlcA at their reducing end, while it is absent in the vibrational fingerprints of the other two species with an IdoA in the respective terminal position. In their case, the aforementioned band seems to be blue shifted to around 1220 cm^{-1} (empty brown circle). Based on this observation, we may tentatively assign the bands around 1175 and 1220 cm^{-1} to the antisymmetric stretching modes of sulfates on the internal GlcNAc6S adjacent to the nonreducing end GlcA and IdoA, respectively. An intense peak at 1295 cm^{-1} can be observed uniformly in the spectra of all four isomers, while the band at 1330 cm^{-1} and another intense spectral feature around 1600 cm^{-1} (both marked with a full brown circle) appear only in the spectra of the two species that contain an internal IdoA adjacent to the reducing end GlcNAc6S carrying the aminoalkyl linker.

The above observations indicate that the local chemical environments of the sulfate and amide groups in a given GlcNAc6S unit, and as such, the corresponding vibrational frequencies and band intensities are strongly influenced by the stereochemistry of the hexuronic acid that is attached to this GlcNAc6S in the 4-*O*-position. On the other hand, the same bands seem not to depend on whether the other hexuronic acid residue in the tetrasaccharide is GlcA or IdoA. For example, the antisymmetric sulfate stretching bands associated with the nonreducing end GlcA-GlcNAc6S and IdoA-GlcNAc6S disaccharide modules (signals marked with empty blue and empty brown circles) are largely unaffected by the stereochemistry of the internal hexuronic acid residue. Similarly, diagnostic spectral features associated with the reducing end IdoA-GlcNAc6S-OL disaccharide module with the aminopentyl linker

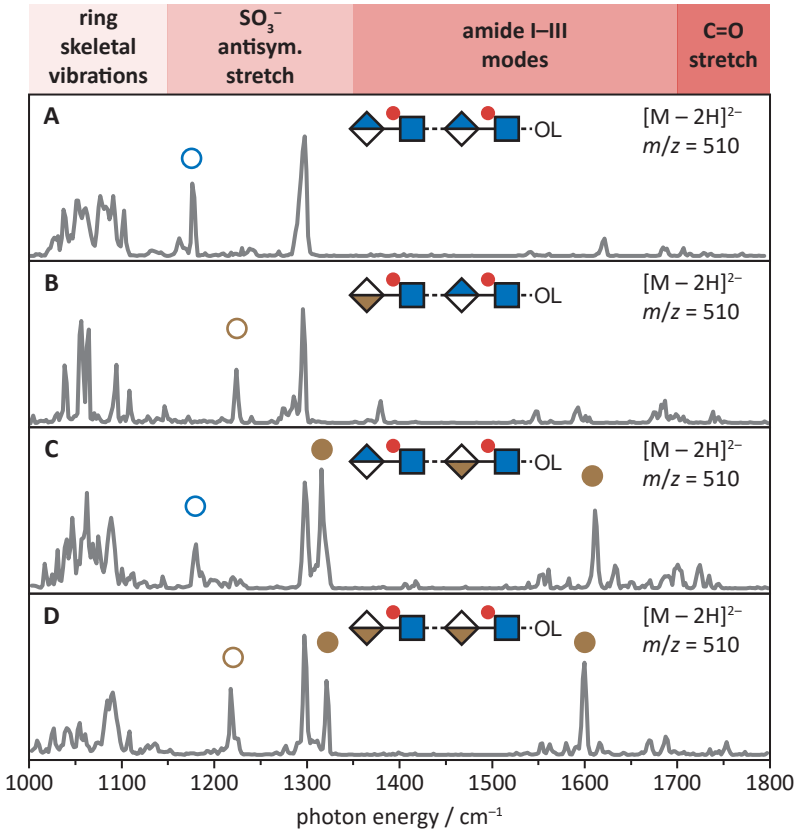

Figure 5.5: Vibrational fingerprints of doubly deprotonated HS tetrasaccharide ions between 1000 and 1800 cm^{-1}. Cold-ion IR spectroscopy reveals diagnostic absorption features, enabling unambiguous distinction of all four stereoisomers. Strong structure–spectrum relationships are apparent, the respective bands being indicated by color-coded symbols. Empty blue circles mark diagnostic features appearing in the spectra of the two glycans carrying GlcA at their nonreducing end. Empty brown circles indicate bands that appear only in the spectra of the respective isomers with a nonreducing end IdoA. Full brown circles mark signals that correlate with the presence of an internal IdoA residue adjacent to the reducing end GlcNAc6S. The aminopentyl linker is abbreviated with L. Characteristic spectral regions are highlighted above the IR spectra, serving as a simplified practical guide.

(bands marked with full brown circles) do not depend on the stereochemistry of the hexuronic acid on the nonreducing end. Thus, the hydrogen bonding networks of the discrete disaccharide modules in each tetrasaccharide seem to be independent of each another.

Unfortunately, the size and complexity of the doubly deprotonated HS tetrasaccharides make high-level calculations on these ions unfeasible. Therefore, to rationalize the experimental findings, a series of theoretical calculations were carried out on structurally related HS disaccharides as singly depro-

tonated species. The disaccharides carry either an aminopentyl linker or a methoxy group at their reducing end, both fixed in α-anomeric configuration. The following four disaccharide ions were subjected to theory: [GlcA-GlcNAc6S-OCH_3 – H]$^-$, [IdoA-GlcNAc6S-OCH_3 – H]$^-$, [GlcA-GlcNAc6S-$O(CH_2)_5NH_2$ – H]$^-$, and [IdoA-GlcNAc6S-$O(CH_2)_5NH_2$ – H]$^-$. The latter two species with the aminopentyl linker correspond to the discrete disaccharide modules on the reducing terminus of the tetrasaccharides, whereas the methyl glycosides mimic the respective disasaccharide modules on the nonreducing end of the parent tetrasaccharides. The calculations were performed by Kim Greis (Fritz Haber Institute and Freie Universität Berlin, Berlin, Germany). A brief description of the applied theoretical methods is given below.

For sampling the conformational space of the disaccharide anions, the FAFOOM[374] (flexible algorithm for optimization of molecules) genetic algorithm was employed with local optimization using density functional theory in the FHI-aims[375] external software. The structures were screened for interactions between their carboxyl, amide, sulfate, and (in presence of a linker) amino functional groups with relevant interatomic distances below 2 Å. Low-energy conformers with distinct intramolecular interaction motifs were reoptimized at the PBE0-D3/6-31G(d)[376,377] level of theory. For sulfur alone, the larger 6-311+G(2df,2pd) basis set was employed. Finally, the lowest-energy structure for each of the four disaccharides was reoptimized and vibrational frequencies were computed at the PBE0-D3/ma-def2-TZVP[378,379] level of theory. The lowest-energy structures and the corresponding theoretical

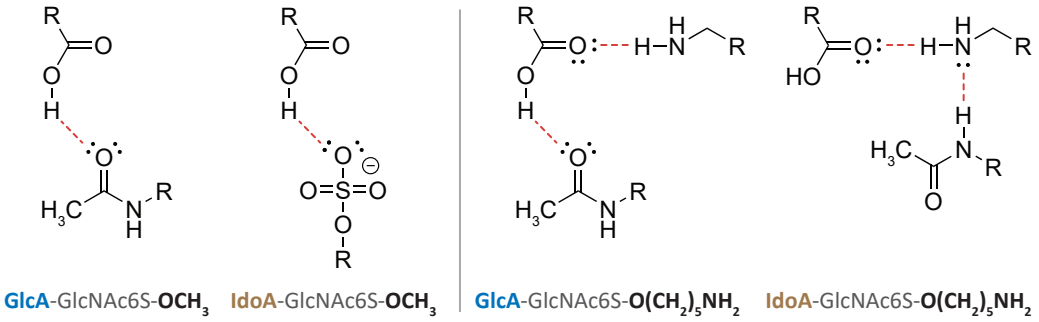

Figure 5.6: Hydrogen bonding motifs in the lowest-energy structures of singly deprotonated heparan sulfate disaccharides, representing the four distinct disaccharide modules of the tetrasaccharide stereoisomers. (left) Hydrogen bonding pattern of disaccharides with a methoxy group at their reducing end. (right) Interactions in disaccharides carrying an aminopentyl linker. Figure adapted with permission from M. Lettow, M. Grabarics, K. Greis, E. Mucha, D. A. Thomas, P. Chopra, G.-J. Boons, R. Karlsson, J. E. Turnbull, G. Meijer, R. L. Miller, G. von Helden, K. Pagel, *Analytical Chemistry* **2020**, *92*, 10228–10232. Copyright 2020 American Chemical Society.

IR spectra are shown in Appendix D.

The lowest-energy structures of the four disaccharides exhibit distinct interaction motifs that are clearly different from each other. Differences in these intramolecular hydrogen bonding patterns, highlighted schematically in Figure 5.6, provide a rational behind the experimental results and observed spectral differences. In case of $[\text{GlcA-GlcNAc6S-OCH}_3 - \text{H}]^-$, a hydrogen bond is established between the carbonyl oxygen of the GlcNAc6S unit's amide group and the hydrogen at the GlcA residue's neutral carboxyl group. Its epimer, $[\text{IdoA-GlcNAc6S-OCH}_3 - \text{H}]^-$, displays a different hydrogen bonding pattern where the neutral carboxyl forms an ionic hydrogen bond with the negatively charged sulfate group instead. Considering the disaccharides with the aminopentyl linker, it is apparent that the amino group of the linker strongly influences the intramolecular hydrogen bonding networks. In case of $[\text{GlcA-GlcNAc6S-O(CH}_2)_5\text{NH}_2 - \text{H}]^-$ it serves as a hydrogen bond donor to the carbonyl oxygen of the neutral carboxyl, while in case of $[\text{IdoA-GlcNAc6S-O(CH}_2)_5\text{NH}_2 - \text{H}]^-$ the linker participates in the network as both donor and acceptor, establishing a hydrogen bond with the neighboring amide group as well.

In summary, cold-ion IR spectroscopy provides highly resolved spectra for moderately sulfated HS tetrasaccharides, allowing for the unambiguous distinction of diastereomers differing only in their hexuronic acid stereochemistry. Diagnostic amide I and sulfate stretching bands appear in a unique combination for each isomer, and their appearance in the spectra seem to be directly linked to the presence of well-defined structural elements. To provide a rational behind experimental observations, calculations were performed on structurally related disaccharide anions, employing a strategy that merges a genetic algorithm with first-principles density functional calculations. Finally, we should recognize the importance and analytical potential of the strong structure–spectrum correlations observed herein. While the distinction of isomers with minute structural differences is an important aspect of glycomics, the ultimate goal of glycan analysis may be the *de novo* sequencing of molecules with unknown structures. Based on the above results, it is tempting to envisage an analytical method where the appearance of diagnostic spectral bands can serve as an indicator for the presence of certain structural features in GAGs. Testing this hypothesis, however, requires spectroscopic data on a much larger pool of GAG oligosaccharides that display a wide variety of different structural elements. Obtaining such information is the subject of ongoing research, and the potential benefits of expanding the MS-based GAG analysis toolbox with IR spectroscopy on mass-selected ions will certainly motivate further studies in this direction.

5.4 Conclusions

In summary, the above findings demonstrate the utility of cold-ion IR spectroscopy for the structural analysis of GAG oligosaccharides. By employing the He droplet action spectroscopy scheme in combination with the Fritz Haber Institute Free-Electron Laser, highly resolved infrared spectra could be recorded for mass-selected HA and HS tetrasaccharides in the fingerprint region. Importantly, the antisymmetric sulfate stretching bands appear in a spectral region where no other intense signal occurs, which decreases spectral congestion and improves the diagnostic potential of these absorption features. In addition, carboxylate and carboxyl stretching vibrations reveal information on charge localization, thereby guiding the analyst to select the optimal charge state, minimize the possibility of charge migration, and avoid the presence of multiple deprotomers in the experiments.

The unique combination of diagnostic spectral features in the vibrational fingerprints of HS stereoisomers allowed for the unambiguous distinction of these extremely similar structures. As hexuronic acid stereochemistry has a strong impact on the affinity and selectivity of GAG–protein interactions, cold-ion IR spectroscopy may prove to be a powerful tool for unraveling the structure–activity relationships of bioactive GAG sequences that contain different hexuronic acid epimers. Furthermore, the strong structure–spectrum correlations observed in the experiments provide motivation for further studies. Indeed, obtaining reference spectra for larger and more heavily sulfated GAG oligosaccharides, as well as isomeric species differing in the position of their sulfate modifications, is the subject of ongoing research at the Fritz Haber Institute.

Finally, we would like to comment on the immense possibilities that could be opened by implementing IR spectroscopy on mass-selected ions into existing MS-based GAG analysis workflows. One may envisage databases that contain m/z values together with vibrational fingerprints for well-defined GAG oligosaccharide ions. Besides using such databases for verifying the presence of known sequences in biological samples, it may be possible to sequence larger GAGs with unknown structures based on the characteristic IR fingerprints of their fragments, in a similar fashion as recently demonstrated for HS oligosaccharides using $^{\mathrm{DT}}\mathrm{CCS}_{\mathrm{He}}$ values.[356]

While an experimental setup utilizing superfluid He droplets and an IR free-electron laser will probably not serve as the prototype for affordable analytical devices, instruments that employ tunable benchtop laser systems and rely on alternative action spectroscopy schemes such as messenger-tagging may eventually find commercial applications. In addition to more affordable and easy-to-use instrumental solutions, for IR ion spectroscopy to become

a widespread analytical technique, the spectral acquisition rate needs to be significantly improved. A recently developed setup that employs N_2 tagging in a cryogenic multitrap and a continuous wave fiber-pumped IR laser enabled rapid acquisition of highly-resolved spectra for glycan ions.[380] Covering a spectral range of 450 cm^{-1}, IR spectra with well-resolved bands and sufficiently high signal-to-noise ratio were recorded within tens of seconds, which shall allow for the online coupling of IR ion spectroscopy to condensed-phase chromatographic and electrophoretic separations. With such giant steps of technological progress, IR spectroscopy of mass-selected ions might become a widespread technique for the analysis of GAGs and other glycans in the foreseeable future.

Chapter 6

Summary and outlook

In an attempt to expand the MS-based glycan analysis toolbox, this thesis explored novel analytical techniques for the separation and structural characterization of carbohydrate ions. Utilizing the concept of theoretical plates and an abstract mathematical framework adapted from chromatography, we developed a detailed analytical model for drift tube ion mobility separations. The model, rooted in physical laws governing separative and dispersive ion transport in gaseous media, addressed the three main aspects of zonal separations.

First, zone broadening was described as the result of independently acting dispersion processes, and suitable equations were derived for calculating plate heights, theoretical plates, and resolving power in ion mobility separations. The validity of the plate-height model was assessed through comparison with experiments, performed on a custom-built drift tube ion mobility-mass spectrometer, which allowed for control over key experimental parameters such as the buffer gas pressure or the injection pulse-width. Through incorporating the concept of selectivity and relative velocity difference, the model was successfully extended to describe resolution between neighboring peaks in ion mobility spectra. We presented a critical analysis of existing chromatography-influenced equations, and provided alternative solutions that overcome their limitations. In addition, we derived exact, predictive resolution equations for drift tube ion mobility separations from first principles, and a simple semi-empirical formula for separations utilizing the traveling wave technique. The third main aspect of ion mobility separations explored through the plate-height model was peak capacity. In addition to simple, approximate solutions, an exact peak capacity equation was derived based on the injection–diffusion model of peak broadening. These equations can be readily applied to improve separations dealing with highly complex samples and a large number of peaks, where concentrating on the width of an arbitrarily chosen zone or

on the resolution of a critical peak pair may not be adequate optimization strategies. The discussion of the plate-height model is completed with a study on fluorescently labeled glycans, demonstrating the utility of the model to aid the evaluation and optimization of ion mobility separations in everyday practice.

The plate-height model thus offers a comprehensive theoretical framework to evaluate, predict, and improve the efficiency of time-dispersive ion mobility separations, and to compare the performance of this technique with that of other separation methods such as chromatography or zone electrophoresis. In this sense, our work is aimed not only at researchers in the field of gas-phase ion chemistry, but also at the broader separation science community. With respect to future perspectives, an exact equation for traveling wave ion mobility spectrometry relating the average velocity of ions to their mobility and other potentially important properties may not only allow researchers to circumvent collision cross section calibration, but would also enable the development of an analytical model describing zone broadening in this technique. Furthermore, concepts established previously for various steady-state separation methods may be successfully applied to trapped ion mobility spectrometry, facilitating the progress of this powerful novel separation technique.[36,381–384]

In addition to presenting a plate-height model for ion mobility separations and the application of this model to glycan analysis, in this thesis we demonstrated the potential of cold-ion IR spectroscopy for the structural characterization of GAG oligosaccharides. Studying hyaluronan and heparan sulfate tetrasaccharides as deprotonated species, we obtained highly resolved IR spectra of mass-selected ions between 1000 and 1800 cm^{-1}. The optical fingerprints confirmed that negative charges are preferentially localized on sulfate groups, and that these sulfate groups give rise to diagnostic absorption features in a spectral region where no other notable signals occur. The unique combination of diagnostic sulfate stretches and amide bands allowed for the unambiguous identification of four heparan sulfate stereoisomers. These tetrasaccharides differ only in their hexuronic acid stereochemistry, and are extremely difficult if not impossible to distinguish using state-of-the-art tandem MS methods. Our experiments also revealed strong structure–spectrum relationships for the heparan sulfate isomers, as the appearance of certain diagnostic bands could be directly linked to the presence of well-defined structural elements and building blocks in the analytes. The experimental observations could be rationalized through quantum chemical calculations, which indicated pronounced differences between the intramolecular hydrogen bonding patterns of the four tetrasaccharide anions.

The above findings directly lead us to potential future developments. Vibrational spectroscopy of cryogenically cooled ions as a means to distinguish

and identify isomers in complex mixtures could significantly contribute to advancements in GAG research. With further progress in IR laser technology, spectroscopy on mass-selected ions may become possible using commercial instruments, enabling the integration of this technique into multidimensional GAG analysis workflows. To use vibrational fingerprints for the identification of analytes, however, suitable databases are required that compile spectroscopic data for a large number of species. Therefore, ongoing spectroscopic research at the Fritz Haber Institute and the Freie Universität Berlin is aimed at characterizing a more extensive set of heparan sulfate standards. The studied structures include disaccharides with different sulfation motifs, species carrying rare 3-*O*-sulfate modification, as well as densely sulfated oligosaccharides that mimic NS domains in heparan sulfate chains. These efforts, in combination with those of like-minded academic research groups focusing on other classes of glycans, may bring us closer to the long-standing goal of glycosciences to finally decipher the sugar code.

Appendix A

Calculating variance for simple distributions

In Section 4.2.2, Eq. 4.17, C_{inj} is introduced as a dimensionless constant of proportionality relating the temporal variance of the injected ion packet ($\sigma^2_{\mathrm{t,inj}}$) to the square of the pulse duration (t^2_{inj}). If the function describing the axial distribution of the ions is known, C_{inj} may be obtained using simple statistical methods.

Considering a continuous random variable x with a probability density function $f(x)$, the second central moment or variance can be calculated as

$$\mu_2 = \sigma^2 = \int_{-\infty}^{+\infty} (x-\mu)^2 f(x)\mathrm{d}x, \tag{A.1}$$

where μ is the population mean of the distribution. In relation to calculating C_{inj}, we consider four distributions that are all symmetric with respect to the mean: rectangular, quadratic, isosceles triangular, and the Gaussian distribution. Let us choose μ to be 0 for convenience and introduce the notation $t_{\mathrm{inj}} = 2a$. Thus, with the exception of the Gaussian distribution that will be discussed later, the lower and upper limit of the distributions appear at $-a$ and $+a$, respectively. As the probability density outside these limits is 0, we may readily calculate $\sigma^2_{\mathrm{t,inj}}$ by solving the following integral, where t denotes the independent variable:

$$\sigma^2_{\mathrm{t,inj}} = \int_{-a}^{+a} t^2 f(t)\mathrm{d}t. \tag{A.2}$$

Eq. A.2 relates $\sigma^2_{\mathrm{t,inj}}$ to the pulse duration $t_{\mathrm{inj}} = 2a$, which corresponds to the full temporal width of the injected ion packet.

Rectangular distribution. For a rectangular distribution with $\mu = 0$, the probability density function (PDF) appears as

$$f(t) = \begin{cases} \frac{1}{2a}, & \text{if } -a \leq t \leq +a \\ 0, & \text{if } t < -a \text{ or } +a < t. \end{cases} \tag{A.3}$$

Thus, $\sigma^2_{\mathrm{t,inj}}$ can be obtained from

$$\sigma^2_{\mathrm{t,inj}} = \int_{-a}^{+a} t^2 \frac{1}{2a} \mathrm{d}t. \tag{A.4}$$

The stepwise solution of Eq. A.4,

$$\begin{aligned} \sigma^2_{\mathrm{t,inj}} &= \int_{-a}^{+a} t^2 \frac{1}{2a} \mathrm{d}t \\ &= \left[\frac{t^3}{6a} \right]_{-a}^{+a} \\ &= \frac{a^2}{3} \\ &= \frac{t^2_{\mathrm{inj}}}{12}, \end{aligned} \tag{A.5}$$

finally yields the constant of proportionality when the axial distribution of ions in the injected packet follows a rectangular shape: $C_{\mathrm{inj}} = 12$.

Quadratic distribution. For a quadratic distribution with $\mu = 0$, the PDF can be written as

$$f(t) = \begin{cases} \frac{3}{4a^3}(a^2 - t^2), & \text{if } -a \leq t \leq +a \\ 0, & \text{if } t < -a \text{ or } +a < t, \end{cases} \tag{A.6}$$

from which we obtain:

$$\sigma^2_{\mathrm{t,inj}} = \frac{3}{4a^3} \int_{-a}^{+a} t^2 (a^2 - t^2) \mathrm{d}t. \tag{A.7}$$

Solving Eq. A.7,

$$\begin{aligned}\sigma^2_{\mathrm{t,inj}} &= \frac{3}{4a^3}\int_{-a}^{+a} t^2(a^2-t^2)\mathrm{d}t \\ &= \left[\frac{5t^3}{20a} - \frac{3t^5}{20a^3}\right]_{-a}^{+a} \\ &= \frac{a^2}{5} \\ &= \frac{t^2_{\mathrm{inj}}}{20}, \end{aligned} \tag{A.8}$$

thus yields $C_{\mathrm{inj}} = 20$ for quadratic ion distributions.

Symmetric triangular distribution. A symmetric triangular distribution with $\mu = 0$ may be defined by the following PDF:

$$f(t) = \begin{cases} \frac{a+t}{a^2}, & \text{if } -a \le t \le 0 \\ \frac{a-t}{a^2}, & \text{if } 0 < t \le +a \\ 0, & \text{if } t < -a \text{ or } +a < t. \end{cases} \tag{A.9}$$

For $-a \le t \le 0$ we can write:

$$\begin{aligned}\int_{-a}^{0} t^2\frac{a+t}{a^2}\mathrm{d}t &= \left[\frac{t^3}{3a} + \frac{t^4}{4a^2}\right]_{-a}^{0} \\ &= \frac{a^2}{3} - \frac{a^2}{4} \\ &= \frac{a^2}{12}. \end{aligned} \tag{A.10}$$

Analogously, for $0 < t \le +a$:

$$\begin{aligned}\int_{0}^{+a} t^2\frac{a-t}{a^2}\mathrm{d}t &= \left[\frac{t^3}{3a} - \frac{t^4}{4a^2}\right]_{0}^{+a} \\ &= \frac{a^2}{3} - \frac{a^2}{4} \\ &= \frac{a^2}{12}. \end{aligned} \tag{A.11}$$

By combining Eqs. A.10 and A.11 we obtain:

$$\begin{aligned}\sigma^2_{\mathrm{t,inj}} &= \frac{a^2}{6} \\ &= \frac{t^2_{\mathrm{inj}}}{24}.\end{aligned} \tag{A.12}$$

Thus, for symmetric triangular distributions $C_{\mathrm{inj}} = 24$.

Gaussian distribution. To calculate C_{inj} for a Gaussian distribution of ions, let us follow a different approach. The distance between the points where the tangents to the two inflection points of a Gaussian intercept the baseline is 4σ, the effective width of the distribution.[36] Employing this convention, for ion packets following a Gaussian distribution along the axial dimension $t_{\mathrm{inj}} = 4\sigma_{\mathrm{t,inj}}$, from which we obtain $C_{\mathrm{inj}} = 16$.

Appendix B

Derivation of resolution equations

Herein we provide detailed derivations for the predictive resolution equations appearing in Section 4.3. First, let us introduce two basic chromatographic definitions. The retention factor of the ith component, k_i, is defined as

$$k_\mathrm{i} = \frac{t_\mathrm{R,i} - t_0}{t_0}, \tag{B.1}$$

where $t_\mathrm{R,i}$ is the retention time of the ith component, while t_0 is the void time of the column.The numerator thus equals the time the solute spends in the stationary phase, while the denominator is the time spent in the mobile phase during the elution process. The separation factor for two components, α, is defined based on the retention factors of the solutes:

$$\alpha = \frac{k_2}{k_1}, \tag{B.2}$$

where $\alpha \geq 1$ by definition. For completeness, a few simple relations applied in the upcoming derivations are listed below:

$$t_\mathrm{R,i} = t_0(1 + k_\mathrm{i}), \tag{B.3}$$

$$\Delta t_\mathrm{R} = t_0 \Delta k, \tag{B.4}$$

$$1 + k_\mathrm{i} = \frac{t_\mathrm{R,i}}{t_0}, \tag{B.5}$$

$$\frac{k_\mathrm{i}}{1 + k_\mathrm{i}} = \frac{t_\mathrm{R,i} - t_0}{t_\mathrm{R,i}}. \tag{B.6}$$

Eq. B.6 represents the so-called chromatographic migration factor. Employing the concept of virtual migration distances it can be readily shown that the equivalent of this factor in DTIMS (an electrophotetic process in the absence of bulk flow) is equal to 1.[385] Additionally,

$$\begin{aligned} \alpha - 1 &= \frac{|\Delta t_{\mathrm{R}}|}{t_{\mathrm{R},1} - t_0} \\ &= \frac{|\Delta k|}{k_1}, \end{aligned} \tag{B.7}$$

$$\begin{aligned} \alpha + 1 &= \frac{t_{\mathrm{R},1} + t_{\mathrm{R},2} - 2t_0}{t_{\mathrm{R},1} - t_0} \\ &= \frac{k_1 + k_2}{k_1}, \end{aligned} \tag{B.8}$$

$$\begin{aligned} \frac{\alpha - 1}{\alpha} &= \frac{|\Delta t_{\mathrm{R}}|}{t_{\mathrm{R},2} - t_0} \\ &= \frac{|\Delta k|}{k_2}, \end{aligned} \tag{B.9}$$

$$\begin{aligned} \frac{\alpha - 1}{\alpha + 1} &= \frac{|\Delta t_{\mathrm{R}}|}{t_{\mathrm{R},1} + t_{\mathrm{R},2} - 2t_0} \\ &= \frac{|\Delta k|}{k_1 + k_2}. \end{aligned} \tag{B.10}$$

Knox–Thijssen equation. This equation is based on the assumption that, for close-lying peaks, $\sigma_{\mathrm{t},1} + \sigma_{\mathrm{t},2} = 2\sigma_{\mathrm{t},1}$. Thus,

$$\begin{aligned} R_{\mathrm{S,chrom}} &= \frac{t_{\mathrm{R},2} - t_{\mathrm{R},1}}{4\sigma_{\mathrm{t},1}} \\ &= \frac{|\Delta t_{\mathrm{R}}|}{4\sigma_{\mathrm{t},1}} \frac{t_{\mathrm{R},1}}{t_{\mathrm{R},1}} \\ &= \frac{\sqrt{N_1}}{4} \frac{|\Delta t_{\mathrm{R}}|}{t_{\mathrm{R},1}} \\ &= \frac{\sqrt{N_1}}{4} \frac{|\Delta k|}{1 + k_1} \\ &= \frac{\sqrt{N_1}}{4} (\alpha - 1) \frac{k_1}{1 + k_1}. \end{aligned} \tag{B.11}$$

Upon eliminating the chromatographic migration factor, we obtain the corresponding equation for DTIMS:

$$R_{\mathrm{S,DTIMS}} = \frac{\sqrt{N_1}}{4}(\alpha - 1), \tag{B.12}$$

where $\alpha = K_1/K_2$, the ratio of mobilities.

Purnell equation. The assumption behind this formula is $\sigma_{\mathrm{t},1} + \sigma_{\mathrm{t},2} = 2\sigma_{\mathrm{t},2}$, and thus we may write:

$$\begin{aligned} R_{\mathrm{S,chrom}} &= \frac{t_{\mathrm{R},2} - t_{\mathrm{R},1}}{4\sigma_{\mathrm{t},2}} \\ &= \frac{|\Delta t_{\mathrm{R}}|}{4\sigma_{\mathrm{t},2}} \frac{t_{\mathrm{R},2}}{t_{\mathrm{R},2}} \\ &= \frac{\sqrt{N_2}}{4} \frac{|\Delta t_{\mathrm{R}}|}{t_{\mathrm{R},2}} \\ &= \frac{\sqrt{N_2}}{4} \frac{|\Delta k|}{1 + k_2} \\ &= \frac{\sqrt{N_2}}{4} \frac{\alpha - 1}{\alpha} \frac{k_2}{1 + k_2}. \end{aligned} \tag{B.13}$$

The respective equation for DTIMS:

$$R_{\mathrm{S,DTIMS}} = \frac{\sqrt{N_2}}{4} \frac{\alpha - 1}{\alpha}. \tag{B.14}$$

Karger equation. This equation can be derived assuming $N_1 = N_2 = N$, which also means that

$$\sigma_{\mathrm{t,i}} = \frac{t_{\mathrm{R,i}}}{\sqrt{N}}. \tag{B.15}$$

Employing the above relation, we may write:

$$\begin{aligned} R_{\mathrm{S,chrom}} &= \frac{t_{\mathrm{R},2} - t_{\mathrm{R},1}}{2\sigma_{\mathrm{t},1} + 2\sigma_{\mathrm{t},2}} \\ &= \frac{|\Delta t_{\mathrm{R}}|}{\frac{2}{\sqrt{N}}(t_{\mathrm{R},1} + t_{\mathrm{R},2})} \\ &= \frac{\sqrt{N}}{4}\frac{|\Delta t_{\mathrm{R}}|}{\langle t_{\mathrm{R}}\rangle} \\ &= \frac{\sqrt{N}}{4}\frac{|\Delta k|}{1 + \langle k\rangle} \\ &= \frac{\sqrt{N}}{4}\left(2\frac{\alpha - 1}{\alpha + 1}\frac{\langle k\rangle}{1 + \langle k\rangle}\right). \end{aligned} \tag{B.16}$$

The respective equation for DTIMS:

$$R_{\mathrm{S,DTIMS}} = \frac{\sqrt{N}}{2}\frac{\alpha - 1}{\alpha + 1}. \tag{B.17}$$

Said equation. By introducing N_{avg} as defined in Eq. 4.61 on page 78, an exact resolution equation can be derived:

$$\begin{aligned} R_{\mathrm{S,chrom}} &= \frac{|\Delta t_{\mathrm{R}}|}{4\langle\sigma_{\mathrm{t}}\rangle}\frac{\langle t_{\mathrm{R}}\rangle}{\langle t_{\mathrm{R}}\rangle} \\ &= \frac{\sqrt{N_{\mathrm{avg}}}}{4}\frac{|\Delta t_{\mathrm{R}}|}{\langle t_{\mathrm{R}}\rangle} \\ &= \frac{\sqrt{N_{\mathrm{avg}}}}{4}\frac{|\Delta k|}{1 + \langle k\rangle} \\ &= \frac{\sqrt{N_{\mathrm{avg}}}}{4}\left(2\frac{\alpha - 1}{\alpha + 1}\frac{\langle k\rangle}{1 + \langle k\rangle}\right). \end{aligned} \tag{B.18}$$

Finally, the respective equation for DTIMS: The respective equation for DTIMS:

$$R_{\mathrm{S,DTIMS}} = \frac{\sqrt{N_{\mathrm{avg}}}}{2}\frac{\alpha - 1}{\alpha + 1}. \tag{B.19}$$

Semi-empirical resolution equation for TWIMS. When traveling potential waves are applied to propel ions through the gas-filled mobility cell, the exact relation between t_D and CCS' is not known from first principles. The aforementioned relation is generally described using Eq. 4.70 on page 87. Employing this equation and the notation $1/b = \gamma$, we may write:

$$\begin{aligned} R_\mathrm{S,TWIMS} &= \frac{t_\mathrm{D,2} - t_\mathrm{D,1}}{4\langle \sigma_\mathrm{t} \rangle} \\ &= \frac{\sqrt{N_\mathrm{avg}}}{4} \frac{t_\mathrm{D,2} - t_\mathrm{D,1}}{\langle t_\mathrm{D} \rangle} \\ &= \frac{\sqrt{N_\mathrm{avg}}}{4} \frac{\left(\frac{\mathrm{CCS'}_2}{a}\right)^\gamma - \left(\frac{\mathrm{CCS'}_1}{a}\right)^\gamma}{\left\langle \left(\frac{\mathrm{CCS'}}{a}\right)^\gamma \right\rangle} \\ &= \frac{\sqrt{N_\mathrm{avg}}}{4} \frac{(\mathrm{CCS'}_2)^\gamma - (\mathrm{CCS'}_1)^\gamma}{\langle (\mathrm{CCS'})^\gamma \rangle}. \end{aligned} \tag{B.20}$$

Appendix C

Derivation of an exact peak capacity equation

Considering the systematic variation of the peaks' width across the separation window according to the injection–diffusion model of zone broadening, in Section 4.4.3 we presented an exact peak capacity equation for DTIMS. To obtain the aforementioned formula, Eq. 4.89 on page 94, the following integral needs to be solved:

$$P_{\mathrm{C,DTIMS}} = 1 + \frac{1}{4R_{\mathrm{S}}} \int_{t_{\mathrm{D,1}}}^{t_{\mathrm{D,n}}} \frac{\mathrm{d}t_{\mathrm{D}}}{\sqrt{\sigma_{\mathrm{t,inj}}^2 + \frac{t_{\mathrm{D}}^2}{N_{\mathrm{diff}}}}}. \tag{C.1}$$

Upon dividing both the numerator and the denominator by the t_{D}-independent $\sigma_{\mathrm{t,inj}}$, we obtain

$$P_{\mathrm{C,DTIMS}} = 1 + \frac{1}{4\sigma_{\mathrm{t,inj}} R_{\mathrm{S}}} \int_{t_{\mathrm{D,1}}}^{t_{\mathrm{D,n}}} \frac{\mathrm{d}t_{\mathrm{D}}}{\sqrt{1 + \frac{t_{\mathrm{D}}^2}{\sigma_{\mathrm{t,inj}}^2 N_{\mathrm{diff}}}}}. \tag{C.2}$$

Let us introduce the following notations for brevity:

$$\rho = \frac{1}{\sigma_{\mathrm{t,inj}}^2 N_{\mathrm{diff}}}, \tag{C.3}$$

$$\tau = t_{\mathrm{D}} \sqrt{\rho}. \tag{C.4}$$

From Eq. C.4 it follows that

$$\frac{\mathrm{d}t_{\mathrm{D}}}{\mathrm{d}\tau} = \frac{1}{\sqrt{\rho}}. \tag{C.5}$$

Employing these notations and the derivative above, Eq. C.2 becomes

$$P_{\mathrm{C,DTIMS}} = 1 + \frac{1}{4\sigma_{\mathrm{t,inj}} R_{\mathrm{S}}} \int_{t_{\mathrm{D,1}}}^{t_{\mathrm{D,n}}} \frac{\mathrm{d}t_{\mathrm{D}}}{\sqrt{1+\tau^2}}$$

$$= 1 + \frac{1}{4\sigma_{\mathrm{t,inj}} R_{\mathrm{S}}\sqrt{\rho}} \int_{\tau_1}^{\tau_{\mathrm{n}}} \frac{\mathrm{d}\tau}{\sqrt{1+\tau^2}}. \tag{C.6}$$

The solution of Eq. C.6 can be traced back to the following basic integral:

$$\int \frac{\mathrm{d}x}{\sqrt{1+x^2}} = \operatorname{arsinh}(x) + C$$

$$= \ln\left(x + \sqrt{x^2+1}\right) + C, \tag{C.7}$$

where arsinh is the inverse hyperbolic sine function and C is the constant of integration. Thus, from Eq. C.6 we obtain

$$P_{\mathrm{C,DTIMS}} = 1 + \frac{1}{4\sigma_{\mathrm{t,inj}} R_{\mathrm{S}}\sqrt{\rho}} \left[\operatorname{arsinh}(\tau_{\mathrm{n}}) - \operatorname{arsinh}(\tau_1)\right]$$

$$= 1 + \frac{1}{4\sigma_{\mathrm{t,inj}} R_{\mathrm{S}}\sqrt{\rho}} \ln \frac{\tau_{\mathrm{n}} + \sqrt{\tau_{\mathrm{n}}^2+1}}{\tau_1 + \sqrt{\tau_1^2+1}}. \tag{C.8}$$

The above equation can be rewritten as

$$P_{\mathrm{C,DTIMS}} = 1 + \frac{\sqrt{N_{\mathrm{diff}}}}{4R_{\mathrm{S}}} \ln \frac{t_{\mathrm{D,n}} + \sqrt{t_{\mathrm{D,n}}^2 + \frac{1}{\rho}}}{t_{\mathrm{D,1}} + \sqrt{t_{\mathrm{D,1}}^2 + \frac{1}{\rho}}}. \tag{C.9}$$

From Eq. C.9 we finally obtain the exact peak capacity equation in its logarithmic form as given in Section 4.4.3:

$$P_{\mathrm{C,DTIMS}} = 1 + \frac{\sqrt{N_{\mathrm{diff}}}}{4R_{\mathrm{S}}} \ln \frac{t_{\mathrm{D,n}} + \sqrt{t_{\mathrm{D,n}}^2 + N_{\mathrm{diff}}\,\sigma_{\mathrm{t,inj}}^2}}{t_{\mathrm{D,1}} + \sqrt{t_{\mathrm{D,1}}^2 + N_{\mathrm{diff}}\,\sigma_{\mathrm{t,inj}}^2}}. \tag{C.10}$$

Alternatively, using the arsinh notation, the exact peak capacity equation appears as

$$P_{\mathrm{C,DTIMS}} = 1 + \frac{\sqrt{N_{\mathrm{diff}}}}{4R_{\mathrm{S}}} \left[\operatorname{arsinh}\left(\frac{t_{\mathrm{D,n}}}{\sigma_{\mathrm{t,inj}}\sqrt{N_{\mathrm{diff}}}}\right) - \operatorname{arsinh}\left(\frac{t_{\mathrm{D,1}}}{\sigma_{\mathrm{t,inj}}\sqrt{N_{\mathrm{diff}}}}\right)\right]. \tag{C.11}$$

The equations derived above are applicable when all ions have the same charge state, *i.e.* when N_{diff} is constant across the whole ion mobility spectrum.

If $\sigma_{\mathrm{t,inj}} = 0$, the exact peak capacity equation adopts the following simplified form (see Eq. 4.90 on page 94):

$$P_{\mathrm{C,DTIMS,diff}} = 1 + \frac{\sqrt{N_{\mathrm{diff}}}}{4R_{\mathrm{S}}} \ln \frac{t_{\mathrm{D,n}}}{t_{\mathrm{D,1}}}. \tag{C.12}$$

At the other extreme, when diffusional broadening becomes negligible as N_{diff} approaches infinity, the respective simplified formula (Eq. 4.91) may be found using the following power series expansion of $\operatorname{arsinh}(x)$ about $x = 0$:

$$\begin{aligned} \operatorname{arsinh}(x) &= \sum_{j=0}^{\infty} (-1)^j \frac{(2j-1)!!}{(2j)!!} \frac{x^{2j+1}}{2j+1} \\ &= x - \frac{1}{2}\frac{x^3}{3} + \frac{1 \cdot 3}{2 \cdot 4}\frac{x^5}{5} - \frac{1 \cdot 3 \cdot 5}{2 \cdot 4 \cdot 6}\frac{x^7}{7} + \ldots \end{aligned} \tag{C.13}$$

From the above Maclaurin series it is apparent that, upon neglecting higher-order terms at small values of x, $\operatorname{arsinh}(x) \approx x$. Thus, when diffusional broadening is negligible and the injection pulse alone determines the peak width, Eq. C.11 becomes

$$\begin{aligned} P_{\mathrm{C,DTIMS,inj}} &= 1 + \frac{\sqrt{N_{\mathrm{diff}}}}{4R_{\mathrm{S}}} \left(\frac{t_{\mathrm{D,n}}}{\sigma_{\mathrm{t,inj}}\sqrt{N_{\mathrm{diff}}}} - \frac{t_{\mathrm{D,1}}}{\sigma_{\mathrm{t,inj}}\sqrt{N_{\mathrm{diff}}}} \right) \\ &= 1 + \frac{t_{\mathrm{D,n}} - t_{\mathrm{D,1}}}{4\sigma_{\mathrm{t,inj}} R_{\mathrm{S}}} \\ &= 1 + \frac{\sqrt{N_{\mathrm{inj,1}}}}{4R_{\mathrm{S}}} \frac{t_{\mathrm{D,n}} - t_{\mathrm{D,1}}}{t_{\mathrm{D,1}}}, \end{aligned} \tag{C.14}$$

where $N_{\mathrm{inj,1}} = t_{\mathrm{D,1}}^2 / \sigma_{\mathrm{t,inj}}^2$.

Appendix D

Calculated structures of heparan sulfate disaccharides

As a supplement to Section 5.3, Appendix D contains the lowest-energy structures of the singly deprotonated heparan sulfate disaccharides. The respective calculated infrared spectra between 1000 and 1800 cm^{-1} are also presented. Kim Greis is gratefully acknowledged for performing the quantum chemical calculations.

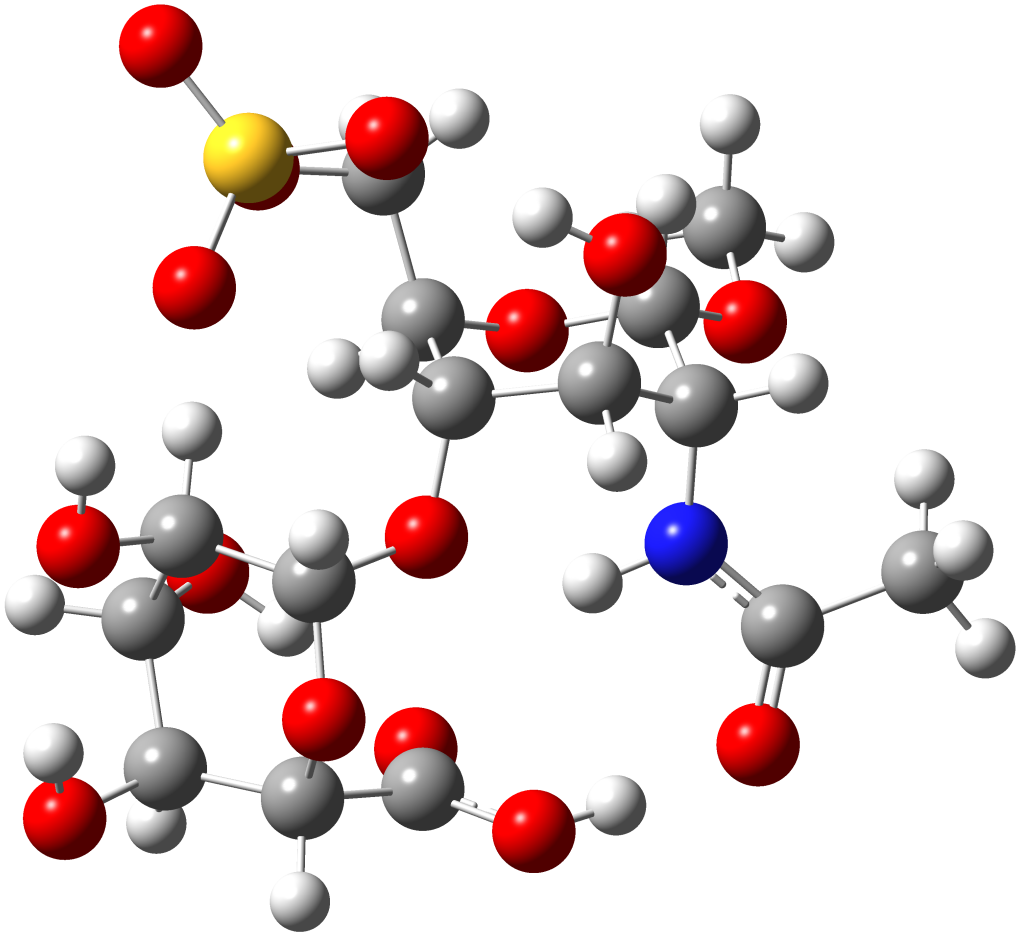

Figure D.1: Lowest energy structure of [GlcA-GlcNAc6S-OCH_3 – H]$^-$, calculated at the PBE0-D3/ma-def2-TZVP level of theory.

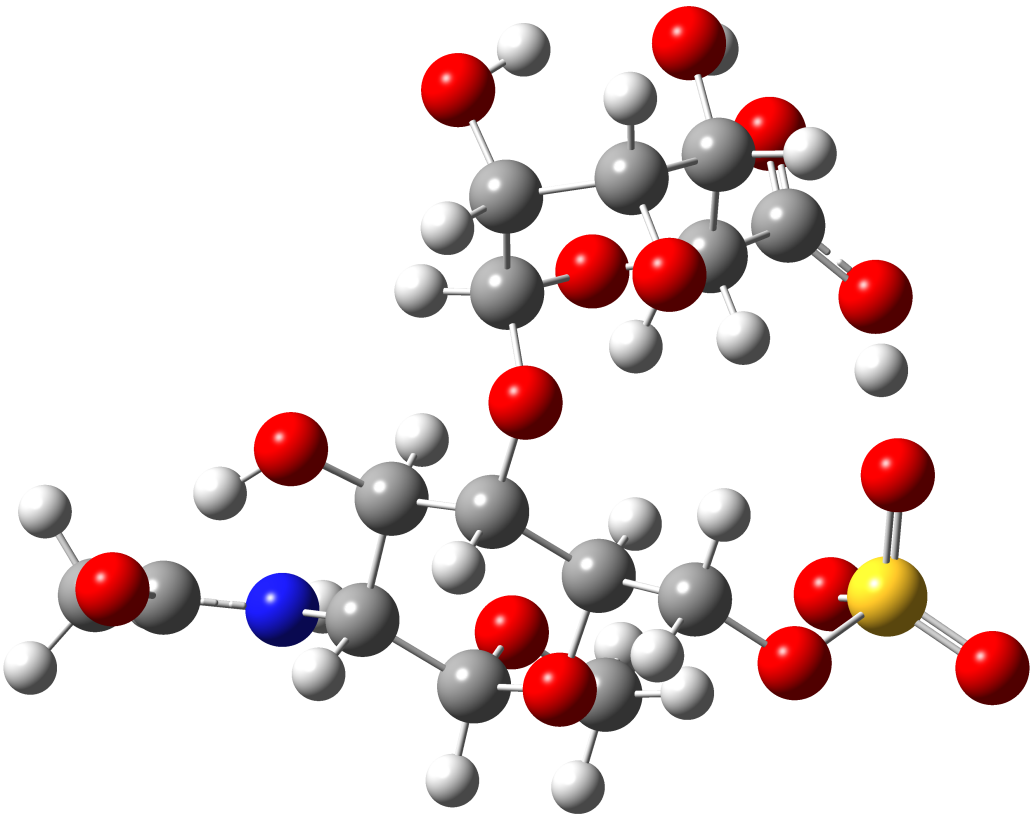

Figure D.2: Lowest energy structure of [IdoA-GlcNAc6S-OCH_3 – H]$^-$, calculated at the PBE0-D3/ma-def2-TZVP level of theory.

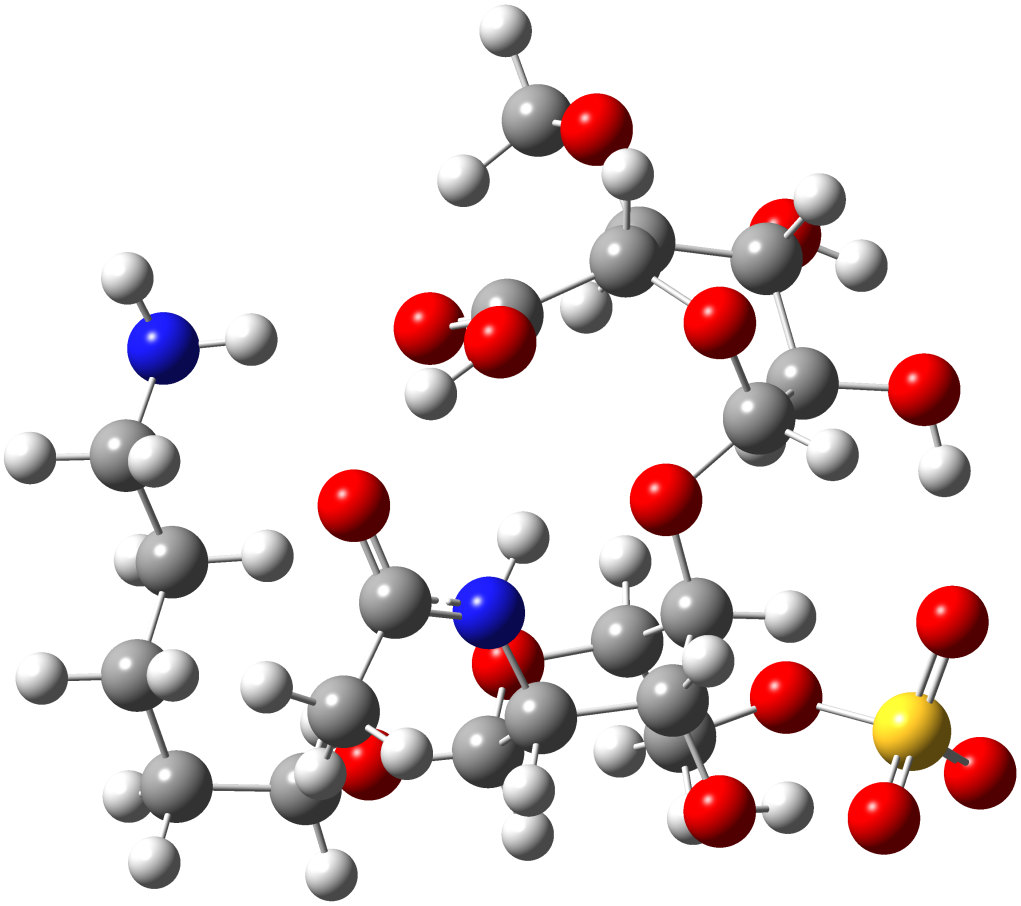

Figure D.3: Lowest energy structure of [GlcA-GlcNAc6S-O$(CH_2)_5NH_2$ – H]$^-$, calculated at the PBE0-D3/ma-def2-TZVP level of theory.

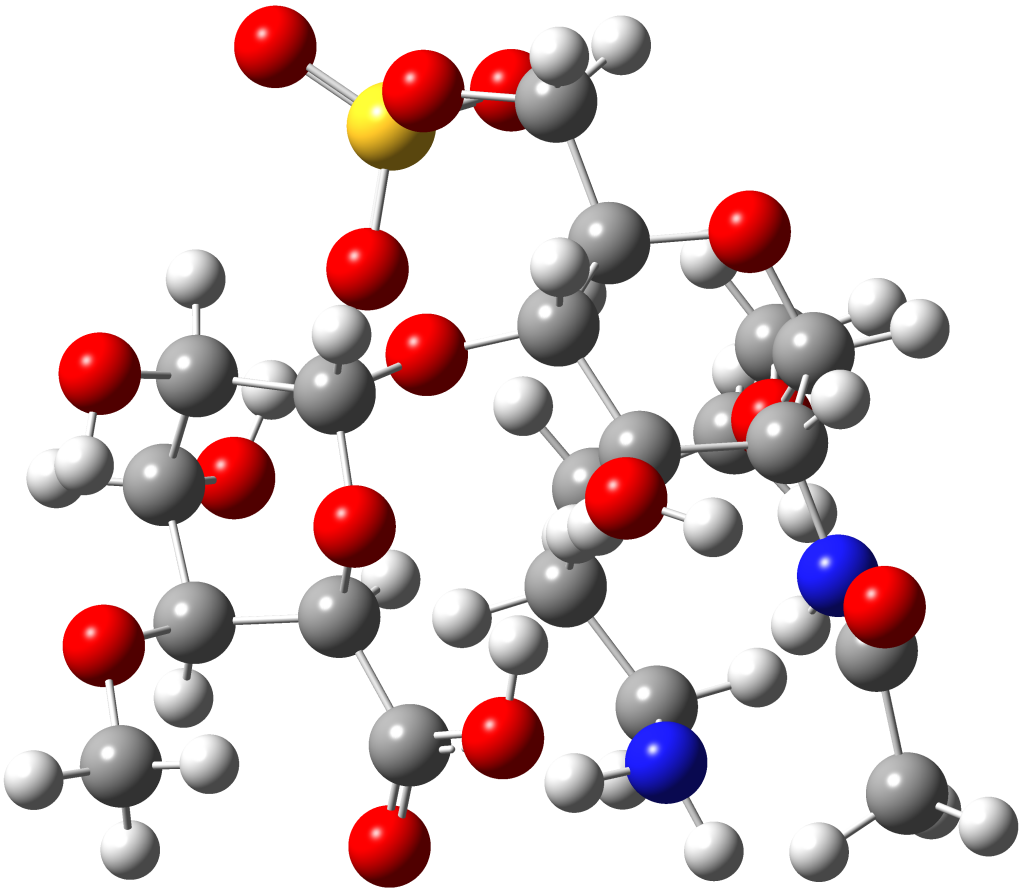

Figure D.4: Lowest energy structure of [IdoA-GlcNAc6S-O$(CH_2)_5NH_2$ – H]$^-$, calculated at the PBE0-D3/ma-def2-TZVP level of theory.

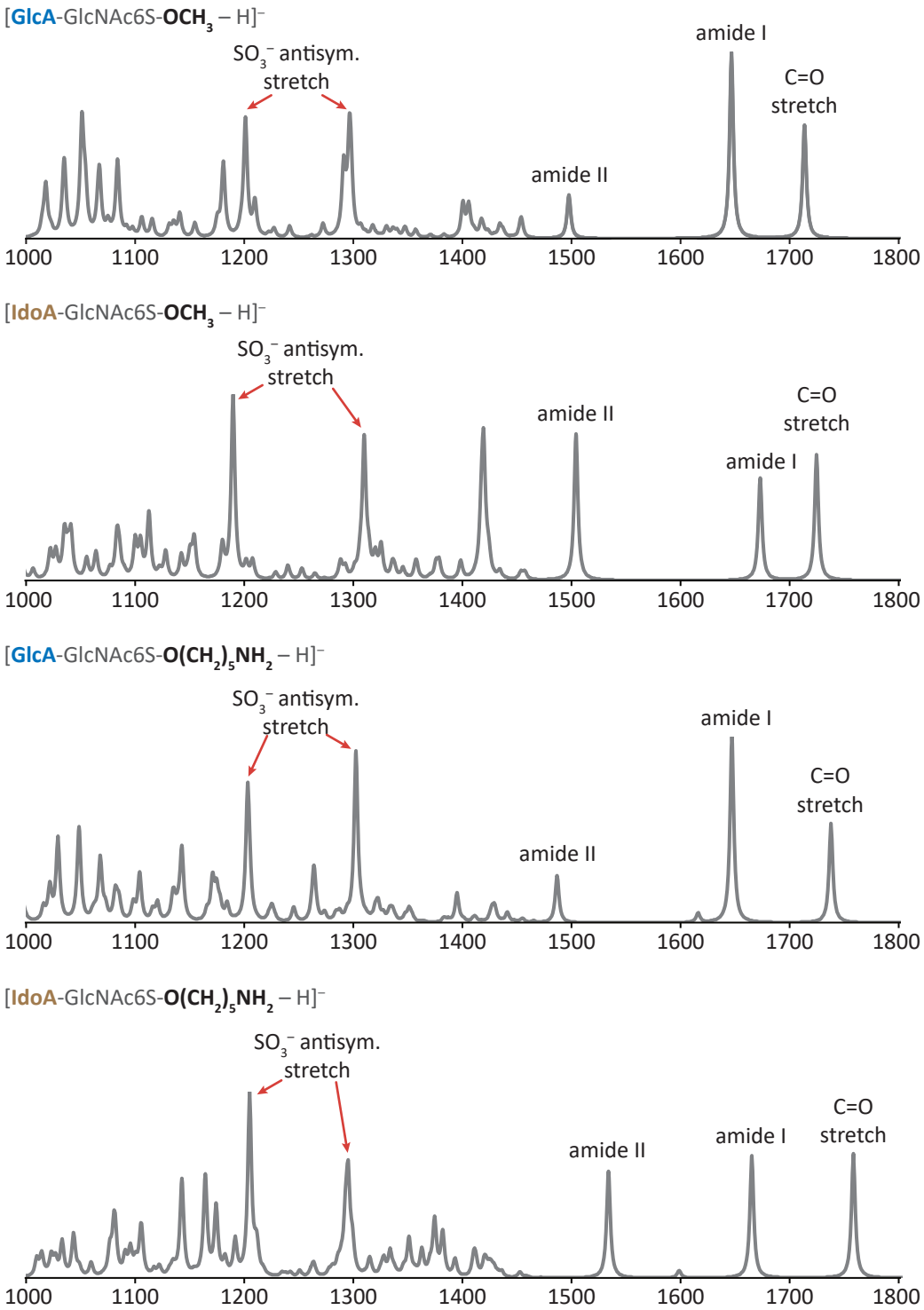

Figure D.5: Computed infrared spectra of the lowest-energy structures of the four heparan sulfate disaccharide anions. Harmonic frequencies were calculated at the PBE0-D3/ma-def2-TZVP level of theory. A scaling factor of 0.965 was employed.

Bibliography

[1] R. B. Merrifield, *Science* **1965**, *150*, 178–185.

[2] F. Sanger, S. Nicklen, A. R. Coulson, *Proceedings of the National Academy of Sciences* **1977**, *74*, 5463–5467.

[3] S. Anderson, A. T. Bankier, B. G. Barrell, M. H. L. de Bruijn, A. R. Coulson, J. Drouin, I. C. Eperon, D. P. Nierlich, B. A. Roe, F. Sanger, P. H. Schreier, A. J. H. Smith, R. Staden, I. G. Young, *Nature* **1981**, *290*, 457–465.

[4] H. Caruthers Marvin, *Science* **1985**, *230*, 281–285.

[5] M. Karas, F. Hillenkamp, *Analytical Chemistry* **1988**, *60*, 2299–2301.

[6] K. Tanaka, H. Waki, Y. Ido, S. Akita, Y. Yoshida, T. Yoshida, T. Matsuo, *Rapid Communications in Mass Spectrometry* **1988**, *2*, 151–153.

[7] J. B. Fenn, M. Mann, C. K. Meng, S. F. Wong, C. M. Whitehouse, *Science* **1989**, *246*, 64–71.

[8] A. Shevchenko, M. Wilm, O. Vorm, M. Mann, *Analytical Chemistry* **1996**, *68*, 850–858.

[9] J. C. Venter *et al.*, *Science* **2001**, *291*, 1304–1351.

[10] E. S. Lander, *Nature* **2011**, *470*, 187–197.

[11] R. Aebersold, M. Mann, *Nature* **2016**, *537*, 347–355.

[12] J. Shendure, S. Balasubramanian, G. M. Church, W. Gilbert, J. Rogers, J. A. Schloss, R. H. Waterston, *Nature* **2017**, *550*, 345–353.

[13] A. Varki, *Glycobiology* **1993**, *3*, 97–130.

[14] R. A. Dwek, *Chemical Reviews* **1996**, *96*, 683–720.

[15] D. H. Dube, C. R. Bertozzi, *Nature Reviews Drug Discovery* **2005**, *4*, 477–488.

[16] J. R. Bishop, M. Schuksz, J. D. Esko, *Nature* **2007**, *446*, 1030–1037.

[17] G. W. Hart, R. J. Copeland, *Cell* **2010**, *143*, 672–676.

[18] A. Varki, *Glycobiology* **2017**, *27*, 3–49.

[19] A. Varki, R. D. Cummings, J. D. Esko, P. Stanley, G. W. Hart, M. Aebi, A. G. Darvill, T. Kinoshita, N. H. Packer, J. H. Prestegard, R. L. Schnaar, P. H. Seeberger, *Essentials of Glycobiology*, Cold Spring Harbor Laboratory Press, New York, 3rd ed., **2017**.

[20] B. A. H. Smith, C. R. Bertozzi, *Nature Reviews Drug Discovery* **2021**, *20*, 217–243.

[21] Y. Mechref, M. V. Novotny, *Chemical Reviews* **2002**, *102*, 321–370.

[22] J. Zaia, *Mass Spectrometry Reviews* **2004**, *23*, 161–227.

[23] J. Zaia, *Chemistry & Biology* **2008**, *15*, 881–892.

[24] K. Mariño, J. Bones, J. J. Kattla, P. M. Rudd, *Nature Chemical Biology* **2010**, *6*, 713–723.

[25] W. R. Alley, M. V. Novotny, *Annual Review of Analytical Chemistry* **2013**, *6*, 237–265.

[26] L. R. Ruhaak, G. Xu, Q. Li, E. Goonatilleke, C. B. Lebrilla, *Chemical Reviews* **2018**, *118*, 7886–7930.

[27] N. de Haan, S. Yang, J. Cipollo, M. Wuhrer, *Nature Reviews Chemistry* **2020**, *4*, 229–242.

[28] H. E. Revercomb, E. A. Mason, *Analytical Chemistry* **1975**, *47*, 970–983.

[29] V. Gabelica, E. Marklund, *Current Opinion in Chemical Biology* **2018**, *42*, 51–59.

[30] M. F. Mesleh, J. M. Hunter, A. A. Shvartsburg, G. C. Schatz, M. F. Jarrold, *The Journal of Physical Chemistry* **1996**, *100*, 16082–16086.

[31] E. G. Marklund, M. T. Degiacomi, C. V. Robinson, A. J. Baldwin, J. L. P. Benesch, *Structure* **2015**, *23*, 791–799.

[32] J. C. May, C. B. Morris, J. A. McLean, *Analytical Chemistry* **2017**, *89*, 1032–1044.

[33] J. C. May, J. A. McLean, *Analytical Chemistry* **2015**, *87*, 1422–1436.

[34] J. Hofmann, K. Pagel, *Angewandte Chemie International Edition* **2017**, *56*, 8342–8349.

[35] V. D'Atri, T. Causon, O. Hernandez-Alba, A. Mutabazi, J.-L. Veuthey, S. Cianferani, D. Guillarme, *Journal of Separation Science* **2017**, *41*, 20–67.

[36] J. C. Giddings, *Unified Separation Science*, Wiley, New York, 1st ed., **1991**.

[37] J. Oomens, B. G. Sartakov, G. Meijer, G. von Helden, *International Journal of Mass Spectrometry* **2006**, *254*, 1–19.

[38] T. R. Rizzo, J. A. Stearns, O. V. Boyarkin, *International Reviews in Physical Chemistry* **2009**, *28*, 481–515.

[39] C. N. Stedwell, J. F. Galindo, A. E. Roitberg, N. C. Polfer, *Annual Review of Analytical Chemistry* **2013**, *6*, 267–285.

[40] E. Mucha, A. I. González Flórez, M. Marianski, D. A. Thomas, W. Hoffmann, W. B. Struwe, H. S. Heung, S. Gewinner, W. Schöllkopf, P. H. Seeberger, G. von Helden, K. Pagel, *Angewandte Chemie International Edition* **2017**, *56*, 11248–11251.

[41] C. Masellis, N. Khanal, M. Z. Kamrath, D. E. Clemmer, T. R. Rizzo, *Journal of The American Society for Mass Spectrometry* **2017**, *28*, 2217–2222.

[42] E. Mucha, A. Stuckmann, M. Marianski, W. B. Struwe, G. Meijer, K. Pagel, *Chemical Science* **2019**, *10*, 1272–1284.

[43] A. I. González Flórez, *Biomolecular Ions in Superfuid Helium Nanodroplets*, PhD Thesis, Freie Universität Berlin, Berlin, **2016**.

[44] E. Mucha, *Vibrational Spectroscopy of Glycans in Helium Nanodroplets*, PhD Thesis, Radboud Universiteit Nijmegen, Nijmegen, **2020**.

[45] E. Mucha, M. Lettow, M. Marianski, D. A. Thomas, W. B. Struwe, D. J. Harvey, G. Meijer, P. H. Seeberger, G. von Helden, K. Pagel, *Angewandte Chemie International Edition* **2018**, *57*, 7440–7443.

[46] E. Mucha, M. Marianski, F.-F. Xu, D. A. Thomas, G. Meijer, G. von Helden, P. H. Seeberger, K. Pagel, *Nature Communications* **2018**, *9*, 4174.

[47] M. Lettow, E. Mucha, C. Manz, D. A. Thomas, M. Marianski, G. Meijer, G. von Helden, K. Pagel, *Analytical and Bioanalytical Chemistry* **2019**, *411*, 4637–4645.

[48] M. Marianski, E. Mucha, K. Greis, S. Moon, A. Pardo, C. Kirschbaum, D. A. Thomas, G. Meijer, G. von Helden, K. Gilmore, P. H. Seeberger, K. Pagel, *Angewandte Chemie International Edition* **2020**, *59*, 6166–6171.

[49] K. Greis, C. Kirschbaum, S. Leichnitz, S. Gewinner, W. Schöllkopf, G. von Helden, G. Meijer, P. H. Seeberger, K. Pagel, *Organic Letters* **2020**, *22*, 8916–8919.

[50] D. Klemm, B. Heublein, H.-P. Fink, A. Bohn, *Angewandte Chemie International Edition* **2005**, *44*, 3358–3393.

[51] M. Rinaudo, *Progress in Polymer Science* **2006**, *31*, 603–632.

[52] A. D. McNaught, *Pure and Applied Chemistry* **1996**, *68*, 1919–2008.

[53] E. Fischer, *Berichte der Deutschen Chemischen Gesellschaft* **1891**, *24*, 2683–2687.

[54] E. Fischer, *Berichte der Deutschen Chemischen Gesellschaft* **1907**, *40*, 102–106.

[55] E. H. Goodyear, W. N. Haworth, *Journal of the Chemical Society* **1927**, 3136–3146.

[56] A. Varki, R. D. Cummings, M. Aebi, N. H. Packer, P. H. Seeberger, J. D. Esko, P. Stanley, G. Hart, A. Darvill, T. Kinoshita, J. J. Prestegard, R. L. Schnaar, H. H. Freeze, J. D. Marth, C. R. Bertozzi, M. E. Etzler, M. Frank, J. F. G. Vliegenthart, T. Lütteke, S. Perez, E. Bolton, P. Rudd, J. Paulson, M. Kanehisa, P. Toukach, K. F. Aoki-Kinoshita, A. Dell, H. Narimatsu, W. York, N. Taniguchi, S. Kornfeld, *Glycobiology* **2015**, *25*, 1323–1324.

[57] A. M. Zivkovic, J. B. German, C. B. Lebrilla, D. A. Mills, *Proceedings of the National Academy of Sciences* **2011**, *108*, 4653–4658.

[58] L. Bode, *Glycobiology* **2012**, *22*, 1147–1162.

[59] L. Bode, E. Jantscher-Krenn, *Advances in Nutrition* **2012**, *3*, 383S–391S.

[60] S. Sarrazin, W. C. Lamanna, J. D. Esko, *Cold Spring Harbor Perspectives in Biology* **2011**, *3*, 7.

[61] K. K. Palaniappan, C. R. Bertozzi, *Chemical Reviews* **2016**, *116*, 14277–14306.

[62] H. S. Bennett, *Journal of Histochemistry & Cytochemistry* **1963**, *11*, 14–23.

[63] J. M. Tarbell, L. M. Cancel, *Journal of Internal Medicine* **2016**, *280*, 97–113.

[64] A.-J. Petrescu, M. R. Wormald, R. A. Dwek, *Current Opinion in Structural Biology* **2006**, *16*, 600–607.

[65] D. Shental-Bechor, Y. Levy, *Current Opinion in Structural Biology* **2009**, *19*, 524–533.

[66] S. D. Rosen, C. R. Bertozzi, *Current Opinion in Cell Biology* **1994**, *6*, 663–673.

[67] B. E. Collins, J. C. Paulson, *Current Opinion in Chemical Biology* **2004**, *8*, 617–625.

[68] H.-J. Gabius, S. André, J. Jiménez-Barbero, A. Romero, D. Solís, *Trends in Biochemical Sciences* **2011**, *36*, 298–313.

[69] D. Xu, J. D. Esko, *Annual Review of Biochemistry* **2014**, *83*, 129–157.

[70] W. J. Snell, J. M. White, *Cell* **1996**, *85*, 629–637.

[71] D. R. P. Tulsiani, H. Yoshida-Komiya, Y. Araki, *Biology of Reproduction* **1997**, *57*, 487–494.

[72] P.-C. Pang, C. N. Chiu Philip, C.-L. Lee, L.-Y. Chang, M. Panico, R. Morris Howard, M. Haslam Stuart, K.-H. Khoo, F. Clark Gary, S. B. Yeung William, A. Dell, *Science* **2011**, *333*, 1761–1764.

[73] R. Sasisekharan, Z. Shriver, G. Venkataraman, U. Narayanasami, *Nature Reviews Cancer* **2002**, *2*, 521–528.

[74] J. U. Baenziger, D. Fiete, *J Biol Chem* **1979**, *254*, 9795–9799.

[75] R. L. Richards, J. Moss, C. R. Alving, P. H. Fishman, R. O. Brady, *Proceedings of the National Academy of Sciences* **1979**, *76*, 1673–1676.

[76] B. K. L. Sim, C. E. Chitnis, K. Wasniowska, T. J. Hadley, L. H. Miller, *Science* **1994**, *264*, 1941–1944.

[77] P. H. Seeberger, D. B. Werz, *Nature* **2007**, *446*, 1046–1051.

[78] C. Anish, B. Schumann, C. L. Pereira, P. H. Seeberger, *Chemistry & Biology* **2014**, *21*, 38–50.

[79] T. J. Boltje, T. Buskas, G.-J. Boons, *Nature Chemistry* **2009**, *1*, 611–622.

[80] B. Ernst, J. L. Magnani, *Nature Reviews Drug Discovery* **2009**, *8*, 661–677.

[81] J. E. Hudak, C. R. Bertozzi, *Chemistry & Biology* **2014**, *21*, 16–37.

[82] U. Lindahl, J. Couchman, K. Kimata, J. D. Esko in *Essentials of Glycobiology* (Eds.: A. Varki, R. D. Cummings, J. D. Esko, P. Stanley, G. W. Hart, M. Aebi, A. G. Darvill, T. Kinoshita, N. H. Packer, J. H. Prestegard, R. L. Schnaar, P. H. Seeberger), Cold Spring Harbor Laboratory Press, New York, 3rd ed., **2017**, book section Chapter 17., pp. 207–221.

[83] I. Capila, R. J. Linhardt, *Angewandte Chemie International Edition* **2002**, *41*, 390–412.

[84] S. Mizumoto, S. Yamada, K. Sugahara, *Current Opinion in Structural Biology* **2015**, *34*, 35–42.

[85] L. Kjellén, U. Lindahl, *Current Opinion in Structural Biology* **2018**, *50*, 101–108.

[86] S. D. Vallet, O. Clerc, S. Ricard-Blum, *Journal of Histochemistry & Cytochemistry* **2020**, *69*, 93–104.

[87] T. N. Laremore, F. Zhang, J. S. Dordick, J. Liu, R. J. Linhardt, *Current Opinion in Chemical Biology* **2009**, *13*, 633–640.

[88] B. P. Toole, *Nature Reviews Cancer* **2004**, *4*, 528–539.

[89] C. R. Parish, *Nature Reviews Immunology* **2006**, *6*, 633–643.

[90] T. Mikami, H. Kitagawa, *Biochimica et Biophysica Acta (BBA) - General Subjects* **2013**, *1830*, 4719–4733.

[91] N. K. Karamanos, Z. Piperigkou, A. D. Theocharis, H. Watanabe, M. Franchi, S. Baud, S. Brézillon, M. Götte, A. Passi, D. Vigetti, S. Ricard-Blum, R. D. Sanderson, T. Neill, R. V. Iozzo, *Chemical Reviews* **2018**, *118*, 9152–9232.

[92] P. Zhang, H. Lu, R. T. Peixoto, M. K. Pines, Y. Ge, S. Oku, T. J. Siddiqui, Y. Xie, W. Wu, S. Archer-Hartmann, K. Yoshida, K. F. Tanaka, A. R. Aricescu, P. Azadi, M. D. Gordon, B. L. Sabatini, R. O. L. Wong, A. M. Craig, *Cell* **2018**, *174*, 1450–1464.

[93] R. Sasisekharan, R. Raman, V. Prabhakar, *Annual Review of Biomedical Engineering* **2006**, *8*, 181–231.

[94] V. Hascall, J. D. Esko in *Essentials of Glycobiology* (Eds.: A. Varki, R. D. Cummings, J. D. Esko, P. Stanley, G. W. Hart, M. Aebi, A. G. Darvill, T. Kinoshita, N. H. Packer, J. H. Prestegard, R. L. Schnaar, P. H. Seeberger), Cold Spring Harbor Laboratory Press, New York, 3rd ed., **2017**, book section Chapter 16., pp. 197–206.

[95] K. Sugahara, T. Mikami, T. Uyama, S. Mizuguchi, K. Nomura, H. Kitagawa, *Current Opinion in Structural Biology* **2003**, *13*, 612–620.

[96] C. I. Gama, S. E. Tully, N. Sotogaku, P. M. Clark, M. Rawat, N. Vaidehi, W. A. Goddard III, A. Nishi, L. C. Hsieh-Wilson, *Nature Chemical Biology* **2006**, *2*, 467–473.

[97] J. D. Esko, S. B. Selleck, *Annual Review of Biochemistry* **2002**, *71*, 435–471.

[98] J. Kreuger, L. Kjellén, *Journal of Histochemistry & Cytochemistry* **2012**, *60*, 898–907.

[99] B. E. Thacker, D. Xu, R. Lawrence, J. D. Esko, *Matrix Biology* **2014**, *35*, 60–72.

[100] J. D. Esko, U. Lindahl, *The Journal of Clinical Investigation* **2001**, *108*, 169–173.

[101] C. J. Jones, S. Beni, J. F. K. Limtiaco, D. J. Langeslay, C. K. Larive, *Annual Review of Analytical Chemistry* **2011**, *4*, 439–465.

[102] R. J. Linhardt, *Journal of Medicinal Chemistry* **2003**, *46*, 2551–2564.

[103] J. L. Funderburgh, *Glycobiology* **2000**, *10*, 951–958.

[104] B. Caterson, J. Melrose, *Glycobiology* **2018**, *28*, 182–206.

[105] M. Ly, F. E. Leach III, T. N. Laremore, T. Toida, I. J. Amster, R. J. Linhardt, *Nature Chemical Biology* **2011**, *7*, 827–833.

[106] Y. Yu, J. Duan, F. E. Leach, T. Toida, K. Higashi, H. Zhang, F. Zhang, I. J. Amster, R. J. Linhardt, *Journal of the American Chemical Society* **2017**, *139*, 16986–16995.

[107] T. H. van Kuppevelt, A. Oosterhof, E. M. M. Versteeg, E. Podhumljak, E. M. A. van de Westerlo, W. F. Daamen, *Scientific Reports* **2017**, *7*, 14785.

[108] L. Li, M. Ly, R. J. Linhardt, *Molecular BioSystems* **2012**, *8*, 1613–1625.

[109] L. Bohlmann, G. D. Tredwell, X. Yu, C.-W. Chang, T. Haselhorst, M. Winger, J. C. Dyason, R. J. Thomson, J. Tiralongo, I. R. Beacham, H. Blanchard, M. von Itzstein, *Nature Chemical Biology* **2015**, *11*, 955–957.

[110] Y. Yu, A. Williams, X. Zhang, L. Fu, K. Xia, Y. Xu, F. Zhang, J. Liu, M. Koffas, R. J. Linhardt, *Glycobiology* **2019**, *29*, 572–581.

[111] J. Zaia, *Mass Spectrometry Reviews* **2009**, *28*, 254–272.

[112] Y. Song, F. Zhang, R. J. Linhardt, *Journal of Histochemistry & Cytochemistry* **2020**, *69*, 121–135.

[113] L. E. Pepi, P. Sanderson, M. Stickney, I. J. Amster, *Molecular & Cellular Proteomics* **2021**, 100025.

[114] M. Yamashita, J. B. Fenn, *The Journal of Physical Chemistry* **1984**, *88*, 4451–4459.

[115] M. Yamashita, J. B. Fenn, *The Journal of Physical Chemistry* **1984**, *88*, 4671–4675.

[116] M. Dole, L. L. Mack, R. L. Hines, R. C. Mobley, L. D. Ferguson, M. B. Alice, *The Journal of Chemical Physics* **1968**, *49*, 2240–2249.

[117] L. L. Mack, P. Kralik, A. Rheude, M. Dole, *The Journal of Chemical Physics* **1970**, *52*, 4977–4986.

[118] G. A. Clegg, M. Dole, *Biopolymers* **1971**, *10*, 821–826.

[119] J. B. Fenn, M. Mann, C. K. Meng, S. F. Wong, C. M. Whitehouse, *Mass Spectrometry Reviews* **1990**, *9*, 37–70.

[120] M. S. Wilm, M. Mann, *International Journal of Mass Spectrometry and Ion Processes* **1994**, *136*, 167–180.

[121] J. B. Fenn, *Angewandte Chemie International Edition* **2003**, *42*, 3871–3894.

[122] G. I. Taylor, *Proceedings of the Royal Society of London. Series A. Mathematical and Physical Sciences* **1964**, *280*, 383–397.

[123] P. Kebarle, U. H. Verkerk, *Mass Spectrometry Reviews* **2009**, *28*, 898–917.

[124] L. Konermann, E. Ahadi, A. D. Rodriguez, S. Vahidi, *Analytical Chemistry* **2013**, *85*, 2–9.

[125] A. T. Iavarone, E. R. Williams, *Journal of the American Chemical Society* **2003**, *125*, 2319–2327.

[126] K. L. Duffin, J. K. Welply, E. Huang, J. D. Henion, *Analytical Chemistry* **1992**, *64*, 1440–1448.

[127] V. N. Reinhold, B. B. Reinhold, C. E. Costello, *Analytical Chemistry* **1995**, *67*, 1772–1784.

[128] D. J. Harvey, *Journal of Mass Spectrometry* **2000**, *35*, 1178–1190.

[129] J. Zaia, C. E. Costello, *Analytical Chemistry* **2001**, *73*, 233–239.

[130] M. Wuhrer, A. R. de Boer, A. M. Deelder, *Mass Spectrometry Reviews* **2009**, *28*, 192–206.

[131] J. Zaia, *OMICS: A Journal of Integrative Biology* **2010**, *14*, 401–418.

[132] W. R. Alley, B. F. Mann, M. V. Novotny, *Chemical Reviews* **2013**, *113*, 2668–2732.

[133] V. Gabelica, E. De Pauw, *Mass Spectrometry Reviews* **2004**, *24*, 566–587.

[134] B. Domon, C. E. Costello, *Glycoconjugate Journal* **1988**, *5*, 397–409.

[135] R. G. Ewing, D. A. Atkinson, G. A. Eiceman, G. J. Ewing, *Talanta* **2001**, *54*, 515–529.

[136] H. Borsdorf, G. A. Eiceman, *Applied Spectroscopy Reviews* **2006**, *41*, 323–375.

[137] G. A. Eiceman, Z. Karpas, H. H. J. Hill, *Ion Mobility Spectrometry*, CRC Press, 3rd ed., **2013**.

[138] E. W. McDaniel, D. W. Martin, W. S. Barnes, *Review of Scientific Instruments* **1962**, *33*, 2–7.

[139] G. von Helden, M. Hsu, P. R. Kemper, M. T. Bowers, *The Journal of Chemical Physics* **1991**, *95*, 3835–3837.

[140] M. T. Bowers, P. R. Kemper, G. von Helden, P. A. M. van Koppen, *Science* **1993**, *260*, 1446–1451.

[141] D. E. Clemmer, R. R. Hudgins, M. F. Jarrold, *Journal of the American Chemical Society* **1995**, *117*, 10141–10142.

[142] M. F. Jarrold, *Annual Review of Physical Chemistry* **2000**, *51*, 179–207.

[143] B. T. Ruotolo, K. Giles, I. Campuzano, A. M. Sandercock, R. H. Bateman, C. V. Robinson, *Science* **2005**, *310*, 1658–1661.

[144] B. T. Ruotolo, J. L. P. Benesch, A. M. Sandercock, S.-J. Hyung, C. V. Robinson, *Nature Protocols* **2008**, *3*, 1139–1152.

[145] C. Bleiholder, N. F. Dupuis, T. Wyttenbach, M. T. Bowers, *Nature Chemistry* **2011**, *3*, 172–177.

[146] C. Uetrecht, I. M. Barbu, G. K. Shoemaker, E. van Duijn, A. J. R. Heck, *Nature Chemistry* **2011**, *3*, 126–132.

[147] S. Warnke, G. von Helden, K. Pagel, *Journal of the American Chemical Society* **2013**, *135*, 1177–1180.

[148] J. Abi-Ghanem, V. Gabelica, *Physical Chemistry Chemical Physics* **2014**, *16*, 21204–21218.

[149] A. Laganowsky, E. Reading, T. M. Allison, M. B. Ulmschneider, M. T. Degiacomi, A. J. Baldwin, C. V. Robinson, *Nature* **2014**, *510*, 172–175.

[150] K. A. Servage, J. A. Silveira, K. L. Fort, D. H. Russell, *Accounts of Chemical Research* **2016**, *49*, 1421–1428.

[151] M. Bedair, L. W. Sumner, *TrAC Trends in Analytical Chemistry* **2008**, *27*, 238–250.

[152] D. Helm, J. P. C. Vissers, C. J. Hughes, H. Hahne, B. Ruprecht, F. Pachl, A. Grzyb, K. Richardson, J. Wildgoose, S. K. Maier, H. Marx, M. Wilhelm, I. Becher, S. Lemeer, M. Bantscheff, J. I. Langridge, B. Kuster, *Molecular & Cellular Proteomics* **2014**, *13*, 3709–3715.

[153] J. C. May, C. R. Goodwin, J. A. McLean, *Current Opinion in Biotechnology* **2015**, *31*, 117–121.

[154] G. Paglia, P. Angel, J. P. Williams, K. Richardson, H. J. Olivos, J. W. Thompson, L. Menikarachchi, S. Lai, C. Walsh, A. Moseley, R. S. Plumb, D. F. Grant, B. O. Palsson, J. Langridge, S. Geromanos, G. Astarita, *Analytical Chemistry* **2015**, *87*, 1137–1144.

[155] G. Paglia, G. Astarita, *Nature Protocols* **2017**, *12*, 797–813.

[156] T. Mairinger, T. J. Causon, S. Hann, *Current Opinion in Chemical Biology* **2018**, *42*, 9–15.

[157] K. E. Burnum-Johnson, X. Zheng, J. N. Dodds, J. Ash, D. Fourches, C. D. Nicora, J. P. Wendler, T. O. Metz, K. M. Waters, J. K. Jansson, R. D. Smith, E. S. Baker, *TrAC Trends in Analytical Chemistry* **2019**, *116*, 292–299.

[158] K. L. Leaptrot, J. C. May, J. N. Dodds, J. A. McLean, *Nature Communications* **2019**, *10*, 985.

[159] C. G. Vasilopoulou, K. Sulek, A.-D. Brunner, N. S. Meitei, U. Schweiger-Hufnagel, S. W. Meyer, A. Barsch, M. Mann, F. Meier, *Nature Communications* **2020**, *11*, 331.

[160] C. J. Gray, B. Thomas, R. Upton, L. G. Migas, C. E. Eyers, P. E. Barran, S. L. Flitsch, *Biochimica et Biophysica Acta (BBA) - General Subjects* **2016**, *1860*, 1688–1709.

[161] Z. Chen, M. S. Glover, L. Li, *Current Opinion in Chemical Biology* **2018**, *42*, 1–8.

[162] C. Manz, K. Pagel, *Current Opinion in Chemical Biology* **2018**, *42*, 16–24.

[163] A. Mookherjee, M. Guttman, *Current Opinion in Chemical Biology* **2018**, *42*, 86–92.

[164] C. J. Gray, L. G. Migas, P. E. Barran, K. Pagel, P. H. Seeberger, C. E. Eyers, G.-J. Boons, N. L. B. Pohl, I. Compagnon, G. Widmalm, S. L. Flitsch, *Journal of the American Chemical Society* **2019**, *141*, 14463–14479.

[165] P. Dwivedi, B. Bendiak, B. H. Clowers, H. H. Hill, *Journal of the American Society for Mass Spectrometry* **2007**, *18*, 1163–1175.

[166] L. S. Fenn, J. A. McLean, *Physical Chemistry Chemical Physics* **2011**, *13*, 2196–2205.

[167] J. Hofmann, H. S. Hahm, P. H. Seeberger, K. Pagel, *Nature* **2015**, *526*, 241–244.

[168] G. Nagy, I. K. Attah, S. V. B. Garimella, K. Tang, Y. M. Ibrahim, E. S. Baker, R. D. Smith, *Chemical Communications* **2018**, *54*, 11701–11704.

[169] T. J. Causon, S. Hann, *Journal of Chromatography A* **2015**, *1416*, 47–56.

[170] E. A. Mason, H. W. Schamp, *Annals of Physics* **1958**, *4*, 233–270.

[171] L. A. Viehland, *Gaseous Ion Mobility, Diffusion, and Reaction*, Springer, 1st ed., **2018**.

[172] V. Gabelica, A. A. Shvartsburg, C. Afonso, P. Barran, J. L. P. Benesch, C. Bleiholder, M. T. Bowers, A. Bilbao, M. F. Bush, J. L. Campbell, I. D. G. Campuzano, T. Causon, B. H. Clowers, C. S. Creaser, E. De Pauw, J. Far, F. Fernandez-Lima, J. C. Fjeldsted, K. Giles, M. Groessl, C. J. Hogan Jr, S. Hann, H. I. Kim, R. T. Kurulugama, J. C. May, J. A. McLean, K. Pagel, K. Richardson, M. E. Ridgeway, F. Rosu, F. Sobott, K. Thalassinos, S. J. Valentine, T. Wyttenbach, *Mass Spectrometry Reviews* **2019**, *38*, 291–320.

[173] E. A. Mason, E. W. McDaniel, *Transport Properties of Ions in Gases*, Wiley, New York, 1st ed., **1988**.

[174] J. N. Dodds, E. S. Baker, *Journal of The American Society for Mass Spectrometry* **2019**, *30*, 2185–2195.

[175] A. T. Kirk, A. Bohnhorst, C.-R. Raddatz, M. Allers, S. Zimmermann, *Analytical and Bioanalytical Chemistry* **2019**, *411*, 6229–6246.

[176] S. M. Stow, T. J. Causon, X. Zheng, R. T. Kurulugama, T. Mairinger, J. C. May, E. E. Rennie, E. S. Baker, R. D. Smith, J. A. McLean, S. Hann, J. C. Fjeldsted, *Analytical Chemistry* **2017**, *89*, 9048–9055.

[177] K. Giles, S. D. Pringle, K. R. Worthington, D. Little, J. L. Wildgoose, R. H. Bateman, *Rapid Communications in Mass Spectrometry* **2004**, *18*, 2401–2414.

[178] K. Giles, J. P. Williams, I. Campuzano, *Rapid Communications in Mass Spectrometry* **2011**, *25*, 1559–1566.

[179] I. D. G. Campuzano, K. Giles, *TrAC Trends in Analytical Chemistry* **2019**, *120*, 115620.

[180] A. A. Shvartsburg, R. D. Smith, *Analytical Chemistry* **2008**, *80*, 9689–9699.

[181] K. Richardson, D. Langridge, K. Giles, *International Journal of Mass Spectrometry* **2018**, *428*, 71–80.

[182] D. P. Smith, T. W. Knapman, I. Campuzano, R. W. Malham, J. T. Berryman, S. E. Radford, A. E. Ashcroft, *European Journal of Mass Spectrometry* **2009**, *15*, 113–130.

[183] M. F. Bush, Z. Hall, K. Giles, J. Hoyes, C. V. Robinson, B. T. Ruotolo, *Analytical Chemistry* **2010**, *82*, 9557–9565.

[184] J. G. Forsythe, A. S. Petrov, C. A. Walker, S. J. Allen, J. S. Pellissier, M. F. Bush, N. V. Hud, F. M. Fernández, *Analyst* **2015**, *140*, 6853–6861.

[185] J. R. N. Haler, C. Kune, P. Massonnet, C. Comby-Zerbino, J. Jordens, M. Honing, Y. Mengerink, J. Far, E. De Pauw, *Analytical Chemistry* **2017**, *89*, 12076–12086.

[186] L. Deng, I. K. Webb, S. V. B. Garimella, A. M. Hamid, X. Zheng, R. V. Norheim, S. A. Prost, G. A. Anderson, J. A. Sandoval, E. S. Baker, Y. M. Ibrahim, R. D. Smith, *Analytical Chemistry* **2017**, *89*, 4628–4634.

[187] K. Giles, J. Ujma, J. Wildgoose, S. Pringle, K. Richardson, D. Langridge, M. Green, *Analytical Chemistry* **2019**, *91*, 8564–8573.

[188] J. Ujma, D. Ropartz, K. Giles, K. Richardson, D. Langridge, J. Wildgoose, M. Green, S. Pringle, *Journal of the American Society for Mass Spectrometry* **2019**, *30*, 1028–1037.

[189] S. Warnke, A. Ben Faleh, V. Scutelnic, T. R. Rizzo, *Journal of the American Society for Mass Spectrometry* **2019**, *30*, 2204–2211.

[190] G. von Helden, M. T. Hsu, N. Gotts, M. T. Bowers, *The Journal of Physical Chemistry* **1993**, *97*, 8182–8192.

[191] K.-M. Ho, A. A. Shvartsburg, B. Pan, Z.-Y. Lu, C.-Z. Wang, J. G. Wacker, J. L. Fye, M. F. Jarrold, *Nature* **1998**, *392*, 582–585.

[192] F. Furche, R. Ahlrichs, P. Weis, C. Jacob, S. Gilb, T. Bierweiler, M. M. Kappes, *The Journal of Chemical Physics* **2002**, *117*, 6982–6990.

[193] V. D'Atri, M. Porrini, F. Rosu, V. Gabelica, *Journal of Mass Spectrometry* **2015**, *50*, 711–726.

[194] A. A. Shvartsburg, M. F. Jarrold, *Chemical Physics Letters* **1996**, *261*, 86–91.

[195] L. A. Viehland, *Computer Physics Communications* **2001**, *142*, 7–13.

[196] C. Bleiholder, T. Wyttenbach, M. T. Bowers, *International Journal of Mass Spectrometry* **2011**, *308*, 1–10.

[197] C. Larriba, C. J. Hogan, *The Journal of Physical Chemistry A* **2013**, *117*, 3887–3901.

[198] L. Zanotto, G. Heerdt, P. C. T. Souza, G. Araujo, M. S. Skaf, *Journal of Computational Chemistry* **2018**, *39*, 1675–1681.

[199] C. Ieritano, J. Crouse, J. L. Campbell, W. S. Hopkins, *Analyst* **2019**, *144*, 1660–1670.

[200] J. M. Hollas, *Modern Spectroscopy*, Wiley, New York, 4th ed., **2004**.

[201] P. M. Morse, *Physical Review* **1929**, *34*, 57–64.

[202] K. R. Asmis, N. L. Pivonka, G. Santambrogio, M. Brümmer, C. Kaposta, D. M. Neumark, L. Wöste, *Science* **2003**, *299*, 1375–1377.

[203] N. C. Polfer, *Chemical Society Reviews* **2011**, *40*, 2211–2221.

[204] J. Seo, S. Warnke, K. Pagel, M. T. Bowers, G. von Helden, *Nature Chemistry* **2017**, *9*, 1263–1268.

[205] J. M. Lisy, *The Journal of Chemical Physics* **2006**, *125*, 132302.

[206] A. B. Wolk, C. M. Leavitt, E. Garand, M. A. Johnson, *Accounts of Chemical Research* **2014**, *47*, 202–210.

[207] J. Roithová, A. Gray, E. Andris, J. Jašík, D. Gerlich, *Accounts of Chemical Research* **2016**, *49*, 223–230.

[208] M. Z. Kamrath, T. R. Rizzo, *Accounts of Chemical Research* **2018**, *51*, 1487–1495.

[209] X. Zhang, N. B. Brauer, G. Berden, A. M. Rijs, M. Drabbels, *The Journal of Chemical Physics* **2012**, *136*, 044305.

[210] A. I. González Flórez, D.-S. Ahn, S. Gewinner, W. Schöllkopf, G. von Helden, *Physical Chemistry Chemical Physics* **2015**, *17*, 21902–21911.

[211] J. P. Toennies, A. F. Vilesov, *Angewandte Chemie International Edition* **2004**, *43*, 2622–2648.

[212] L. Tisza, *Nature* **1938**, *141*, 913–913.

[213] L. Landau, *Physical Review* **1941**, *60*, 356–358.

[214] E. Andronikashvili, *Journal of Physics USSR* **1946**, *10*, 201.

[215] S. Grebenev, P. J. Toennies, F. Vilesov, Andrei, *Science* **1998**, *279*, 2083–2086.

[216] A. Scheidemann, J. P. Toennies, J. A. Northby, *Physical Review Letters* **1990**, *64*, 1899–1902.

[217] M. Y. Choi, G. E. Douberly, T. M. Falconer, W. K. Lewis, C. M. Lindsay, J. M. Merritt, P. L. Stiles, R. E. Miller, *International Reviews in Physical Chemistry* **2006**, *25*, 15–75.

[218] F. Bierau, P. Kupser, G. Meijer, G. von Helden, *Physical Review Letters* **2010**, *105*, 133402.

[219] F. Filsinger, D.-S. Ahn, G. Meijer, G. von Helden, *Physical Chemistry Chemical Physics* **2012**, *14*, 13370–13377.

[220] S. Goyal, D. L. Schutt, G. Scoles, *Physical Review Letters* **1992**, *69*, 933–936.

[221] M. Hartmann, R. E. Miller, J. P. Toennies, A. Vilesov, *Physical Review Letters* **1995**, *75*, 1566–1569.

[222] M. Hartmann, E. Miller Roger, J. P. Toennies, F. Vilesov Andrej, *Science* **1996**, *272*, 1631–1634.

[223] K. Nauta, D. T. Moore, P. L. Stiles, R. E. Miller, *Science* **2001**, *292*, 481–484.

[224] S. Smolarek, N. B. Brauer, W. J. Buma, M. Drabbels, *Journal of the American Chemical Society* **2010**, *132*, 14086–14091.

[225] D. A. Thomas, E. Mucha, S. Gewinner, W. Schöllkopf, G. Meijer, G. von Helden, *The Journal of Physical Chemistry Letters* **2018**, *9*, 2305–2310.

[226] D. A. Thomas, M. Marianski, E. Mucha, G. Meijer, M. A. Johnson, G. von Helden, *Angewandte Chemie International Edition* **2018**, *57*, 10615–10619.

[227] N. B. Brauer, S. Smolarek, X. Zhang, W. J. Buma, M. Drabbels, *The Journal of Physical Chemistry Letters* **2011**, *2*, 1563–1566.

[228] F. Dalfovo, A. Lastri, L. Pricaupenko, S. Stringari, J. Treiner, *Physical Review B* **1995**, *52*, 1193–1209.

[229] S. J. Allen, M. F. Bush, *Journal of The American Society for Mass Spectrometry* **2016**, *27*, 2054–2063.

[230] D. Pentlehner, R. Riechers, B. Dick, A. Slenczka, U. Even, N. Lavie, R. Brown, K. Luria, *Review of Scientific Instruments* **2009**, *80*, 043302.

[231] W. Schöllkopf, S. Gewinner, H. Junkes, A. Paarmann, G. von Helden, H. P. Bluem, M. M. Todd, Alan, *Proc. SPIE Int. Soc. Opt. Eng.*, **2015**, p. 95121L.

[232] D. A. G. Deacon, L. R. Elias, J. M. J. Madey, G. J. Ramian, H. A. Schwettman, T. I. Smith, *Physical Review Letters* **1977**, *38*, 892–894.

[233] R. Prazeres, J. M. Berset, R. Chaput, F. Glotin, D. A. Jaroszynski, J. M. Ortega, *Nuclear Instruments and Methods in Physics Research Section B: Beam Interactions with Materials and Atoms* **1994**, *89*, 54–59.

[234] D. Oepts, A. F. G. van der Meer, P. W. van Amersfoort, *Infrared Physics & Technology* **1995**, *36*, 297–308.

[235] M. Altarelli, *Nuclear Instruments and Methods in Physics Research Section B: Beam Interactions with Materials and Atoms* **2011**, *269*, 2845–2849.

[236] S. Schreiber, B. Faatz, *High Power Laser Science and Engineering* **2015**, *3*, 20.

[237] W. K. Lewis, *Journal of Industrial & Engineering Chemistry* **1922**, *14*, 492–496.

[238] J. W. A. Peters, *Journal of Industrial & Engineering Chemistry* **1922**, *14*, 476–479.

[239] J. W. A. Peters, *Industrial & Engineering Chemistry* **1923**, *15*, 402–403.

[240] A. J. P. Martin, R. L. M. Synge, *The Biochemical journal* **1941**, *35*, 1358–1368.

[241] E. Glueckauf, *Transactions of the Faraday Society* **1955**, *51*, 34–44.

[242] A. S. Said, *AIChE Journal* **1956**, *2*, 477–481.

[243] J. J. van Deemter, F. J. Zuiderweg, A. Klinkenberg, *Chemical Engineering Science* **1995**, *50*, 3869–3882.

[244] J. C. Giddings, H. Eyring, *The Journal of Physical Chemistry* **1955**, *59*, 416–421.

[245] J. C. Giddings, *Journal of Chemical Education* **1958**, *35*, 588.

[246] F. Dondi, M. Remelli, *The Journal of Physical Chemistry* **1986**, *90*, 1885–1891.

[247] A. Cavazzini, M. Remelli, F. Dondi, A. Felinger, *Analytical Chemistry* **1999**, *71*, 3453–3462.

[248] F. Dondi, A. Cavazzini, L. Pasti, *Journal of Chromatography A* **2006**, *1126*, 257–267.

[249] J. C. Giddings, *Separation Science and Technology* **1969**, *4*, 181–189.

[250] J. Giddings, *Dynamics of chromatography*, Marcel Dekker, New York, 1st ed., **1965**.

[251] J. C. Giddings, K. L. Mallik, *Analytical Chemistry* **1966**, *38*, 997–1000.

[252] C. Horváth, H.-J. Lin, *Journal of Chromatography A* **1978**, *149*, 43–70.

[253] J. H. Knox, *Journal of Chromatography A* **1999**, *831*, 3–15.

[254] S. Fanali, P. R. Haddad, C. F. Poole, P. Schoenmakers, D. Lloyd, *Liquid Chromatography: Fundamentals and Instrumentation*, Elsevier, 1st ed., **2013**.

[255] K. Vanderlinden, K. Broeckhoven, Y. Vanderheyden, G. Desmet, *Journal of Chromatography A* **2016**, *1442*, 73–82.

[256] H. Song, D. Sadriaj, G. Desmet, D. Cabooter, *Journal of Chromatography A* **2018**, *1532*, 124–135.

[257] J. Giddings, *Journal of Chromatography A* **1987**, *395*, 19–32.

[258] X. Huang, W. F. Coleman, R. N. Zare, *Journal of Chromatography A* **1989**, *480*, 95–110.

[259] S. Hjertén, *ELECTROPHORESIS* **1990**, *11*, 665–690.

[260] B. Gaš, M. Štědrý, E. Kenndler, *ELECTROPHORESIS* **1997**, *18*, 2123–2133.

[261] F. E. P. Mikkers, F. M. Everaerts, T. Verheggen, *Journal of Chromatography A* **1979**, *169*, 1–10.

[262] F. E. P. Mikkers, *Analytical Chemistry* **1999**, *71*, 522–533.

[263] M. Bier, O. A. Palusinski, R. A. Mosher, D. A. Saville, *Science* **1983**, *219*, 1281–1287.

[264] H. Poppe, *Analytical Chemistry* **1992**, *64*, 1908–1919.

[265] M. Dvořák, P. Dubský, M. Dovhunová, B. Gaš, *ELECTROPHORESIS* **2019**, *40*, 668–682.

[266] J. C. Giddings, *Journal of Chromatographic Science* **1964**, *2*, 167–169.

[267] J. C. Giddings, *Analytical Chemistry* **1963**, *35*, 353–356.

[268] G. E. Spangler, C. I. Collins, *Analytical Chemistry* **1975**, *47*, 403–407.

[269] A. B. Kanu, M. M. Gribb, H. H. Hill, *Analytical Chemistry* **2008**, *80*, 6610–6619.

[270] A. T. Kirk, M. Allers, P. Cochems, J. Langejuergen, S. Zimmermann, *Analyst* **2013**, *138*, 5200–5207.

[271] J. Giddings, *Journal of Chromatography A* **1989**, *480*, 21–33.

[272] A. T. Kirk, S. Zimmermann, *International Journal for Ion Mobility Spectrometry* **2015**, *18*, 129–135.

[273] A. T. Kirk, K. Bakes, S. Zimmermann, *International Journal for Ion Mobility Spectrometry* **2017**, *20*, 105–109.

[274] G. E. Spangler, *Analytical Chemistry* **1992**, *64*, 1312.

[275] A. V. Mariano, W. Su, S. K. Guharay, *Analytical Chemistry* **2009**, *81*, 3385–3391.

[276] M. Levin, A. Krisilov, B. Zon, G. Eiceman, *International Journal for Ion Mobility Spectrometry* **2014**, *17*, 73–77.

[277] A. V. Tolmachev, B. H. Clowers, M. E. Belov, R. D. Smith, *Analytical Chemistry* **2009**, *81*, 4778–4787.

[278] J. Xu, W. B. Whitten, J. M. Ramsey, *Analytical Chemistry* **2000**, *72*, 5787–5791.

[279] W. F. Siems, C. Wu, E. E. Tarver, H. H. J. Hill, P. R. Larsen, D. G. McMinn, *Analytical Chemistry* **1994**, *66*, 4195–4201.

[280] B. C. Hauck, W. F. Siems, C. S. Harden, V. M. McHugh, H. H. Hill, *International Journal for Ion Mobility Spectrometry* **2017**, *20*, 57–66.

[281] K. Tang, A. A. Shvartsburg, H.-N. Lee, D. C. Prior, M. A. Buschbach, F. Li, A. V. Tolmachev, G. A. Anderson, R. D. Smith, *Analytical Chemistry* **2005**, *77*, 3330–3339.

[282] E. S. Baker, B. H. Clowers, F. Li, K. Tang, A. V. Tolmachev, D. C. Prior, M. E. Belov, R. D. Smith, *Journal of the American Society for Mass Spectrometry* **2007**, *18*, 1176–1187.

[283] P. R. Kemper, N. F. Dupuis, M. T. Bowers, *International Journal of Mass Spectrometry* **2009**, *287*, 46–57.

[284] S. Warnke, C. Baldauf, M. T. Bowers, K. Pagel, G. von Helden, *Journal of the American Chemical Society* **2014**, *136*, 10308–10314.

[285] Y. M. Ibrahim, E. S. Baker, W. F. Danielson, R. V. Norheim, D. C. Prior, G. A. Anderson, M. E. Belov, R. D. Smith, *International Journal of Mass Spectrometry* **2015**, *377*, 655–662.

[286] J. C. May, J. N. Dodds, R. T. Kurulugama, G. C. Stafford, J. C. Fjeldsted, J. A. McLean, *Analyst* **2015**, *140*, 6824–6833.

[287] M. J. Manard, P. R. Kemper, *International Journal of Mass Spectrometry* **2016**, *402*, 1–11.

[288] M. F. Bush, I. D. G. Campuzano, C. V. Robinson, *Analytical Chemistry* **2012**, *84*, 7124–7130.

[289] S. J. Allen, K. Giles, T. Gilbert, M. F. Bush, *Analyst* **2016**, *141*, 884–891.

[290] A. T. Kirk, C.-R. Raddatz, S. Zimmermann, *Analytical Chemistry* **2017**, *89*, 1509–1515.

[291] R. Wojcik, G. Nagy, I. K. Attah, I. K. Webb, S. V. B. Garimella, K. K. Weitz, A. Hollerbach, M. E. Monroe, M. R. Ligare, F. F. Nielson, R. V. Norheim, R. S. Renslow, T. O. Metz, Y. M. Ibrahim, R. D. Smith, *Analytical Chemistry* **2019**, *91*, 11952–11962.

[292] C. Schaefer, A. T. Kirk, M. Allers, S. Zimmermann, *Journal of the American Society for Mass Spectrometry* **2020**, *31*, 2093–2101.

[293] P. J. Schoenmakers, J. K. Strasters, A. Bartha, *Journal of Chromatography A* **1988**, *458*, 355–370.

[294] E. V. Dose, G. Guiochon, *Analytical Chemistry* **1990**, *62*, 174–181.

[295] M. Dvořák, J. Svobodová, P. Dubský, M. Riesová, G. Vigh, B. Gaš, *ELECTROPHORESIS* **2015**, *36*, 646–654.

[296] J. H. Purnell, *Journal of the Chemical Society* **1960**, 1268–1274.

[297] J. H. Knox, *Journal of the Chemical Society* **1961**, 433–441.

[298] H. A. C. Thijssen, *Journal of Chromatography A* **1963**, *11*, 141–150.

[299] G. R. Asbury, H. H. Hill, *Journal of Microcolumn Separations* **2000**, *12*, 172–178.

[300] B. L. Karger, *Journal of Chromatographic Science* **1967**, *5*, 161–169.

[301] A. S. Said, *Journal of Chromatographic Science* **1964**, *2*, 60–71.

[302] A. S. Said, *Separation Science and Technology* **1978**, *13*, 647–679.

[303] K. Suematsu, T. Okamoto, *Journal of Chromatographic Science* **1989**, *27*, 13–17.

[304] J. C. Giddings, *Analytical Chemistry* **1968**, *40*, 2143–2149.

[305] J. P. Foley, *Analyst* **1991**, *116*, 1275–1279.

[306] J. W. Jorgenson, K. D. Lukacs, *Analytical Chemistry* **1981**, *53*, 1298–1302.

[307] S. J. Valentine, D. E. Clemmer, *Analytical Chemistry* **2009**, *81*, 5876–5880.

[308] L. A. Viehland, S. L. Lin, E. A. Mason, *Chemical Physics* **1981**, *54*, 341–364.

[309] L. A. Viehland, *International Journal for Ion Mobility Spectrometry* **2016**, *19*, 11–14.

[310] L. A. Viehland, *International Journal for Ion Mobility Spectrometry* **2016**, *19*, 1–10.

[311] G. R. Asbury, H. H. Hill, *Analytical Chemistry* **2000**, *72*, 580–584.

[312] R. T. Kurulugama, E. Darland, F. Kuhlmann, G. Stafford, J. Fjeldsted, *Analyst* **2015**, *140*, 6834–6844.

[313] C. B. Morris, J. C. May, K. L. Leaptrot, J. A. McLean, *Journal of The American Society for Mass Spectrometry* **2019**, *30*, 1059–1068.

[314] R. Fernández-Maestre, C. Wu, H. H. Hill Jr, *Rapid Communications in Mass Spectrometry* **2012**, *26*, 2211–2223.

[315] E. Waraksa, U. Perycz, J. Namieśnik, M. Sillanpää, T. Dymerski, M. Wójtowicz, J. Puton, *TrAC Trends in Analytical Chemistry* **2016**, *82*, 237–249.

[316] J. N. Dodds, J. C. May, J. A. McLean, *Analytical Chemistry* **2017**, *89*, 12176–12184.

[317] W. F. Siems, L. A. Viehland, H. H. Hill, *Analyst* **2016**, *141*, 6396–6407.

[318] J. C. Giddings, *Analytical Chemistry* **1967**, *39*, 1027–1028.

[319] J. M. Davis, J. C. Giddings, *Analytical Chemistry* **1983**, *55*, 418–424.

[320] E. Grushka, *Analytical Chemistry* **1970**, *42*, 1142–1147.

[321] U. D. Neue, *Journal of Chromatography A* **2008**, *1184*, 107–130.

[322] C. Horváth, S. R. Lipsky, *Analytical Chemistry* **1967**, *39*, 1893.

[323] D. Zwillinger, V. Moll, I. S. Gradshteyn, I. M. Ryzhik, *Table of Integrals, Series, and Products*, Academic Press, Boston, 8th ed., **2014**.

[324] L. W. Potts, P. W. Carr, *Analytical Chemistry* **2011**, *83*, 7614–7615.

[325] L. S. Fenn, J. A. McLean, *Chemical Communications* **2008**, 5505–5507.

[326] L. Li, K. R. McKenna, Z. Li, M. Yadav, R. Krishnamurthy, C. L. Liotta, F. M. Fernández, *Analyst* **2018**, *143*, 949–955.

[327] B. Xia, Z. S. Kawar, T. Ju, R. A. Alvarez, G. P. Sachdev, R. D. Cummings, *Nature Methods* **2005**, *2*, 845–850.

[328] L. R. Ruhaak, G. Zauner, C. Huhn, C. Bruggink, A. M. Deelder, M. Wuhrer, *Analytical and Bioanalytical Chemistry* **2010**, *397*, 3457–3481.

[329] M. Pabst, D. Kolarich, G. Pöltl, T. Dalik, G. Lubec, A. Hofinger, F. Altmann, *Analytical Biochemistry* **2009**, *384*, 263–273.

[330] D. J. Harvey, *Journal of Chromatography B* **2011**, *879*, 1196–1225.

[331] M. Melmer, T. Stangler, A. Premstaller, W. Lindner, *Journal of Chromatography A* **2011**, *1218*, 118–123.

[332] M. A. Lauber, Y.-Q. Yu, D. W. Brousmiche, Z. Hua, S. M. Koza, P. Magnelli, E. Guthrie, C. H. Taron, K. J. Fountain, *Analytical Chemistry* **2015**, *87*, 5401–5409.

[333] D. J. Harvey, T. S. Mattu, M. R. Wormald, L. Royle, R. A. Dwek, P. M. Rudd, *Analytical Chemistry* **2002**, *74*, 734–740.

[334] M. Wuhrer, A. M. Deelder, Y. E. M. van der Burgt, *Mass Spectrometry Reviews* **2011**, *30*, 664–680.

[335] M. Kusche-Gullberg, L. Kjellén, *Current Opinion in Structural Biology* **2003**, *13*, 605–611.

[336] U. Lindahl, G. Bäckström, L. Thunberg, I. G. Leder, *Proceedings of the National Academy of Sciences* **1980**, *77*, 6551–6555.

[337] S. Yusuf *et al.*, *New England Journal of Medicine* **2006**, *354*, 1464–1476.

[338] J. I. Weitz, L.-A. Linkins, *Expert Opinion on Investigational Drugs* **2007**, *16*, 271–282.

[339] D. Shukla, J. Liu, P. Blaiklock, N. W. Shworak, X. Bai, J. D. Esko, G. H. Cohen, R. J. Eisenberg, R. D. Rosenberg, P. G. Spear, *Cell* **1999**, *99*, 13–22.

[340] J. Zaia, *Molecular & Cellular Proteomics* **2013**, *12*, 885.

[341] J. J. Wolff, I. J. Amster, L. Chi, R. J. Linhardt, *Journal of the American Society for Mass Spectrometry* **2007**, *18*, 234–244.

[342] J. J. Wolff, T. N. Laremore, H. Aslam, R. J. Linhardt, I. J. Amster, *Journal of the American Society for Mass Spectrometry* **2008**, *19*, 1449–1458.

[343] J. J. Wolff, F. E. Leach, T. N. Laremore, D. A. Kaplan, M. L. Easterling, R. J. Linhardt, I. J. Amster, *Analytical Chemistry* **2010**, *82*, 3460–3466.

[344] Y. Huang, X. Yu, Y. Mao, C. E. Costello, J. Zaia, C. Lin, *Analytical Chemistry* **2013**, *85*, 11979–11986.

[345] J. Wu, J. Wei, J. D. Hogan, P. Chopra, A. Joshi, W. Lu, J. Klein, G.-J. Boons, C. Lin, J. Zaia, *Journal of The American Society for Mass Spectrometry* **2018**, *29*, 1262–1272.

[346] D. R. Klein, F. E. Leach, I. J. Amster, J. S. Brodbelt, *Analytical Chemistry* **2019**, *91*, 6019–6026.

[347] A. M. Hawkridge, S. Hackbusch, *Analytical and Bioanalytical Chemistry* **2020**, *412*, 7925–7935.

[348] F. E. Leach, M. Ly, T. N. Laremore, J. J. Wolff, J. Perlow, R. J. Linhardt, I. J. Amster, *Journal of the American Society for Mass Spectrometry* **2012**, *23*, 1488–1497.

[349] I. Agyekum, A. B. Patel, C. Zong, G.-J. Boons, I. J. Amster, *International Journal of Mass Spectrometry* **2015**, *390*, 163–169.

[350] J. Wu, J. Wei, P. Chopra, G.-J. Boons, C. Lin, J. Zaia, *Analytical Chemistry* **2019**, *91*, 11738–11746.

[351] L. E. Pepi, F. E. Leach, D. R. Klein, J. S. Brodbelt, I. J. Amster, *Journal of the American Society for Mass Spectrometry* **2021**, *32*, 1759–1770.

[352] M. R. Schenauer, J. K. Meissen, Y. Seo, J. B. Ames, J. A. Leary, *Analytical Chemistry* **2009**, *81*, 10179–10185.

[353] M. J. Kailemia, M. Park, D. A. Kaplan, A. Venot, G.-J. Boons, L. Li, R. J. Linhardt, I. J. Amster, *Journal of The American Society for Mass Spectrometry* **2014**, *25*, 258–268.

[354] R. L. Miller, W. Wei, R. Schwörer, O. V. Zubkova, P. C. Tyler, J. E. Turnbull, J. A. Leary, *European Journal of Mass Spectrometry* **2015**, *21*, 245–254.

[355] J. Wei, J. Wu, Y. Tang, M. E. Ridgeway, M. A. Park, C. E. Costello, J. Zaia, C. Lin, *Analytical Chemistry* **2019**, *91*, 2994–3001.

[356] R. L. Miller, S. E. Guimond, R. Schwörer, O. V. Zubkova, P. C. Tyler, Y. Xu, J. Liu, P. Chopra, G.-J. Boons, M. Grabarics, C. Manz, J. Hofmann, N. G. Karlsson, J. E. Turnbull, W. B. Struwe, K. Pagel, *Nature Communications* **2020**, *11*, 1481.

[357] E. B. Cagmat, J. Szczepanski, W. L. Pearson, D. H. Powell, J. R. Eyler, N. C. Polfer, *Physical Chemistry Chemical Physics* **2010**, *12*, 3474–3479.

[358] B. Schindler, G. Renois-Predelus, N. Bagdadi, S. Melizi, L. Barnes, S. Chambert, A.-R. Allouche, I. Compagnon, *Glycoconjugate Journal* **2017**, *34*, 421–425.

[359] B. Schindler, L. Barnes, C. J. Gray, S. Chambert, S. L. Flitsch, J. Oomens, R. Daniel, A. R. Allouche, I. Compagnon, *The Journal of Physical Chemistry A* **2017**, *121*, 2114–2120.

[360] N. Khanal, C. Masellis, M. Z. Kamrath, D. E. Clemmer, T. R. Rizzo, *Analytical Chemistry* **2017**, *89*, 7601–7606.

[361] H. A. Orgueira, A. Bartolozzi, P. Schell, R. E. J. N. Litjens, E. R. Palmacci, P. H. Seeberger, *Chemistry – A European Journal* **2003**, *9*, 140–169.

[362] S. Arungundram, K. Al-Mafraji, J. Asong, F. E. Leach, I. J. Amster, A. Venot, J. E. Turnbull, G.-J. Boons, *Journal of the American Chemical Society* **2009**, *131*, 17394–17405.

[363] S. Eller, M. Collot, J. Yin, H. S. Hahm, P. H. Seeberger, *Angewandte Chemie International Edition* **2013**, *52*, 5858–5861.

[364] L. Sun, P. Chopra, G.-J. Boons, *The Journal of Organic Chemistry* **2020**, *85*, 16082–16098.

[365] B. Kuberan, M. Z. Lech, D. L. Beeler, Z. L. Wu, R. D. Rosenberg, *Nature Biotechnology* **2003**, *21*, 1343–1346.

[366] J. Gottschalk, L. Elling, *Current Opinion in Chemical Biology* **2021**, *61*, 71–80.

[367] Y. Xu, S. Masuko, M. Takieddin, H. Xu, R. Liu, J. Jing, S. A. Mousa, R. J. Linhardt, J. Liu, *Science* **2011**, *334*, 498–501.

[368] S. Köhling, G. Künze, K. Lemmnitzer, M. Bermudez, G. Wolber, J. Schiller, D. Huster, J. Rademann, *Chemistry – A European Journal* **2016**, *22*, 5563–5574.

[369] W. Lu, C. Zong, P. Chopra, L. E. Pepi, Y. Xu, I. J. Amster, J. Liu, G.-J. Boons, *Angewandte Chemie International Edition* **2018**, *57*, 5340–5344.

[370] X. Zhang, L. Lin, H. Huang, R. J. Linhardt, *Accounts of Chemical Research* **2020**, *53*, 335–346.

[371] S. Köhling, J. Blaszkiewicz, G. Ruiz-Gómez, M. I. Fernández-Bachiller, K. Lemmnitzer, N. Panitz, A. G. Beck-Sickinger, J. Schiller, M. T. Pisabarro, J. Rademann, *Chemical Science* **2019**, *10*, 866–878.

[372] W. B. Struwe, C. Baldauf, J. Hofmann, P. M. Rudd, K. Pagel, *Chemical Communications* **2016**, *52*, 12353–12356.

[373] S. Brézillon, V. Untereiner, L. Lovergne, I. Tadeo, R. Noguera, F.-X. Maquart, Y. Wegrowski, G. D. Sockalingum, *Analytical and Bioanalytical Chemistry* **2014**, *406*, 5795–5803.

[374] A. Supady, V. Blum, C. Baldauf, *Journal of Chemical Information and Modeling* **2015**, *55*, 2338–2348.

[375] V. Blum, R. Gehrke, F. Hanke, P. Havu, V. Havu, X. Ren, K. Reuter, M. Scheffler, *Computer Physics Communications* **2009**, *180*, 2175–2196.

[376] C. Adamo, V. Barone, *The Journal of Chemical Physics* **1999**, *110*, 6158–6170.

[377] S. Grimme, J. Antony, S. Ehrlich, H. Krieg, *The Journal of Chemical Physics* **2010**, *132*, 154104.

[378] F. Weigend, R. Ahlrichs, *Physical Chemistry Chemical Physics* **2005**, *7*, 3297–3305.

[379] J. Zheng, X. Xu, D. G. Truhlar, *Theoretical Chemistry Accounts* **2011**, *128*, 295–305.

[380] S. Warnke, A. Ben Faleh, T. R. Rizzo, *ACS Measurement Science Au* **2021**, DOI: 10.1021/acsmeasuresciau.1c00018.

[381] D. R. Hernandez, J. D. DeBord, M. E. Ridgeway, D. A. Kaplan, M. A. Park, F. Fernandez-Lima, *Analyst* **2014**, *139*, 1913–1921.

[382] K. Michelmann, J. A. Silveira, M. E. Ridgeway, M. A. Park, *Journal of The American Society for Mass Spectrometry* **2015**, *26*, 14–24.

[383] J. A. Silveira, K. Michelmann, M. E. Ridgeway, M. A. Park, *Journal of the American Society for Mass Spectrometry* **2016**, *27*, 585–595.

[384] M. E. Ridgeway, M. Lubeck, J. Jordens, M. Mann, M. A. Park, *International Journal of Mass Spectrometry* **2018**, *425*, 22–35.

[385] A. S. Rathore, C. Horváth, *Journal of Chromatography A* **1996**, *743*, 231–246.

Acknowledgements

There are many people who – in one way or another – have contributed to the work presented in this thesis and helped to turn my graduate studies into an exciting experience filled with pleasant memories. I would like to mention first my supervisor, Kevin Pagel, to whom I am truly thankful for several reasons. First and foremost, for offering me a doctoral position in his research group at a casual Friday dinner, which marked the end of my rather short but all the more fascinating first visit to Berlin. Of course, a PhD position alone would not have meant too much, had it not come together with his continuous support and contagious enthusiasm, plenty of interesting research projects, and an exceptionally friendly and motivating working atmosphere. I am especially thankful for being given the scientific freedom and independence that I consider essential for the development of ideas.

I am also very grateful to Gert von Helden, who has become my informal second supervisor at the FHI. In addition to providing me the opportunity to work with the most exciting experimental setups, his insightful comments concerning both experimental and theoretical aspects of my research have been crucial for many projects. I would also like to thank Gerard Meijer for his support, and for making me feel not merely like a welcome guest but a full member of the Department of Molecular Physics.

At this point I would like to say thank you to Szabolcs Béni and Gunda Köllensperger, my former supervisors, who oversaw my first clumsy steps in academic research as an undergraduate and fostered my interest in analytical chemistry. I am really happy that we are not only still in contact but have also managed to maintain a fruitful scientific collaboration.

A day in the life of a PhD candidate would be of course much less enjoyable if they were not surrounded by fellow students and postdocs. In this sense I consider myself extremely lucky, since I had the chance to get to know so many friendly, interesting, and talented young researchers in the past few years. Besides patiently introducing me to the modified Synapt instrument, Christian Manz and Johanna Hofmann also helped me overcome all the unexpected obstacles hiding in the labyrinth of the German bureaucratic system. Mateusz

Marianski and Jongcheol Seo – both on tenure track now – have taught me more about molecular symmetry, point groups, and homebrewing than all my undergraduate chemistry courses combined. I would also like to thank Daniel Thomas, Eike Mucha, Jan Horlebein, Katja Ober, Kim Greis, Łukasz Polewski, Clemens Richter, and all other participants of the FHI Sitcom for making our time at the Haber Villa one of the highlights of the past years.

I am especially thankful to Maike Lettow for making exhausting beam shifts seem much less tiring, for never shutting down a HeDrop experiment before the first U-Bahn started running in the morning so that I did not have to take the night bus to the other side of Berlin, and for preparing a special birthday cake when I suddenly turned a year older during one of the long days in the lab. In relation to beam shifts and lasers I would also like to thank Wieland Schöllkopf and Sandy Gewinner, who made sure that we always had enough IR photons to kick those ions out of the helium droplets.

Days of data evaluation and writing have been made a lot more enjoyable by Gergő Péter Szekeres, with whom we established a small exclave of Hungary at the FHI in the form of a shared office. I would also like to thank my latest and noblest office mate, Carla Freifrau von Kirschbaum, for preparing our fearsome coat of arms with the rabbit from Monty Python's Holy Grail. Her genuine kindness and inexplicable enthusiasm for the word "csütörtök" helped me keep my good mood and sanity during the last few weeks of writing this thesis.

There are many other colleagues whom I would like to acknowledge herein. Waldemar Hoffmann, Melanie Göth, Leonhard Urner, Rayoon Chang, Martín Taccone, Michael Götze, Emeline Hanozin, Denis Morsa, Leïla Bechtella, Andreas Zappe, Anna Wolf, Chun-Wei Chang, Jerome Riedel, Sascha Schaller, Sebastian Malerz, Simon Hofsäss, Maximilian Doppelbauer, Ju Hyeon Lee, Silvio Marx, Christian Schewe, Sebastian Kray, Inga von Dölln, Karin Grassow, Manuela Misch, Henrik Haak, Klaus Peter Vogelgesang, Uwe Hoppe, and Boris Sartakov have all contributed to the nice atmosphere at the university or at the FHI. Special thanks go to Jesús Pérez-Ríos for handing me a life-saving copy of *Gradshteyn and Ryzhik*.

In addition to colleagues from Berlin mentioned above, I would like to acknowledge a few long-standing collaborators from other parts of Germany and Europe. The contribution of Ansgar Kirk and Tim Causon was indispensable for the development of the plate-height model, and I hope that our collaboration will last for many more years in the future. I also want to say thank you to Konrad Koszinowski and Thomas Auth for the exciting adventure into the realm of organometallics and catalytic intermediates. Being a pharmacist by training, I did not think of venturing this far from mixing creams and ointments in a small-town drugstore, but organometallic chemistry appeared

to me as an intriguing and refreshing novelty.

Finally, I would like to express my gratitude to my friends and family. To Ádám, Áron, Dani, and Márk for visiting me so often here in Berlin; to Jingwei for always finding a way to be cheerful and cheer up everybody else around herself; to my sisters, Gréti and Kitti, for listening so patiently whenever I gave a completely incomprehensible answer to the simple and well-justified question: "So what is your research actually about?"; and of course to my parents for their unconditional support that enabled me to pursue a life in science.

While I may not be in the position to assess the real scientific value of this thesis, I am confident to say that the journey towards it was a truly wonderful experience!

List of publications

1. M. Grabarics,* O. Csernák,* R. Balogh, S. Béni; Analytical characterization of human milk oligosaccharides – potential applications in pharmaceutical analysis, *Journal of Pharmaceutical and Biomedical Analysis* **2017**, *146*, 168–178.

2. S. Theiner, M. Grabarics, L. Galvez, H. P. Varbanov, N. S. Sommerfeld, M. Galanski, B. K. Keppler, G. Koellensperger; The impact of whole human blood on the kinetic inertness of platinum(IV) prodrugs – an HPLC-ICP-MS study, *Dalton Transactions* **2018**, *47*, 5252–5258.

3. L. Galvez, S. Theiner, M. Grabarics, C. R. Kowol, B. K. Keppler, S. Hann, G. Koellensperger; Critical assessment of different methods for quantitative measurement of metallodrug–protein associations, *Analytical and Bioanalytical Chemistry* **2018**, *410*, 7211–7220.

4. C. Manz, M. Grabarics, F. Hoberg, M. Pugini, A. Stuckmann, W. B. Struwe, K. Pagel; Separation of isomeric glycans by ion mobility spectrometry – the impact of fluorescent labelling, *Analyst* **2019**, *144*, 5292–5298.

5. M. Lettow,* M. Grabarics,* E. Mucha, D. A. Thomas, L. Polewski, J. Freyse, J. Rademann, G. Meijer, G. von Helden, K. Pagel; IR action spectroscopy of glycosaminoglycan oligosaccharides, *Analytical and Bioanalytical Chemistry* **2020**, *412*, 533–537.

6. R. L. Miller, S. E. Guimond, R. Schwörer, O. V. Zubkova, P. C. Tyler, Y. Xu, J. Liu, P. Chopra, G.-J. Boons, M. Grabarics, C. Manz, J. Hofmann, N. G. Karlsson, J. E. Turnbull, W. B. Struwe, K. Pagel; Shotgun ion mobility mass spectrometry sequencing of heparan sulfate saccharides, *Nature Communications* **2020**, *11*, 1481.

7. M. Lettow,* M. Grabarics,* K. Greis, E. Mucha, D. A. Thomas, P. Chopra, G.-J. Boons, R. Karlsson, J. E. Turnbull, G. Meijer, R. L.

Miller, G. von Helden, K. Pagel; Cryogenic infrared spectroscopy reveals structural modularity in the vibrational fingerprints of heparan sulfate diastereomers, *Analytical Chemistry* **2020**, *92*, 10228–10232.

8. M. Grabarics, M. Lettow, A. T. Kirk, G. von Helden, T. J. Causon, K. Pagel; Plate-height model of ion mobility-mass spectrometry, *Analyst* **2020**, *145*, 6313–6333.

9. B. Várnai, M. Grabarics, Z. Szakács, K. Pagel, M. Malanga, T. Sohajda, S. Béni; Structural characterization of fondaparinux interaction with per-6-amino-beta-cyclodextrin: An NMR and MS study, *Journal of Pharmaceutical and Biomedical Analysis* **2021**, *197*, 113947.

10. M. Lettow, K. Greis, M. Grabarics, J. Horlebein, R. L. Miller, G. Meijer, G. von Helden, K. Pagel; Chondroitin sulfate disaccharides in the gas phase: Differentiation and conformational constraints, *The Journal of Physical Chemistry A* **2021**, *125*, 4373–4379.

11. T. Auth,* M. Grabarics,* M. Schlangen, K. Pagel, K. Koszinowski; Modular ion mobility calibrants for organometallic anions based on tetraorganylborate salts, *Analytical Chemistry* **2021**, *93*, 9797–9807.

12. M. Grabarics, M. Lettow, A. T. Kirk, G. von Helden, T. J. Causon, K. Pagel; Plate-height model of ion mobility-mass spectrometry: Part 2. Peak-to-peak resolution and peak capacity, *Journal of Separation Science* **2021**, *44*, 2798–2813.

13. M. Grabarics, M. Lettow, C. Kirschbaum, K. Greis, C. Manz, K. Pagel; Mass spectrometry-based techniques to elucidate the sugar code, *Chemical Reviews* **2021**. DOI: 10.1021/acs.chemrev.1c00380

The asterisks indicate equal contribution of the respective authors.